www.isac-net.org May 2021

ISAC
INTERNATIONAL SOCIETY FOR ADVANCEMENT OF CYTOMETRY

CYTOMETRY

Journal of Quantitative Cell Science PART A

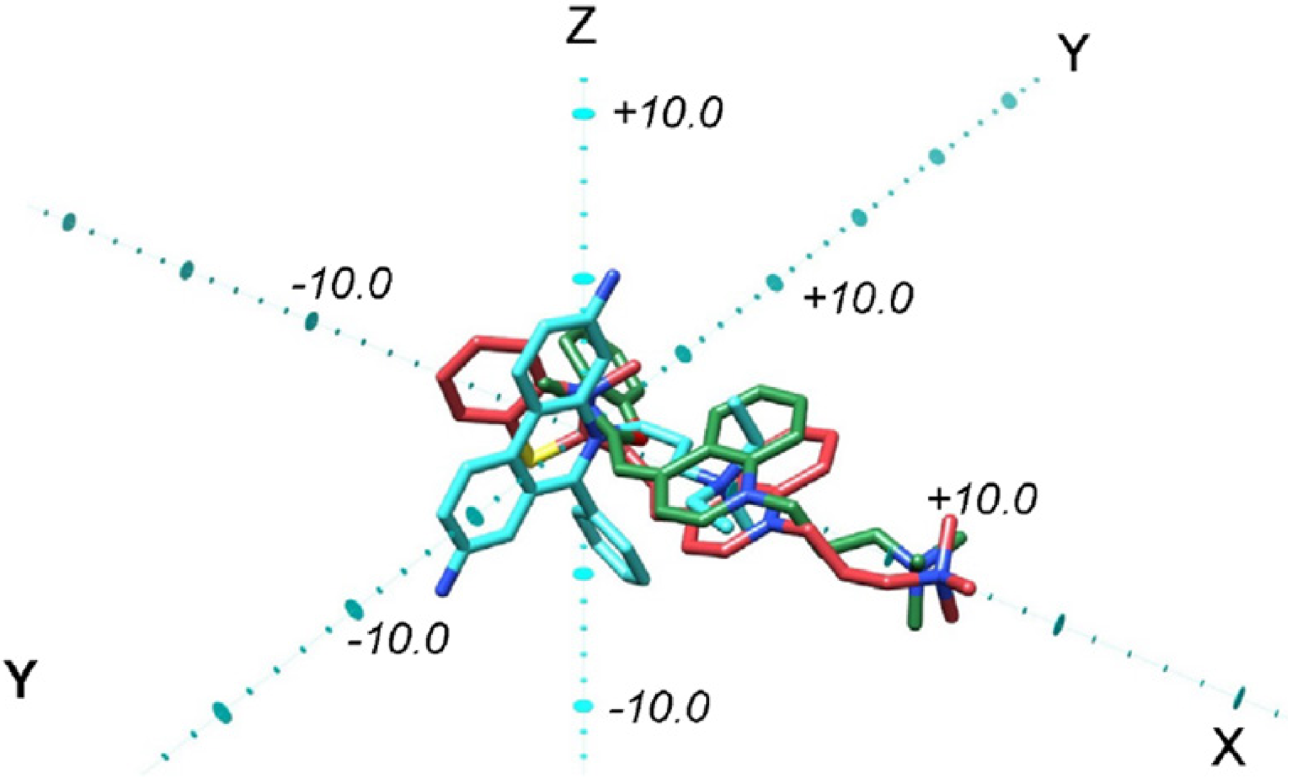

SPECIAL COLLECTION

Clinical & Cellular Uses of Flow Cytometry

WILEY


BIO-RAD
ZE5 Cell Analyzer
BIOSERO

TABLE OF CONTENTS

Clinical and Cellular Uses of Flow Cytometry:
An Introduction

by Gwen Taylor, Ph.D.
Managing Editor of *Cytometry Part A*, the official journal of the International Society for the Advancement of Cytometry

The array of applications that can be studied by flow cytometry is extraordinarily broad, spanning essentially any basic or clinical research involving single cells. This collection of articles presents a sampling of flow cytometry-based studies for the purposes of drug screening, clinical sample analysis, cell communication, and food science.

Barczyk et al. (2020) describes the development of multi-parameter drug screening methods based on conventional flow cytometry, imaging flow cytometry, and spectral flow cytometry. These techniques were used to measure the activity of the P2X purinergic receptor 7 (P2RX7) upon activation by a modified ATP molecule. P2RX7 is a poorly selective ATP-gated ion channel and has emerged as a potential therapeutic target in inflammation, neuropathic pain, Alzheimer's disease, and cancer. This group demonstrated the simultaneous quantification of calcium influx (Fluo-3 AM), large pore opening (TO-PRO-3, a DNA-intercalating dye), and viability (propidium iodide) for low- to medium-throughput screening of P2RX7 modulators. Spectral cytometry notably enabled assay of several biological activities while correcting for the intrinsic fluorescence of the screened compounds—a well-known limitation of fluorescence-based screening.

Flow cytometry-based assays can also be used for rapid, highly reproducible analysis of clinical and nonclinical samples. For example, Grasse et al. (2018) describe development of a simple, rapid flow cytometry assay to measure the capacity of antibodies to mediate Fc-receptor-dependent phagocytosis in the setting of Chlamydia trachomatis infection. C. trachomatis is a bacterial infection that can cause permanent damage to fallopian tubes, resulting in infertility and increased risk of ectopic pregnancy. There is a great need for a vaccine against C. trachomatis and as a result there is a need for assays to evaluate functional immune responses for use in clinical trials and epidemiological studies. The flow cytometry method presented by Grasse et al. provides a substantial advantage over the previous time-consuming, labor-intensive, and low-throughput methodology that involved visualization of phagocytized bacteria via immunofluorescence staining, followed by manual counting of the bacterial inclusions by microscopy.

Cells release membrane-enclosed particles called extracellular vesicles (EVs) into their environment to communicate and to transport waste. EVs are present in all body fluids and are potential biomarkers because their concentration and composition change with disease, including in cancer, cardiovascular disease, and immune responses. Flow cytometry is often used to characterize EVs in body fluids because of its high throughput and ability to distinguish between different EV populations at the single-EV level based on immunophenotype. However, due to their small size and low refractive index, the scatter intensity of most EVs is below the detection limit of common flow cytometers. de Rond et al. (2020) describe modifications to the optical and fluidics configurations of a flow cytometer to produce a user-friendly, high-throughput, and high-sensitivity assay with significantly improved detection limits for studying EVs.

Flow cytometry is also used for high-throughput determination of microbial abundance in a range of medical, environmental, and food-related applications. For example, in environments that require specific species to thrive, such as in wine fermentation, determining microbial abundance can provide information to winemakers, enabling successful fermentation progression. Bartle et al. (2021) describe a straightforward flow cytometric approach to enumerating the most common wine bacterium, Oenococcus oeni. However, determination of O. oeni cell concentration by flow cytometry presents several challenges because these cells often occur in doublets or chains of varying lengths, and are also very small and may exhibit a range of morphologies. The authors describe various parameters, such as sample preparation techniques, knowledge of varying cell morphologies in different phases of growth, and equipment settings that need to be considered when developing flow cytometry assays for enumeration of these bacterial cells.

This collection of articles represents only a selection of the types of single-cell studies that can be accomplished using flow cytometry. It is a highly adaptable technique and, in addition to the areas mentioned above, has applications in diagnostics, hematological research, biomarker detection, chromosome analysis, and many other areas.

REFERENCES

Barczyk A et al. (2020). Flow cytometry: An accurate tool for screening P2RX7 modulators. Cytometry Vol/Issue:1-14. https://doi.org/10.1002/cyto.a.24287

Grasse M et al. (2018). A flow cytometry-based assay to determine the phagocytic activity of both clinical and nonclinical antibody samples against Chlamydia trachomatis. Cytometry 93:525-532. https://doi.org/10.1002/cyto.a.23353

de Rond L et al. (2020). A systematic approach to improve scatter sensitivity of a flow cytometer for detection of extracellular vesicles. Cytometry 97, 582-591. https://doi.org/10.1002/cyto.a.23974

Bartle L et al. (2021). Evaluating the cytometric detection and enumeration of the wine bacterium, Oenococcus oeni. Cytometry Vol/Issue/pages. https://doi.org/10.1002/cyto.a.24258

CYTOMETRY
Journal of Quantitative Cell Science PART A

A Flow Cytometry-Based Assay to Determine the Phagocytic Activity of Both Clinical and Nonclinical Antibody Samples Against *Chlamydia trachomatis*

Marco Grasse,[1,2] Ida Rosenkrands,[1] Anja Olsen,[1] Frank Follmann,[1] Jes Dietrich[1*]

[1]Department of Infectious Disease Immunology, Statens Serum Institut, Copenhagen, Denmark

[2]Department of Immunology, Institute for Biomedical Aging Research, Universität Innsbruck, Innsbruck, Austria

Received 6 October 2017; Revised 15 December 2017; Accepted 12 February 2018

Grant sponsor: Danish 3 R Center, project no 33010-NIFA-17–672

Grant sponsor: Austrian Science Fund (FWF; doctoral programme HOROS, W 1253)

Grant sponsor: European Commission through the ADITEC, Grant number: FP7-HEALTH-2011.1.4–4-280873

Grant sponsor: TRACVAC consortium contract (EU Horizon 2020), Grant number: 2017–733373

Additional Supporting Information may be found in the online version of this article

*Correspondence to: Jes Dietrich; Department of Infectious Disease Immunology, Statens Serum Institut, Artillerivej 5, DK-2300 Copenhagen S, Denmark. E-mail: jdi@ssi.dk

DOI: 10.1002/cyto.a.23353

Abstract

Globally, an estimated 131 million new cases of chlamydial infection occur annually. *Chlamydia trachomatis* infection can cause permanent damage to the fallopian tubes in woman, resulting in infertility and a risk of ectopic pregnancy. There is a great need for a vaccine against *Chlamydia trachomatis* and as a result there is a need for assays to evaluate functional immune responses for use in future clinical trials and epidemiological studies. Antibodies play a crucial role in the defense against infection and can be protective by several functions, including phagocytosis and neutralization. Vaccine development could greatly benefit from a method to measure functional *C. trachomatis*-specific antibodies in a large number of samples. In the current in vitro antibody protection assays, which measure the capacity of antibodies to facilitate phagocytic uptake of *C. trachomatis*, the phagocytosed bacteria have to be counted manually. This is both labor demanding, time consuming, and it prevents high-throughput usage of this method. In this study, we, therefore, developed a simple and rapid flow cytometry based assay to measure the capacity of antibodies to mediate Fc-receptor dependent phagocytosis. This method is highly reproducible and suitable to analyze large numbers of clinical and nonclinical samples.

Key terms
chlamydia; antibody; flow cytometry; vaccine; phagocytosis

CHLAMYDIACEAE are a family of gram-negative intracellular bacteria with a wide host range and diverse pathological outcomes (1). Globally, an estimated 131 million new cases of *Chlamydia trachomatis* (*C. trachomatis)* infections occur annually. Genital infection with *C. trachomatis* (Sv D-K and L) is the most common bacterial sexually transmitted infection. Ascension of chlamydial infection to the female upper genital tract can cause acute pelvic inflammatory disease, infertility, and ectopic pregnancy. Shortcomings of current chlamydia control strategies, has highlighted the need for a vaccine against *C. trachomatis* (2).

Protective immunity against an infection with *C. trachomatis* involves both T and B cells (3–5). As a consequence, development of high-throughput assays for determination of T cell-specific epitopes, as well as B cell specific epitopes is important. Recently, the role of neutralizing antibodies (Abs) has received increasing attention, and immunization with an extended major outer membrane protein (MOMP) variable domain 4 (VD4) region, containing the conserved LNPTIAG region, elicited neutralizing Abs in mice (6). However, although recent reports have demonstrated that neutralizing Abs can be protective against infection with *C. trachomatis* (6), other studies have indicated that neutralization may not be sufficient for protection (7–10). Thus, it has been suggested that Abs may exert several roles in addition to

ISAC
International Society for Advancement of Cytometry

neutralization during an infection with *C. trachomatis* (11). Such roles could be to increase T cell activation, induce killing of epithelial cells via antibody-dependent cell-mediated cytotoxicity (12,13) or phagocytosis of antibody-coated chlamydiae (14).

Ab induced phagocytosis is mediated by the constant part of the Ab, which binds to Fc-receptors on the surface of the phagocytic cell. A phagocytosis assay measures the ability of an Ab to increase uptake of the bacteria into a phagocytic cell, and counting of the engulfed bacteria often involves visualization via immunofluorescence staining, followed by manually counting the bacterial inclusions via microscopy. This method of bacterial counting is a time consuming, labor demanding, low-throughput method, and only a limited number of samples can be handled. Efficient vaccine antigen discovery and development require more effective high-throughput assays.

Here we present a simple, rapid flow cytometry (FCM) based assay to measure the capacity of Abs to mediate Fc-receptor dependent phagocytosis. This method is highly reproducible and suitable to analyze large numbers of clinical and nonclinical samples.

MATERIALS AND METHODS

Cells

Hela 229 cells were obtained from American Type Culture Collection (ATCC, Manassas, Virginia). The adherent cells were maintained in RPMI 1640 (Gibco®, Thermofischer Scientific, Waltham, Massachusetts) supplemented with 1% (vol/vol) L-Glutamine, 1% (vol/vol) HEPES, 1% (vol/vol) nonessential amino acids (NEAA), 1% (vol/vol) pyrovate, 10 µg/ml gentamicin and 5% heat-inactivated fetal bovine serum (FBS) at 37°C/5% CO_2. Cells were splitted after reaching a confluence of 80%.

McCoy cells were used to determine the concentration of the bacteria used in the experiments. McCoy cells were obtained from ATCC and maintained in RPMI 1640 supplemented with 1% (vol/vol) L-Glutamine, 1% (vol/vol) HEPES, 1% (vol/vol) pyrovate, 1% (vol/vol) NEAA, 70 µM Mercaptoethanol, 10 µg/ml gentamicin and 10% heat-inactivated FBS at 37°C/5% CO_2.

PLB-985 cells, a human myeloid leukaemia cell line, were obtained from German Collection of Microorganisms and Cell Cultures (DSMZ, Braunschweig, Germany). The cells were maintained in suspension in RPMI 1640 supplemented with 1% (vol/vol) L-Glutamine, 1% (vol/vol) HEPES, 1% (vol/vol) pyrovate, 1% (vol/vol) NEAA, 10 µg/ml gentamicin, and 10% heat-inactivated FBS at 37°C/5% CO_2. The culture media was changed every 3–4 days to maintain a cell density between 2×10^5 and 1×10^6 cells/ml. To differentiate them into a neutrophil-like cell type, 200,000 cells/ml were stimulated with 100 mM N,N-Dimethylformamide (DMF; Sigma-Aldrich, St. Louis, Missouri) in culture media without HEPES and antibiotics for 5 days at 37°C/5% CO_2. The assay media of the PLB-985 cells was culture media without HEPES and antibiotics.

HL-60 cells, a human promyeloblast cell line, were obtained from ATCC. These cells were maintained and stimulated identical to the PLB-985 cells.

Bacteria

C. trachomatis SvD (UW-3/Cx; ATCC VR-885) were propagated in Hela 229 cells and purified as described elsewhere (15). Bacteria were resuspended in sucrose (1 M)—phoshphate (0.5 M)—glutamate (0.2 M) buffer (SPG) and stored at −80°C.

CFSE Staining

3.37×10^9 IFU of SvD bacteria were washed in PBS at 20,000 g, 4°C for 20 min. The pellet was resuspended in 500 µl of a 2 µM carboxyfluorescein diacetate succinimidyl ester (CFDA SE) solution (Vybrant® CFDA SE Cell Tracer Kit, Thermofischer Scientific; diluted in PBS) and incubated for 30 min at 37°C. The CFDA SE solution was prewarmed to 37°C. CFDA SE is cell permeable and as soon as it enters cells, its acetate group cleaved by intracellular esterases to form the amin-reactive fluorescent product carboxyfluorescein succinimidyl ester (CFSE). To quench unbound CFSE, 500 µl of ice-cold PBS containing 10% BSA was added, followed by a centrifugation at 20,000 *g*, 4°C for 20 min. The pellet was washed once more in ice-cold PBS containing 10% BSA. The bacteria were fixed by resuspending them in 500 µl of 4.2% formaldehyde (Cytofix®, BD, San Jose, CA). After 20 min incubation at 4°C the bacteria were washed with PBS. The pellet was resuspended in 250 µl PBS and stored at 4°C until usage. 50% of the originally amount of SvD bacteria is lost due to the staining procedure.

Antibodies

Anti-Hirep1 rabbit Ab [anti-serum against the vaccine construct Hirep1, consisting of the VD4 region from *C. trachomatis* serovar D, E, F, fused together (6)], anti-CT043 rabbit Ab (serum), anti-CFP10 Rabbit Ab (serum) (CFP10 is a tuberculosis antigen), Mouse anti-VD4pep4 Ab (serum), mouse anti-CTH522 Ab, anti-SvD Ab (serum taken from infected B6C3F1 mice), mouse anti-chlamydia trachomatis LPS monoclonal Ab, IgG2a (Abnova, Taipei City, Taiwan; Cat. MAB6167, clone CL21–331.1), human serum (from an exposed and a nonexposed individual) described previously (16,17), goat anti-mouse-IgG Alexafluor™647 conjugated IgG (Thermofischer Scientific; Cat. A21235), mouse anti-human CD16—FITC conjugated IgG1 (BD, San Jose, CA; Cat. 560996, clone 3G8), mouse anti-human CD32 – PE-Cy7 conjugated IgG1 (Thermofischer Scientific; Cat. 25–0329-41, clone 6C4), mouse anti-human CD64—PerCP-Cy™5.5 conjugated IgG1 (BD, San Jose, CA; Cat. 561194, clone 10.1).

FCM Based Phagocytosis Assay

The assay was performed in a 96 U-well Nunclon™ delta surface plate (Thermofischer Scientific) with a total volume of 200 µl. CFSE-labeled SvD bacteria and serum samples were diluted in PLB-985 assay media, mixed 1:1 and incubated for 40 min at 37°C on a rocker table. 100 µl of DMF-stimulated PLB-985 cells at a concentration of 2×10^6 cells/ml were then mixed with 40 µl of the bacteria-serum mix. Assay medium was added to each well up to a total volume of 200 µl. The 96 U-well assay plate was incubated for 4 h at 37°C on a rocker table. Afterwards, cells were immediately washed with PBS and kept at 4°C from there on.

For some controls, the stimulated PLB-985 cells were preincubated for 30 min with different dilutions of human Fc receptor binding inhibitor monoclonal Ab (Thermofischer Scientific, Cat. 14–9161-73) or with 20 µl of the actin inhibitor Cytochalasin D (Sigma-Aldrich, St. Louis, MO) before the addition of bacteria-serum mix.

FCM Analysis to Determine Phagocytosis

All samples were measured with a BD FACSCanto equipped with a high throughput sample reader (HTS). Acquiring Software was BD FACSDIVA version 8.0.1. Analysis of the FCS files were performed with FlowJo version 10.3 (FlowJo, LLC, Ashland, Oregon).

The entire staining procedure was performed at 4°C. The PBS was removed and the cells were resuspended in 50 µl fixable viability dye eFluor® 780 (Thermofischer Scientific; Cat. 65–0865-14). After 15 min cells were washed with FACS-buffer (PBS with 2% FBS, 0.1% sodium azide, 1 mM EDTA). The cells were then fixed for 20 min with BD Cytofix® (containing 4.2% formaldehyde) and washed in PBS. Finally, the cells were resuspended in 130 µl PBS. 80 µl of the stained samples were acquired with the HTS. PLB-985 cells were gated on FSC-A versus SSC-A. Doublets and triplets were excluded by gating on FSC-A versus FSC-H. Dead cells were excluded by gating on the negative population on the APC-Cy7 channel. The CFSE signal was then measured in the FITC channel. The baseline for chlamydia-positive cells was set by controls that incubated the phagocytic cells only with the CFSE-labeled bacteria and without any serum.

Ethical Statement

The protocol and procedures employed were reviewed and approved by our institutional review committee. Regarding the two human Abs used in the study, they have been described previously (17) in a study that was approved by the Local Ethical Committee for Copenhagen (01– 008/03). The procedures followed were in accordance with the ethical standards of Local Ethical Committee for Copenhagen on human experimentation and with the Helsinki Declaration of 1975, as revised in 2008.

RESULTS

Labeling *C. trachomatis* with CFSE

To make the phagocytosis assay as simple as possible, we decided to use fluorescently labeled bacteria, thus avoiding the step of intracellular staining of phagocytosed bacteria.

The first objective was to label the bacteria, and measure the labeling by flow cytometry. To label the bacteria, we used CFSE (as explained in materials and methods). Labeling with CFSE occurs inside the bacteria, making it a good method to visualize antibody mediated phagocytosis of bacteria, as it does not interact with surface antigens. At first, *C. trachomatis* (SvD) bacteria were stained with CFSE and analyzed by flow cytometry. The gating strategy is shown in Figure 1A. For comparison, bacteria were stained with an anti-*C. trachomatis* LPS Ab and some were co-stained with the anti-*C. trachomatis*

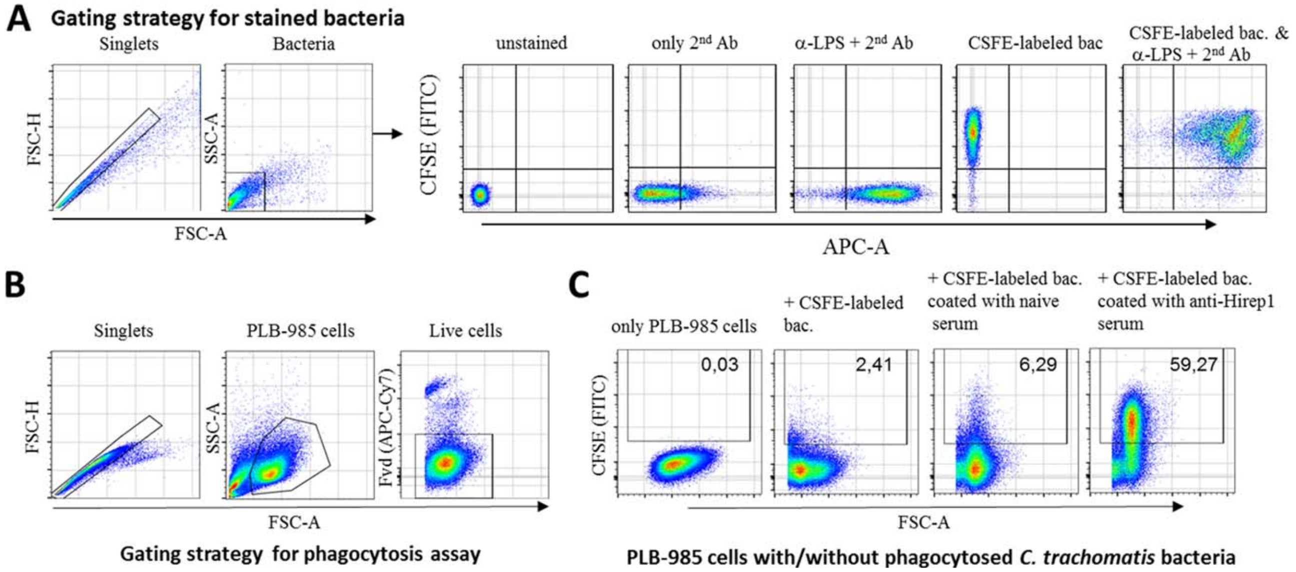

Figure 1. Gating strategies for CFSE-labeled *C. trachomatis* bacteria and phagocytosis assay. All gatings were first set on singlet events (FSC-A vs FSC-H), followed by gating on target cell population (FSC-A vs. SSC-A). **(A)** Bacteria were then shown in APC-A versus FITC-A (stained either with mouse anti-*C. trachomatis* LPS monoclonal Ab and a goat anti-mouse-IgG-Alexaflour^{TM}647 secondary Ab or labeled with CFSE). **(B)** PLB-985 cells were stained with fixable viability dye eFluor® 780 (FvD) and gated on living cells with FSC-A versus APC-Cy7-A. **(C)** CFSE-labeled SvD bacteria were preincubated with no serum, serum from naïve rabbits, or serum from rabbits vaccinated with Hirep1 for 40 min at 37°C and incubated for 4 h with DMF-stimulated PLB-985 cells. CFSE-signal was measured by flow cytometry in the FITC channel. Cells were gated on CFSE-positive (=phagocytosing) events. Pseudo-color dot plots show PLB-985 cells alone or after incubation with noncoated or coated bacteria.

LPS Ab and CFSE-labeled. The data showed an efficient labeling with CFSE, and an almost complete co-staining of anti-*C. trachomatis* LPS on CFSE-labeled bacteria (Fig. 1A). Moreover, CFSE labeling and fixation did not affect phagocytosis of the bacteria, as we observed similar phagocytosis of CFSE labeled and nonlabeled bacteria (Supporting Information Fig. S1).

Antibody Mediated Uptake of Bacteria

We next coated the CFSE labeled SvD bacteria with different concentrations of rabbit polyclonal Abs directed against Hirep1. The Hirep1 vaccine construct is based on the *C. trachomatis* Major Outer Membrane Protein (MOMP), and is known to induce neutralizing antibodies [(6) and Olsen et al. unpublished observations)]. We measured the uptake of Ab-coated bacteria by PLB-985 cells, an immature myeloid cell line, which was differentiated by DMF treatment for 5 days into terminally mature neutrophils, closely mimicking the functions of blood neutrophils (18). The measurement was performed by flow cytometry and the gating strategy for measuring uptake of CFSE labeled bacteria into PLB-985 cells is shown in Figure 1B.

Control stainings are shown in Figure 1C. It shows a comparison of PLB-985 cells with PLB-985 cells being subjected to CFSE-labeled *C. trachomatis* bacteria (noncoated or precoated with anti-Hirep1 serum or naïve serum). Although some phagocytosis was observed by adding CFSE labeled bacteria (noncoated or coated with naïve serum) to PLB-985 cells, the phagocytosis increased when adding *C. trachomatis* bacteria that had been coated with anti-Hirep1 serum (Fig. 1C). At MOIs of 10, 20, or 40, anti-Hirep1 Abs induced a strong

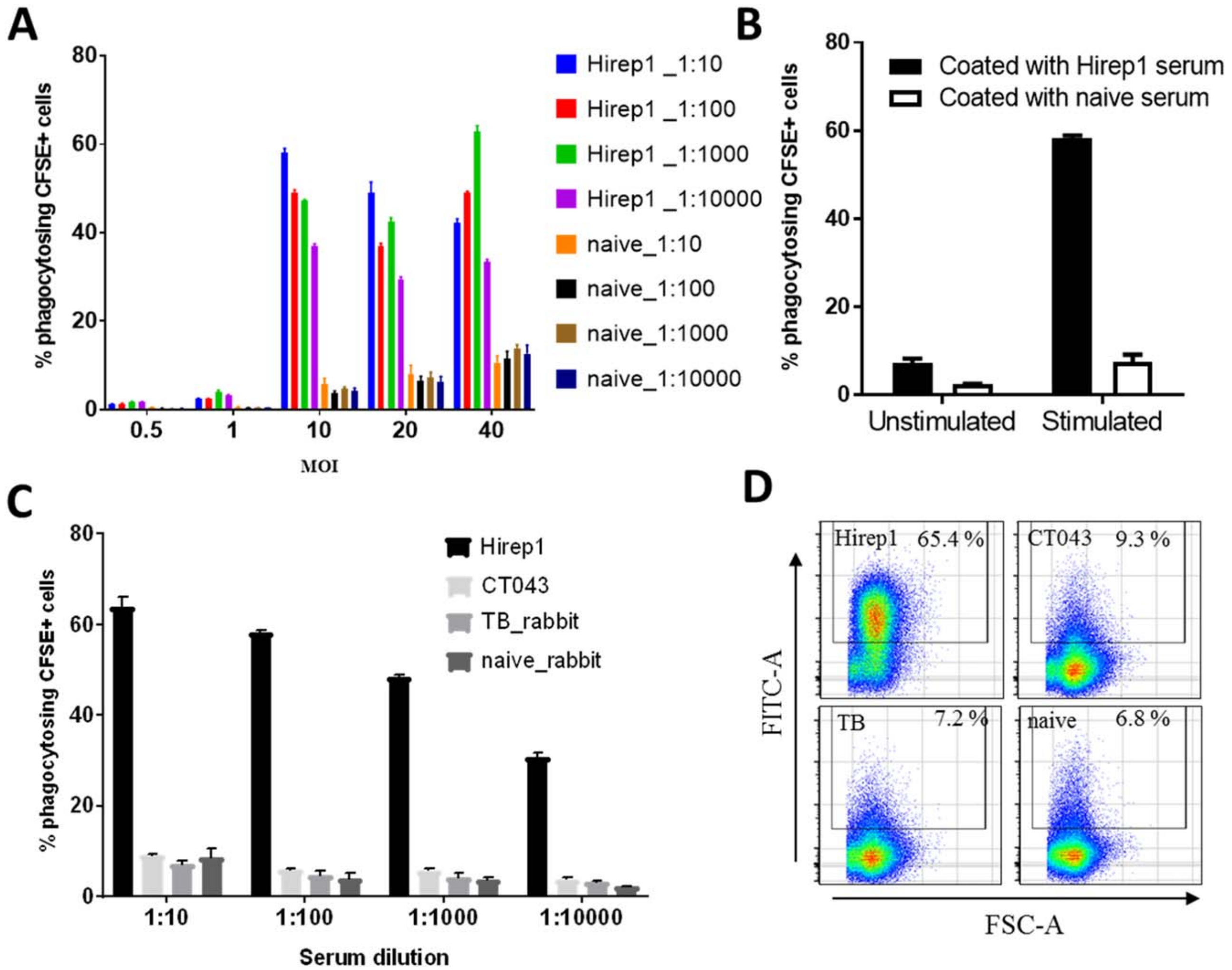

Figure 2. Antibody mediated phagocytosis. CFSE-labeled SvD bacteria were pre-incubated with serum of vaccinated and naïve rabbits for 40 min at 37 °C and incubated for 4 h with DMF-stimulated PLB-985 cells. CFSE-signal was measured by flow cytometry in the FITC channel. Cells were gated on CFSE-positive (=phagocytosing) events. **(A)** Bacteria were titrated from MOI 0.5 to MOI 40 and sera from naïve and Hirep1-vaccinated rabbits were titrated from a 1:10 to a 1:10000 dilution. **(B)** Unstimulated and DMF-stimulated PLB-985 cells were incubated with serum-coated CFSE-labeled SvD bacteria at MOI 10. **(C)** SvD bacteria at MOI 10 were incubated with different rabbit sera that were titrated 1:10 to 1:10000. Phagocytosis was measured by flow cytometry. **(D)** Representative pseudo-color dot plots of DMF-stimulated PLB-985 cells in FSC-A vs FITC-A with different rabbit sera at a dilution of 1:10 and SvD bacteria at MOI of 10. Mean and SD at a sample size of $n = 3$ are shown (A to C).

Table 1. Intra and Interassay coefficient of variation

	% PHAGOCYTOSING CFSE+ PLB-985 CELLS					
EXP. NUMBER	REPLICATE 1	REPLICATE 2	REPLICATE 3	MEAN	SD	INTRA CV (%)
1	57.4	57.4	59.2	58.00	0.85	1.46
2	65.4	65.1	61.5	64.00	1.77	2.77
3	62.3	62.9	61.2	62.13	0.70	1.13
4	60.4	62.2	59.5	60.70	1.12	1.85
5	59.3	57.1	58.5	58.30	0.91	1.56
			Inter CV (%)	3.76		

phagocytosis. Approximately 58% of PLB-985 cells stained positive for *C. trachomatis* (at MOI 10) (Fig. 2A). Decreasing the concentration of the Abs led, as expected, to a decrease in phagocytosis to 37% at a serum dilution of 1:10,000. Significantly less positive cells were observed in the presence of serum from naïve animals (Fig. 2A). We choose a MOI of 10 as the bacteria-to-cell ratio we would use in this assay. Furthermore, we noted that the phagocytosing capability of the PLB-985 cells increased following stimulation with DMF (Fig. 2B). To determine the variability of the phagocytosis assay it was repeated in five independent experiments with anti-Hirep1 Ab coated CFSE-labeled bacteria at a serum dilution of 1:10 and bacteria concentration of MOI 10 with DMF stimulated PLB-985 cells. The intra-assay coefficient of variation (CV) was between 1.13 and 2.77% and the interassay CV was 3.76% (Table 1). We, therefore, conclude that the assay is reproducible using a serum dilution of 1:10 and bacteria concentration of MOI 10. Using serum dilutions of 1:100–1:10,000 gave, as expected, a reduced phagocytosis and a higher CV value, although even with a dilution of 1:10,000, the assay was reproducible (Supporting Information Fig. S2).

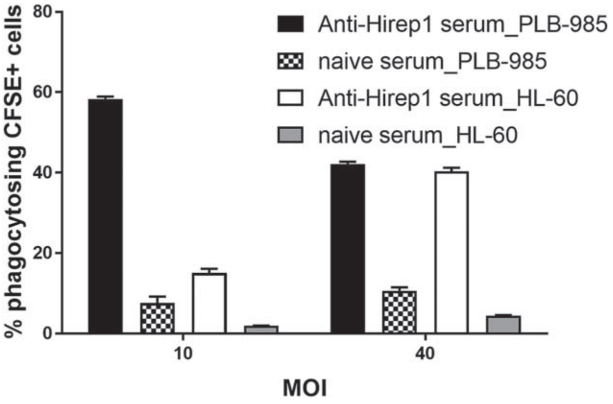

Figure 3. Comparison of phagocytosis by PLB-985 and HL-60 cells. CFSE-labeled SvD bacteria at MOIs of 10 and 40 were incubated with 1:10 diluted sera of naïve and Hirep1 vaccinated rabbits. DMF-stimulated PLB-985 and HL-60 cells were then incubated with the coated bacteria. Phagocytosis was measured by flow cytometry. Mean and SD are shown at a sample size of $n = 3$.

We next compared the anti-Hirep1 Ab with a rabbit antiserum directed against another chlamydial surface-exposed antigen, the CT043 antigen (19). Interestingly, in contrast to the anti-Hirep1 Ab, an Ab directed against the CT043 antigen did not induce phagocytosis, demonstrating that being surface exposed does not automatically lead to phagocytosis. We also tested a control serum from rabbits vaccinated with a tuberculosis antigen ["H56" (20)]. As expected, this Ab did also not induce phagocytosis (Figs. 2C and 2D).

Finally, we also tested the FCM assay with HL-60 cells, another neutrophilic cell line that is used in several laboratories. CFSE labeled bacteria coated with the anti-Hirep1 Ab were added to DMF stimulated HL-60 cells and phagocytosis was measured by FCM, as explained above. The results showed that at a MOI of 40 HL-60 and PLB-985 cells showed a similar phagocytosis (Fig. 3). However, at a MOI of 10, PLB-985 cells showed a significantly higher phagocytosis compared to HL-60 cells.

Taken together, using a rabbit Ab specific for MOMP, we could show phagocytosis of the CFSE labeled bacteria. The percentage of phagocytosing cells was dependent on the amount of Ab used. Compared to the naïve rabbit control serum, no increase in phagocytosis was observed with antibodies directed against a tuberculosis antigen or with an anti-CT043 Ab.

Inhibition of Phagocytosis

We next wanted to explore the mechanism behind the observed phagocytosis. As expected, the Fcγ receptors (CD16 and CD32) were expressed on PLB-985 cells and CD64 on ~40% of the cells (Fig. 4A). To confirm that the phagocytosis was dependent on Fcγ receptors, we examined the effect of inhibiting the binding of anti-Hirep1 Abs to the Fcγ receptors, on the ability of anti-Hirep1 Abs to induce phagocytosis. Stimulated PLB-985 cells were preincubated with three different dilutions of human Fcγ receptor binding inhibitor polyclonal Ab (1:4, 1:10, 1:100), prior to incubation with CFSE-labeled bacteria coated with the anti-Hirep1 Ab. The result showed that in the absence of preincubation with Fcγ receptor inhibitor, approximately 60% of the PLB-985 cells were SvD positive (Fig. 4B). Preincubation with Fcγ receptor inhibitor reduced the phagocytosis in a concentration dependent manner (Figs. 4B and 4D) from 60% to 11%. Thus, efficient phagocytosis was dependent on an intact interaction between the Ab coated bacteria and the Fcγ receptors.

Several reports have shown that Fc receptor mediated internalization involve polymerization of actin (21,22). Therefore, preventing actin polymerization should inhibit internalization. To test this, PLB-985 cells were preincubated with Cytochalasin D, an inhibitor of actin polymerization, before the addition of bacteria-serum mix. At all concentrations tested, Cytochalasin D blocked Ab mediated phagocytosis of the labeled bacteria (Figs. 4C and 4D).

In summary, PLB-985 cells stained positive for CD16 and CD32 and partially for CD64. Moreover, using the FCM phagocytosis assay, we show that anti-Hirep1 Ab induced

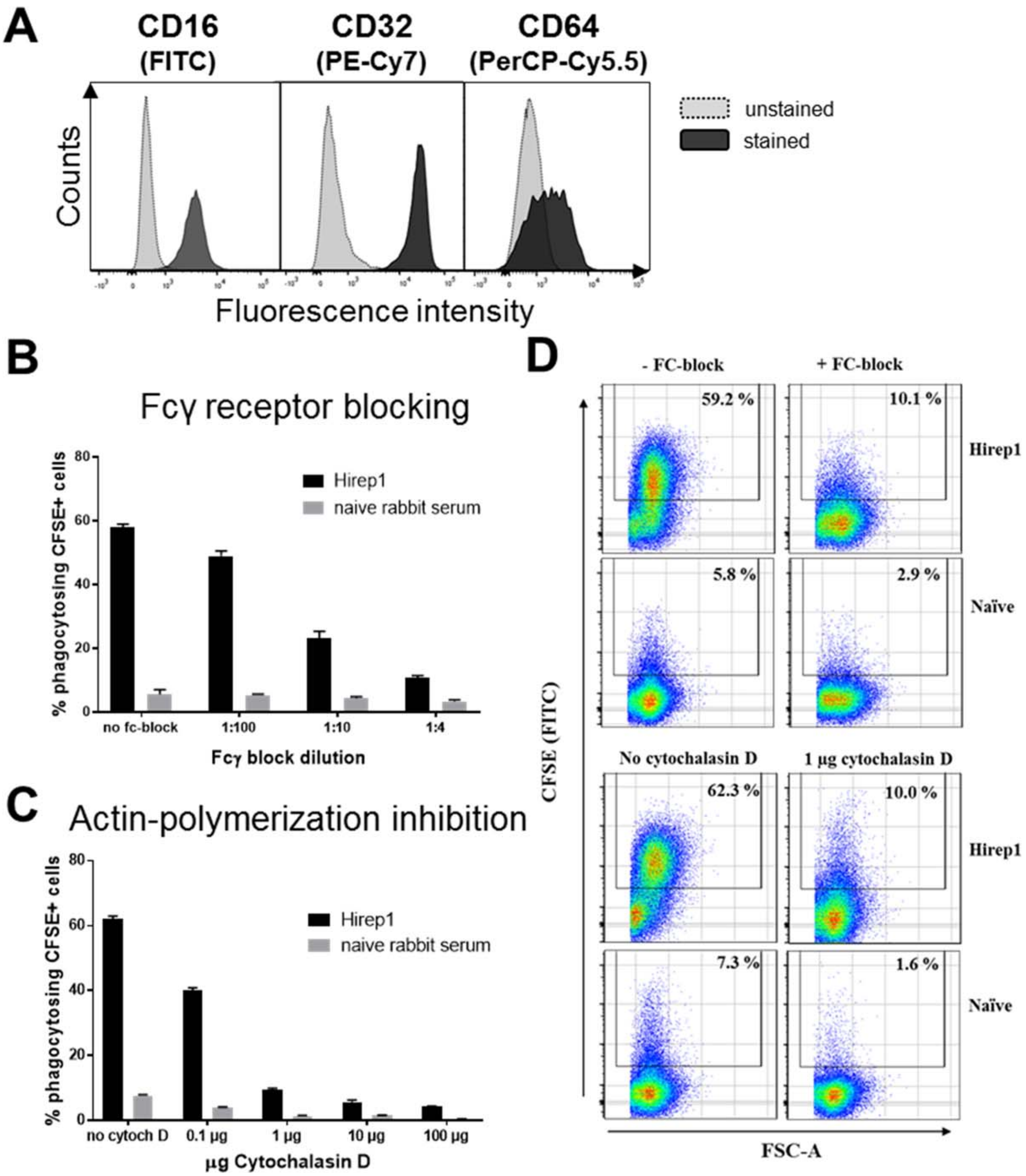

Figure 4. Dependence of phagocytosis on Fcγ receptors and actin polymerization. **(A)** Expression of CD16, CD32 and CD64 on the surface of DMF stimulated PLB-985 cells. **(B)** CFSE-labeled SvD bacteria at a MOI of 10 were incubated with 1:10 diluted sera of naïve and Hirep1 vaccinated rabbits and given to DMF stimulated PLB-985 cells that were either pre-incubated with different dilutions of human Fcγ-receptor-block (1:4, 1:10, 1:100), or with **(C)** different concentrations of Cytochalasin D (0.1 µg, 1 µg, 10 µg, 100 µg); **(D)** Phagocytosis of PLB-985 cells was measured by flow cytometry. Representative pseudo-color dot plots of treatment with Fcγ-receptor-block (1:4) or Cytochalasin D (1 µg) in comparison to untreated PLB-985 cells. Mean and SD are shown at a sample size of $n = 3$ (B and C).

phagocytosis could be blocked by an Fcγ receptor inhibitor, or by inhibiting the polymerization of actin.

Phagocytosis Mediated by Human and Murine Serum

An obvious use for a FCM based phagocytosis assay is the high-throughput testing of serum samples from human donors, or samples from mice vaccinated with different vaccine candidates. It was, therefore, important to show that the assay is also suitable for human and murine serum. We used serum from mice infected with *C. trachomatis* SvD and serum from mice immunized with a construct containing the neutralizing epitope in the VD4 region of MOMP, “VD4p4.” In addition, we tested a murine monoclonal Ab specific for *C. trachomatis* LPS.

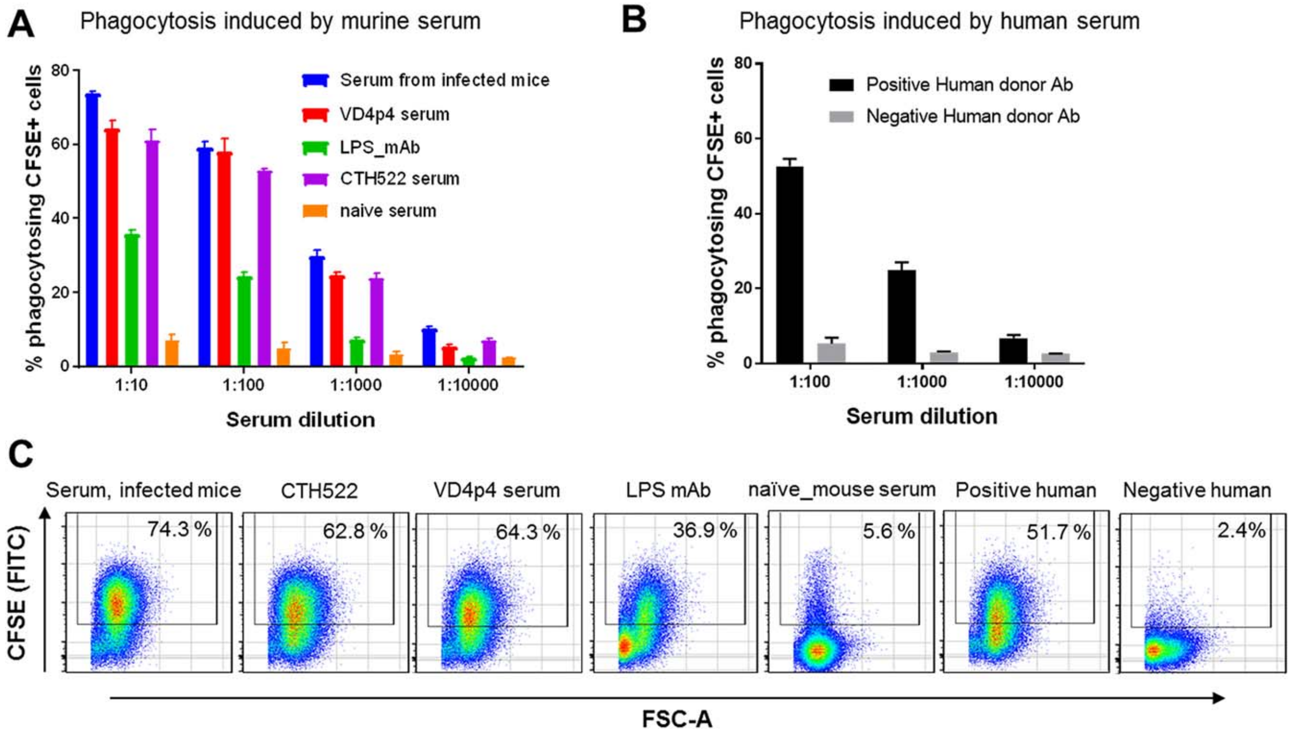

Figure 5. Phagocytosis assay using human and murine serum. CFSE-labeled SvD bacteria at a MOI of 10 were incubated with **(A)** serum from infected/vaccinated mice or a monoclonal mouse-a-*C. trachomatis* LPS Ab, or **(B)** serum from an infected human donor. Serum of naïve mice/humans were used as negative controls. Murine sera were titrated from 1:10 to 1:10000 (*C. trachomatis* LPS mAb was pre-diluted to 1 ng/μl) and human sera from 1:100 to 1:10000. Phagocytosis was measured by flow cytometry. **(C)** Representative pseudo-color dot plots of the phagocytosis assay with all sera at a dilution of 1:10 (for human sera 1:100). Mean and SD are shown at a sample size of n = 3 (A and B).

The assay was performed in the same way as shown above with the rabbit serum. CFSE-labeled SvD *C. trachomatis* bacteria were coated with diluted serum samples (1:10–1:10,000), and subsequently incubated with the DMF-stimulated PLB-985 cells for 4 h, before being subjected to FCM analysis.

Both serum from infected and immunized mice induced phagocytosis (Fig. 5A). A murine anti-*C. trachomatis* LPS mAb also induced phagocytosis in a dose-dependent manner (Fig. 5A).

We also tested serum from a human donor with a confirmed genital SvD infection. We choose a donor that we have previously shown to possess Abs directed against MOMP SvD (16,17). In contrast to serum from a nonexposed “naïve” human donor, the serum from the exposed human donor induced a strong phagocytosis leading to 52.6% positive PLB-985 cells (Fig. 5B).

Taken together, the assay showed to be applicable for both human and murine serum. Murine Abs directed against the VD4 region from MOMP induced phagocytosis of the *C. trachomatis* bacteria, whereas serum from nonvaccinated mice did not. Anti-LPS Abs also induced phagocytosis.

DISCUSSION

The flow cytometry assay was recently shown to be an alternative to microscopy in terms of counting and titrating bacteria (23). In this article, we show that flow cytometry is also suitable for high-throughput testing of the phagocytosing ability of an Ab directed against an intracellular bacterium, in our case *C. trachomatis*.

For the FACS based phagocytosis assay, we used CFSE labeled bacteria. While others have also used CFSE labeling to visualize the appearance of bacteria in target cells (24), there are other options, such as fluorescein isothiocyanate (FITC) or a pH sensitive dye pHrodo^{TM} (25,26). FITC is an amine group reactive compound that binds to every protein, which is also true for CFSE. However, we used CFDA SE, which is a cell permeable dye. Once inside the bacteria, intracellular esterases cleave the acetate groups, which results in the reactive CFSE form. Thus, this method provides an intrabacterial labeling, while FITC stains the outside of the bacteria. The pH sensitive pHrodo dye is labeling the bacteria in the same way as CFDA SE. However, the dye will change its excitation maximum according to the pH, and this allows a distinction between bacteria in a neutral pH environment, such as on the surface of cells, or bacteria in an acidic intracellular environment, such as the phagolysosomes. In future experiments, we will compare the different staining methods. It should be noted that the pHrodo dye in general is more expensive than CFDA SE, which is an important factor to consider in the development of a high throughput assay, to be used with many samples.

We observed 50–70% of phagocytosing cells after coating bacteria with serum of vaccinated or infected animals/individuals in our in vitro assay. Phagocytosis was observed not only with human serum, but also with murine and rabbit serum.

The ability of IgG from different species to bind to human Fc receptors is in agreement with previous studies (27–30). Fabbrini et al. developed an Ab dependent phagocytosis assay for Group B Streptococcus (26). They used the human neutrophil-like HL-60 cell line. They also tested different murine and rabbit sera from vaccinated animals and achieved a phagocytic uptake of approximately 60%. We also tested the HL-60 cell line, and found HL-60 cells also efficiently phagocytosed Ab coated bacteria, although requiring higher MOIs than with PLB-985 cells. The specificity and sensitivity of the FCM-based assay was not compared with the standard microscopy assay.

The phagocytosis in our assay was Fcγ receptor and actin polymerization dependent as blocking FcR binding or actin polymerization prevented uptake of the bacteria (Fig. 4). The FcR blocking reagent is known to bind Fcg receptors, indicating a role for these receptors in mediating the phagocytosis. All the Fcγ receptors are capable of endocytosis, and the precise role for each of the individual Fcγ receptors in phagocytosing *C. trachomatis* requires further experiments (31,32). Interestingly, the FACS assay could distinguish between a binding nonphagocytosing Ab (directed against CT043) and a binding phagocytosing Ab (directed against Hirep1) (Fig. 2C). As phagocytosis require crosslinking of the Fc receptor (33), it could be speculated that the lack of phagocytosis with the CT043 Ab is due to the CT043 antigen being too far apart on the chlamydial surface for the binding Abs to crosslink the Fc receptor on the phagocyte.

We also tested an LPS mAb and found that despite a complete lack of neutralizing capability (data not shown), this mAb was, however, able to induce phagocytosis of *C. trachomatis* (Fig. 5). Thus, this mAb could be used to selectively study the phagocytosis of *C. trachomatis*.

In conclusion, we have developed a simple, rapid, reproducible flow cytometric based assay that use cultivable effector/target cells and is able to handle a large number of samples.

Acknowledgments

The funders had no role in study design, data collection and analysis, decision to publish, or preparation of the manuscript. The authors do not have a commercial or other association that poses a conflict of interest. The authors thank Helene Bæk Juel for critically reading the manuscript. The authors thank Lene Rasmussen and Sharmila Subratheepam for excellent technical assistance.

Literature Cited

1. de la Maza LM, Zhong G, Brunham RC. Update on *Chlamydia trachomatis* vaccinology. Clin Vaccine Immunol 2017;24:e00543-16.
2. Poston TB, Darville T. Chlamydia trachomatis: Protective adaptive responses and prospects for a vaccine. Curr Top Microbiol Immunol (in press).
3. Picard MD, Bodmer JL, Gierahn TM, Lee A, Price J, Cohane K, Clemens V, DeVault VL, Gurok G, Kohberger R, et al. Resolution of Chlamydia trachomatis infection is associated with a distinct T cell response profile. Clin Vaccine Immunol 2015;22:1206–1218.
4. Lampe MF, Wilson CB, Bevan MJ, Starnbach MN. Gamma interferon production by cytotoxic T lymphocytes is required for resolution of Chlamydia trachomatis infection. Infect Immun 1998;66:5457–5461.
5. Li LX, McSorley SJ. A re-evaluation of the role of B cells in protective immunity to Chlamydia infection. Immunology Lett 2015;164:88–93.
6. Olsen AW, Follmann F, Erneholm K, Rosenkrands I, Andersen P. Protection against Chlamydia trachomatis infection and upper genital tract pathological changes by vaccine-promoted neutralizing antibodies directed to the VD4 of the major outer membrane protein. J Infect Dis 2015;212:978–989.
7. Clynes RA, Towers TL, Presta LG, Ravetch JV. Inhibitory Fc receptors modulate in vivo cytoxicity against tumor targets. Nat Med 2000;6:443–446.
8. Johnson P, Glennie M. The mechanisms of action of rituximab in the elimination of tumor cells. Semin Oncol 2003;30:3–8.
9. Schmidt RE, Gessner JE. Fc receptors and their interaction with complement in autoimmunity. Immunol Lett 2005;100:56–67.
10. Hessell AJ, Hangartner L, Hunter M, Havenith CEG, Beurskens FJ, Bakker JM, Lanigan CMS, Landucci G, Forthal DN, Parren PWHI, et al. Fc receptor but not complement binding is important in antibody protection against HIV. Nature 2007; 449:101–104.
11. Ackerman ME, Barouch DH, Alter G. Systems serology for evaluation of HIV vaccine trials. Immunol Rev 2017;275:262–270.
12. Moore T, Ananaba GA, Bolier J, Bowers S, Belay T, Eko FO, Igietseme JU. Fc receptor regulation of protective immunity against Chlamydia trachomatis. Immunology 2002;105:213–221.
13. Moore T, Ekworomadu CO, Eko FO, MacMillan L, Ramey K, Ananaba GA, Patrickson JW, Nagappan PR, Lyn D, Black CM, et al. Fc receptor-mediated antibody regulation of T cell immunity against intracellular pathogens. J Infect Dis 2003;188:617–624.
14. Naglak EK, Morrison SG, Morrison RP. Gamma interferon is required for optimal antibody-mediated immunity against genital chlamydia infection. Infection Immun 2016;84:3232–3242.
15. Olsen AW, Follmann F, Jensen K, Hojrup P, Leah R, Sorensen H, Hoffmann S, Andersen P, Theisen M. Identification of CT521 as a frequent target of Th1 cells in patients with urogenital Chlamydia trachomatis infection. J Infect Dis 2006;194: 1258–1266.
16. Follmann F, Olsen AW, Jensen KT, Hansen PR, Andersen P, Theisen M. Antigenic profiling of a Chlamydia trachomatis gene-expression library. J Infect Dis 2008;197: 897–905.
17. Olsen AW, Follmann F, Højrup P, Leah R, Sand C, Andersen P, Theisen M. Identification of human T-cell targets recognized during the Chlamydia trachomatis genital infection. J Infect Dis 2007;196:1546–1552.
18. Pedruzzi E, Fay M, Elbim C, Gaudry M, Gougerot-Pocidalo MA. Differentiation of PLB-985 myeloid cells into mature neutrophils, shown by degranulation of terminally differentiated compartments in response to N-formyl peptide and priming of superoxide anion production by granulocyte-macrophage colony-stimulating factor. Br J Haematol 2002;117:719–726.
19. Meoni E, Faenzi E, Frigimelica E, Zedda L, Skibinski D, Giovinazzi S, Bonci A, Petracca R, Bartolini E, Galli G, et al. CT043, a protective antigen that induces a CD4+ Th1 response during Chlamydia trachomatis infection in mice and humans. Infect Immun 2009;77:4168–4176.
20. Aagaard C, Hoang T, Dietrich J, Cardona PJ, Izzo A, Dolganov G, Schoolnik GK, Cassidy JP, Billeskov R, Andersen P. A multistage tuberculosis vaccine that confers efficient protection before and after exposure. Nat Med 2011;17:189–U224.
21. May RC, Machesky LM. Phagocytosis and the actin cytoskeleton. J Cell Sci 2001;114: 1061–1077.
22. Diakonova M, Bokoch G, Swanson JA. Dynamics of cytoskeletal proteins during Fc gamma receptor-mediated phagocytosis in macrophages. Mol Biol Cell 2002;13:402–411.
23. Käser T, Pasternak JA, Hamonic G, Rieder M, Lai K, Delgado-Ortega M, Gerdts V, Meurens F. Flow cytometry as an improved method for the titration of Chlamydiaceae and other intracellular bacteria. Cytometry A 2016;89A:451–460.
24. Schnitger K, Njau F, Wittkop U, Liese A, Kuipers JG, Thiel A, Morgan MA, Zeidler H, Wagner AD. Staining of Chlamydia trachomatis elementary bodies: a suitable method for identifying infected human monocytes by flow cytometry. J Microbiol Methods 2007;69:116–121.
25. Oberley RE, Ault KA, Neff TL, Khubchandani KR, Crouch EC, Snyder JM. Surfactant proteins A and D enhance the phagocytosis of Chlamydia into THP-1 cells. Am J Physiol Lung Cell Mol Physiol 2004;287:L296–L306.
26. Fabbrini M, Sammicheli C, Margarit I, Maione D, Grandi G, Giuliani MM, Mori E, Nuti S. A new flow-cytometry-based opsonophagocytosis assay for the rapid measurement of functional antibody levels against Group B Streptococcus. J Immunol Methods 2012;378:11–19.
27. Lubeck MD, Steplewski Z, Baglia F, Klein MH, Dorrington KJ, Koprowski H. The interaction of murine IgG subclass proteins with human monocyte Fc receptors. J Immunol 1985;135:1299–1304.
28. Jonsson F, Mancardi DA, Kita Y, Karasuyama H, Iannascoli B, Van Rooijen N, Shimizu T, Daeron M, Bruhns P. Mouse and human neutrophils induce anaphylaxis. J Clin Invest 2011;121:1484–1496.
29. McCool D, Birshtein BK, Painter RH. Structural requirements of immunoglobulin G for binding to the Fc gamma receptors of the human tumor cell lines U937, HL-60, ML-1, and K562. J Immunol 1985;135:1975–1980.
30. Flinsenberg TW, Compeer EB, Koning D, Klein M, Amelung FJ, van Baarle D, Boelens JJ, Boes M. Fcgamma receptor antigen targeting potentiates cross-presentation by human blood and lymphoid tissue BDCA-3+ dendritic cells. Blood 2012;120:5163–5172.
31. Sanders LA, Feldman RG, Voorhorst-Ogink MM, de Haas M, Rijkers GT, Capel PJ, Zegers BJ, van de Winkel JG. Human immunoglobulin G (IgG) Fc receptor IIA (CD32) polymorphism and IgG2-mediated bacterial phagocytosis by neutrophils. Infect Immun 1995;63:73–81.
32. Amigorena S, Bonnerot C. Fc receptor signaling and trafficking: a connection for antigen processing. Immunol Rev 1999;172:279–284.
33. Aderem A, Underhill DM. Mechanisms of phagocytosis in macrophages. Annu Rev Immunol 1999;17:593–623.

ORIGINAL ARTICLE

ISAC CYTOMETRY Journal of Quantitative Cell Science PART A

Flow cytometry: An accurate tool for screening P2RX7 modulators

Amélie Barczyk[1] | Hélène Bauderlique-Le Roy[2] | Nathalie Jouy[3] | Nicolas Renault[1] | Audrey Hottin[1] | Régis Millet[1] | Valérie Vouret-Craviari[4] | Sahil Adriouch[5] | Thierry Idziorek[3,6] | Xavier Dezitter[1]

[1]Univ. Lille, Inserm, CHU Lille, U1286 – Infinite – Institute for Translational Research in Inflammation, Lille, France

[2]Univ. Lille, UMS 2014-US 41 PLBS BICel, Flow Cytometry Core Facility, Institut Pasteur de Lille, Lille cedex, France

[3]Univ. Lille, UMS 2014-US 41 PLBS BICel, Flow Cytometry Core Facility, IRCL, 1 place de Verdun, Lille cedex, France

[4]University Cote d'Azur, Institute for Research on Cancer and Aging, IRCAN U1081 UMR CNRS 7284, Nice, France

[5]Normandie University, UNIROUEN, INSERM, U1234, Pathophysiology, Autoimmunity, Neuromuscular Diseases and Regenerative THERapies (PANTHER), Rouen, France

[6]Univ. Lille, CNRS, Inserm, CHU Lille, Institut de Recherche contre le Cancer de Lille, UMR9020 – UMR-S 1277 - Canther – Cancer Heterogeneity, Plasticity and Resistance to Therapies, Lille, France

Correspondence

Xavier Dezitter, Institut de Chimie Pharmaceutique Albert Lespagnol, Université de Lille, INSERM U1286 – Infinite – Institute for Translational Research in Inflammation, 3, rue du Professeur Laguesse BP 83, 59006 Lille, France.
Email: xavier.dezitter@univ-lille.fr

Funding information

Centre National de la Recherche Scientifique; Institut National de la Santé et de la Recherche Médicale; Institut National Du Cancer; University of Lille

Abstract

The P2X purinergic receptor 7 (P2RX7) is a poorly selective ATP-gated ion channel. Although P2RX7 binds ATP with relatively low affinity, prolonged activation can lead to nonselective membrane pore formation. Indeed, brief exposure to ATP triggers a rapid Ca^{2+} influx, whereas prolonged exposure to high ATP concentrations results in the passage of larger organic molecules. P2RX7 is involved in the physiopathology of a number of diseases and has notably emerged as a potential therapeutic target in inflammation, neuropathic pain, Alzheimer's disease, and cancer—prompting growing interest in the synthesis of novel P2RX7 modulators and the development of reliable, stringent screening methods. In the present study, we developed methods based on conventional flow cytometry, imaging flow cytometry and spectral flow cytometry and used them to measure P2RX7's activity upon activation by 3'-O-(4-benzoyl)benzoyl ATP. We also demonstrated the use of the highly sensitive DNA-intercalating dye TO-PRO-3 to determine P2RX7's large pore activity. The simultaneous quantification of calcium influx (Fluo-3 AM), large pore opening (TO-PRO-3), and viability (propidium iodide) is a very efficient method for low- to medium-throughput screening of P2RX7 modulators. Agonist and antagonist potencies can be accurately evaluated. Spectral cytometry notably enabled us to assay several biological activities while correcting for the intrinsic fluorescence of the screened compounds—otherwise a well-known limitation of fluorescence-based screening. Hence, spectral cytometry appears to be a useful, novel tool for drug candidate screening.

KEYWORDS

drug discovery, flow cytometry, imaging flow cytometry, P2RX7, screening, spectral cytometry

1 | INTRODUCTION

The P2X purinergic receptor 7 (P2RX7) is a poorly selective ATP-gated ion channel that binds ATP with relatively low affinity. In humans, P2RX7 is expressed in many cell types, including immune cells (macrophages and microglia) and cells in the central and peripheral nervous systems [1]. P2RX7 has an essential role in inflammation, innate immunity, tumor progression, neurodegenerative diseases, and several other diseases [1].

Brief exposure of P2RX7 to extracellular ATP induces rapid channel opening and thus Ca^{2+} and Na^{+} influx, and K^{+} efflux. In contrast,

---

Amélie Barczyk, Hélène Bauderlique-Le Roy, and Nathalie Jouy contributed equally to this work.

prolonged exposure to ATP leads to the formation of a poorly selective membrane pore that allows the passage of molecules of up to 900 Da in weight. For decades, two competing mechanistic hypotheses were considered with regard to the large pore opening [2–4]: the enlargement of the P2RX7 cation channel, and the recruitment of a partner protein (e.g., pannexin-1) [5]. It is now acknowledged that upon activation, P2RX7's ion channel becomes immediately permeable to large molecules [6–10].

P2RX7 signalling affects major cell functions and cell fate and depends on the cellular context. In the setting of inflammation, P2RX7 activation triggers inflammasome assembly and release of pro-inflammatory cytokines (such as IL-1β and IL-18) [11,12]. In many cell subtypes (including tumor cell lines in vitro), P2RX7 acts as a cell death inducer by disrupting plasma membrane permeability [13]. In vivo, P2RX7's role in tumor progression and metastasis is more complex, and depends on (i) tumor microenvironment factors (e.g., the extracellular ATP concentration, or the type and abundance of ecto-ATPase), and (ii) the expression levels and functional status of the P2RX7 variants expressed at the surface of tumor cells [14–17]. Adding to this complexity, tonic low-level P2RX7 activation in cancer cells is associated with faster in vivo tumor growth; indeed, in some models, P2RX7 antagonists have antitumor effects [16,18]. In the mouse, however, P2RX7 knock-out, loss-of-function *P2RX7* gene polymorphisms, and pharmacological inhibition are associated with tumor progression, due to the impairment of antitumor immune responses [19–21]. The net effect of P2RX7 pharmacological modulation on tumor progression therefore appears to depend on the type of cancer and on the balance between direct pharmacological effects on cancer cells and impairment of the host immune system [22].

Despite the complexity of the purinergic pathways, decades of accumulated scientific evidence have prompted the scientific community and pharmaceutical companies to develop P2RX7 modulators as drug candidates in the treatment of cancer, inflammatory diseases, and other emerging clinical indications. These drug candidates range from small molecules to P2RX7-specific antibodies and nanobodies [23,24]. The reliable, stringent screening of drug candidates is therefore essential in this context. P2RX7 pharmacology has been intensely studied with electrophysiological methods (e.g., patch-clamp techniques) and microscopy- or microplate-based fluorescent dye assays. The P2RX7 ion channel has mainly been studied using electrophysiological techniques (whole-cell current clamping), but automated patch clamp is necessary for screening large series of compounds. P2RX7-mediated calcium influx has also been studied in microscopy- or microplate-based assays with fluorescent probes like Fluo-3 AM or Fluo-4 AM [4]. The opening of P2RX7 large pore is usually measured through the entry of high-molecular-weight cationic fluorescent dyes (such as ethidium [394 Da as ethidium bromide], propidium [668 Da as propidium iodide, PI], or YO-PRO-1 [629 Da as YOPRO-1 iodide]) or anionic fluorescent dyes (such as Lucifer yellow [457 Da as the lithium salt] or fluorescein [376 Da as the sodium salt]) [4]. These dye uptake assays are suitable for high-throughput screening.

Flow cytometry has already been used to separately measure calcium influx and dye uptake in independent experiments [25–28]. In the present study, we used flow cytometry to simultaneously assess Ca^{2+} influx, large pore opening, and cell viability upon activation of P2RX7 by 3'-O-(4-benzoyl)benzoyl ATP (BzATP). Flow cytometry has the advantage of excluding dead cells that interfere with the measurement of large pore opening. The simultaneous quantification of both calcium influx (high Ca^{2+}) and large pore opening proved to be an excellent method for compound screening and for measuring the potency (as the half maximal effective concentration EC_{50} or the half maximal inhibitory concentration IC_{50}) of both agonists and antagonists. Furthermore, we better defined the biological activity of compounds of interest by exploiting the advantageous properties of spectral cytometry.

2 | MATERIALS AND METHODS

2.1 | Reagents

BzATP was purchased from Sigma-Aldrich (St. Louis, MO). AZ11645373 was purchased from Tocris (Ellisville, MO). The fluorescent dyes Fluo-3 AM, YO-PRO-1, TO-PRO-3, PI, 7-AAD and Hoechst 33342 were purchased from Life Technologies (Carlsbad, CA). The synthesized compounds were prepared in DMSO.

2.2 | Cell culture

HEK-293 cells stably expressing human or mouse P2RX7 were established as described [29]. The cells were cultured in DMEM medium with Glutamax (Life Technologies), supplemented with 10% heat-inactivated foetal calf serum, 1000 UI/ml penicillin, 1000 μg/ml streptomycin and incubated at 37°C in 5% CO_2. Stable cell lines were grown in medium supplemented with 5 μg/ml blasticidin (Sigma-Aldrich), in order to select P2RX7-overexpressing cells.

2.3 | Fluorescence analysis using a plate reader

For intracellular calcium concentration measurement, the cells were harvested and loaded (10^6 cells/ml) with the calcium indicator Fluo-3 AM (500 nM) for 30 min in culture medium without foetal calf serum at 37°C. The cells were then centrifuged at 230*g* for 5 min and resuspended in sucrose buffer (20 mM HEPES, 300 mM sucrose, 5 mM KCl, 1 mM $MgCl_2$, 1 mM $CaCl_2$, 10 mM glucose, and pH 7.4) and placed in a 96 well plate. The cells were treated with BzATP and the fluorescence intensity was measured with a Varioskan Flash multimode reader (Thermo Fisher Scientific, Waltham, MA), with a 490 nm excitation wavelength and an emission at 530 nm.

For YO-PRO-1 uptake assay, the cells were harvested, centrifuged at 230*g* for 5 min and resuspended in sucrose buffer (20 mM HEPES, 300 mM sucrose, 5 mM KCl, 1 mM $MgCl_2$, 1 mM $CaCl_2$, 10 mM glucose, and pH 7.4) in the presence of YO-PRO-1 (1 μM) and placed in a 96 well plate. The cells were treated with BzATP and the fluorescence intensity was measured with a Varioskan Flash multimode reader (Thermo Fisher Scientific), with a 470 nm excitation wavelength and an emission at 509 nm.

2.4 | Flow cytometry analysis

2.4.1 | Multiple staining with Fluo-3 AM, TO-PRO-3, and PI

Intracellular calcium concentration and large pore opening were assessed by flow cytometry analysis using, respectively, Fluo-3-AM fluorescent dye and the membrane impermeant DNA-intercalating dye TO-PRO-3 (Life Technologies). Briefly, the cells (10^6 cells/ml) were loaded with Fluo-3 AM (50 nM) for 30 min in culture medium without foetal calf serum at 37°C. The cells were then centrifuged at 230*g* for 5 min and resuspended in sucrose buffer (20 mM HEPES, 300 mM sucrose, 5 mM KCl, 1 mM $MgCl_2$, 1 mM $CaCl_2$, 10 mM glucose, and pH 7.4) containing TO-PRO-3 (10 nM) and PI (75 nM). The cells (10^5 in 200 μl) were treated with BzATP and/or different compounds for 1 h at room temperature and analysed using flow cytometry. In some experiments, the impermeant DNA-intercalating dye YO-PRO-1 was used at 10 nM instead of TO-PRO-3 (without Fluo-3 AM). We used a lower concentration of Fluo-3 AM in flow cytometry (50 nM) than in the microplate reader analysis (500 nM) because the former method is more sensitive. The concentration of 50 nM was sufficient and reduced the percentage compensation in the FL3 filter used to detect PI.

The staining index was defined as the difference between the positive staining and the (negative) background signal, divided by twice the standard deviation of the background signal. To estimate the staining indexes of the dyes without interfering with their ability to enter through P2RX7, unlabelled dead cells were taken as negative controls and labeled dead cells were taken as positive controls.

Staining index = $(MFI_{Positive\ cells} - MFI_{Negative\ cells})/(2 \times \text{standard deviation } MFI_{Negative\ cells})$ as previously described [30].

2.4.2 | Conventional flow cytometry

Conventional cytometry was performed with a CyAn ADP LX9 flow cytometer running Summit analytical software (Beckman Coulter, Miami, FL). Fluo-3 AM and PI were excited by the blue laser (488 nm) and the emission fluorescences were acquired with FL1 (530/40 nm) and FL3 (613/20 nm) filters, respectively. TO-PRO-3 was excited by the red laser (633 nm) and TO-PRO-3 emission fluorescence was acquired with an FL8 (665/20 nm) filter. Highly PI-positive cells were considered as dead cells and gated out using Summit analysis software.

2.4.3 | Imaging flow cytometry

Imaging flow cytometry was performed on Imagestream^X MarkII imaging flow cytometer (AMNIS, Millipore, Seattle, WA). Twenty thousand cells were collected for each sample in INSPIRE acquisition software. Laser powers were adjusted as follows in order that the fluorophore intensities are in the detection range: 375 nm: 70 mW; 488 nm: 129 mW; 561 nm: 100 mW; 642 nm: 50 mW; 785 nm: 1.75 mW. Fluorescent signals were collected as follows. Brightfield images were measured in channels 1 (430–470 nm) and 9 (575–595 nm). Fluo-3 AM was excited with the 488 nm laser (129 mW) and fluorescence was measured in channel 2 (470–560 nm). PI was excited with the 561 nm laser (100 mW) and fluorescence was measured in channel 4 (595–660 nm). TO-PRO-3 was excited with the 642 nm laser (50 mW) and fluorescence was measured in channel 11 (660–720 nm). Hoechst 33342 was excited with the 375 nm laser (70 mW) and fluorescence was measured in channel 7 (430–505 nm). Side scatter was probed at 785 nm, and fluorescence was measured in channel 12 (720–800 nm). IDEAS analysis software was used for analysis. Highly PI-positive cells were considered as dead cells and gated out.

2.4.4 | Spectral cytometry

Spectral flow cytometry was performed with an SP6800 spectral cell analyser using SP6800 software (Sony Biotechnology, San Jose, CA). The SP6800 is equipped with 488, 405 and 638 nm lasers. It uses 10 consecutive prisms to spread the emitted fluorescence from individual cells and 32-channel photomultiplier tubes to measure the fluorescence spectrum from 420 nm to 800 nm. Full spectra of unstained cells (autofluorescence) or single-positive cells were analysed with 488, 405, and 638 nm laser excitations and used as references for the spectral unmixing algorithm based on the weighted least squares method (WLSM) [31,32]. The spectrum of the unstained cells was used as the universal negative reference. Based on each dye reference spectrum, the unmixing algorithm was used to calculate the fluorescence intensity of each dye in multistained samples. Ten thousand cells were analysed in each sample. Highly PI-positive cells were considered to be dead cells and were gated out using SP6800 analysis software.

2.4.5 | P2RX7 expression analysis

For P2RX7 expression, HEK-293 cells (10^6 cells/ ml) were saturated in PBS, 3% BSA at room temperature and stained with anti-human P2RX7 monoclonal antibody (cell supernatant) [33] and Alexa Fluor 488-conjugated anti-mouse IgG secondary antibody at room temperature for 30 min. The cells were then centrifuged at 230*g* for 5 min and resuspended in sucrose buffer (20 mM HEPES, 300 mM sucrose, 5 mM KCl, 1 mM $MgCl_2$, 1 mM $CaCl_2$, 10 mM glucose, pH 7.4) containing TO-PRO-3 (10 nM) and PI (75 nM). The cells (10^5 in 200 μl) were treated with BzATP for 1 h at room temperature and analysed using flow cytometry.

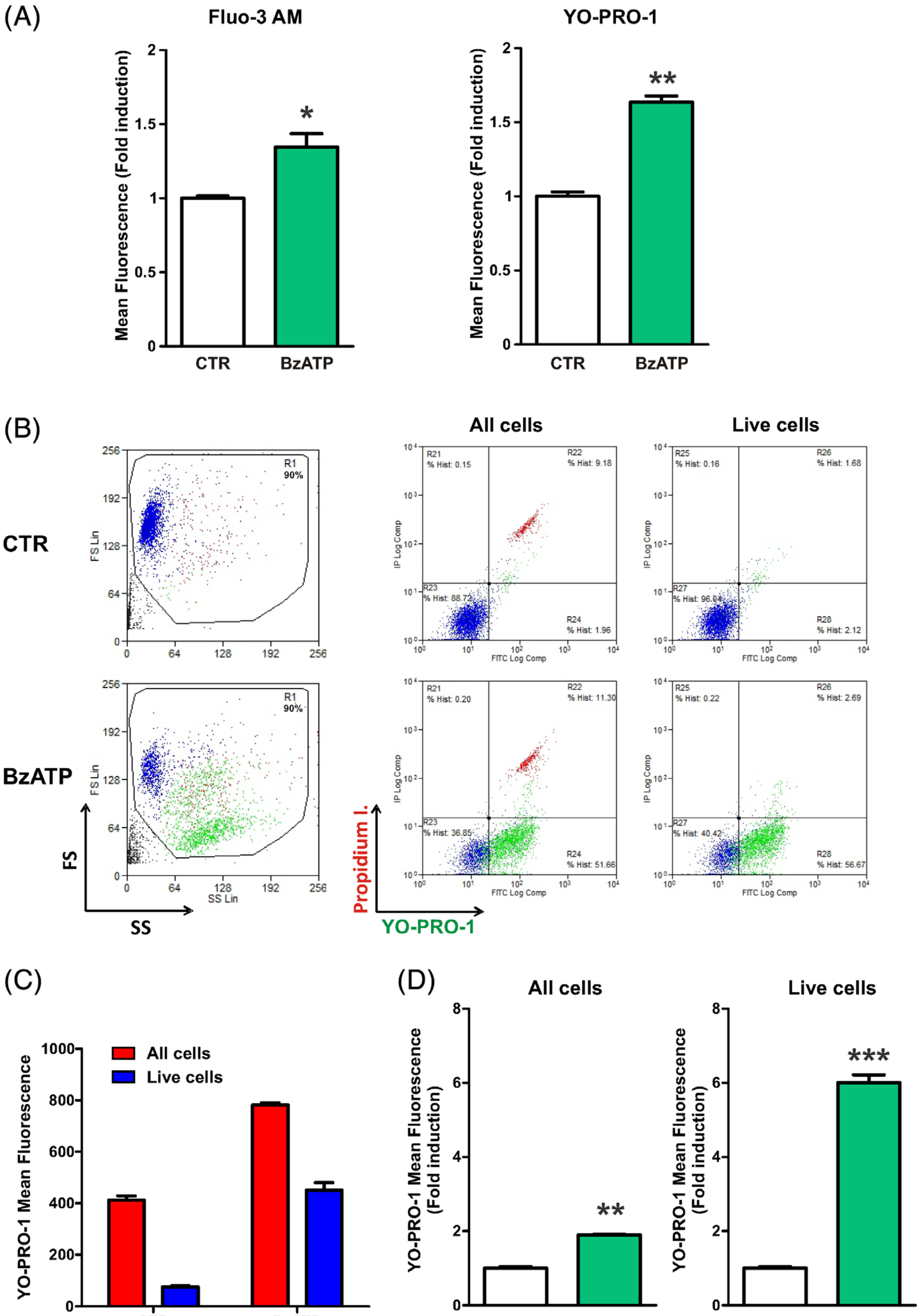

FIGURE 1 Determination of P2RX7 activity by the use of fluorescent dyes in a microplate assay or a flow cytometry assay. (A) HEK-293 cells overexpressing human P2RX7 were stained with the calcium indicator Fluo-3 AM (left panel) or incubated in the presence of the nonpermeant DNA-intercalating dye YO-PRO-1 (right panel) before addition of the P2RX7 agonist BzATP (100 μM) for 10 min (Fluo-3 AM, left panel) or 1 h (YO-PRO-1, right panel). Fluorescence was measured with the microplate reader VarioSkan and plotted as a fold induction relative to control cells. The results are representative of three independent experiments (**p* < 0.05; ***p* < 0.01). (B) HEK-293 cells overexpressing human P2RX7 were incubated with the non-permeant DNA-intercalating dyes YO-PRO-1 (large pore opening) and PI (cell viability) before addition of the P2RX7 agonist BzATP (100 μM) for 1 h. The cells were then analysed using flow cytometry (with the CyAn cytometer from Beckman Coulter). Two-parameter plots of size versus structure parameters (FS/SS) and YO-PRO-1 versus PI fluorescence of nontreated cells (CTR) or cells treated with BzATP (100 μM) were created with Summit software. High PI (dead) cells were coloured in red and PI-negative (live) cells were colored in blue with Summit software. The cells presenting a size decrease in the presence of BzATP were arbitrary colored in green with Summit software. (C) Histograms represent YO-PRO-1 mean fluorescence in all cells or in live (PI-negative) cells in the presence or absence of BzATP from Figure 1 (B). (D) The YO-PRO-1 fluorescence was plotted as a fold induction relative to control cells in all cells and in live cells. The results are representative of three independent experiments (***p* < 0.01; ****p* < 0.001)

2.5 | Three-dimensional molecular models

Marvin software (version 17.29.0, http://www.chemaxon.com) was used for 3D conversion and conformer generation. Scatter plots were produced with DataWarrior (version 4.5) [34], and 3D representations were displayed using UCSF Chimera [35].

2.6 | Statistical analysis

The results are expressed as the mean ± SEM of three separate replicate experiments. Levels of significance were evaluated using Student's *t*-test. The threshold for statistical significance was set to $p < 0.05$. All analyses were performed with GraphPad Prism 5 software (GraphPad Software, San Diego, CA).

3 | RESULTS

3.1 | Assessment of P2RX7's large pore activity in a flow cytometry assay

In order to measure the biological activity of molecules synthesized as potential P2RX7 modulators, we developed an assay in HEK-293 cells stably expressing human P2RX7. First, we used a microplate reader to assay the intracellular calcium concentration (using the calcium indicator Fluo-3 AM) and large pore opening (using YO-PRO-1). The cells were stimulated with the potent agonist BzATP in a sucrose buffer—a commonly used buffer for pharmacological studies of P2RX7 [25,36,37]. As expected, we observed increases in intracellular calcium content (Figure 1(A), left panel) and YO-PRO-1 uptake (Figure 1(A), right panel). Despite the statistical significance of the observed differences (*$p < 0.05$, **$p < 0.01$ in the figure), we further developed a flow cytometry assay in an attempt to increase the sensitivity of YO-PRO-1 dye measurement (Figure 1(B)). Two-parameter plots of forward scatter (FS) versus side scatter (SS) highlighted a single-cell population in control samples, and the appearance of a new cell population (characterized by cell shrinkage and increased granularity) in the presence of BzATP (the cells arbitrary colored in green). We then performed a YO-PRO-1 uptake assay in the presence of a low concentration (75 nM) of the cell viability marker propidium iodide. In control experiments (i.e., in the absence of a P2RX7 agonist), YO-PRO-1 versus PI two-parameter plots evidenced a cell population that incorporated large amounts of YO-PRO-1. PI staining indicated that these cells were dead; hence, YO-PRO-1-high cells not exposed to a P2RX7 agonist are necrotic cells with a disrupted plasma membrane (high YO-PRO-1/high PI; the red cells on the graph). In live (i.e., PI-negative) cells, the addition of BzATP induced cell shrinkage (the green cells in the FS/SS plot) and YO-PRO-1 uptake (attesting to large pore opening). It was therefore possible to discriminate between dead cells (the high YO-PRO-1/high PI red cells on the graph) and P2RX7-activated cells (the YO-PRO-1-positive/PI-negative, green cells on the graph) by using YO-PRO-1 and a low PI concentration. It is noteworthy that under our experimental conditions, a 1 h incubation with BzATP did not induce significant cell death. We next took advantage of flow cytometry's ability to gate out dead (PI-positive) cells that were strongly stained by YO-PRO-1 (i.e., independently of P2RX7 activation). By gating out dead cells, we removed the high background level of YO-PRO-1 staining (Figure 1(C)), enhanced the specificity of the signal upon BzATP treatment (Figure 1(D)), and increased both the sensitivity (a sixfold increase, relative to the control), statistical significance (***$p < 0.001$), and reproducibility of the method for studying large pore opening versus a microplate assay (Figure 1(A), right panel).

3.2 | A flow cytometry assessment of P2RX7-mediated fluorescent dye uptake

In order to determine the most suitable dye for a flow cytometry assay, we compared the uptake of various fluorescent dyes after the addition of BzATP (Figure 2). HEK-293 cells overexpressing human P2RX7 were incubated in the presence of increasing concentrations of YO-PRO-1 (629 Da; 375 Da as a cation), PI (668 Da; 414 Da as a cation), and 7-aminoactinomycin D (7-AAD; 1270 Da, uncharged), together with BzATP (Figure 2(A) + Supporting Information Figure S1 for the histograms). We also assessed the uptake of the red fluorescent dye TO-PRO-3—a monomeric cyanine nucleic acid stain that is structurally similar to YO-PRO-1 and has much the same molecular weight (671 and 629 Da for TO-PRO-3 and YO-PRO-1, respectively; 417 Da as a cation for TO-PRO-3). As previously shown in Figure 1(B), YO-PRO-1 and TO-PRO-3 uptakes were measured in the presence of low concentrations of PI (75 nM). High YO-PRO-1/high TO-PRO-3/PI-positive cells (corresponding to dead cells) were gated out. In order to study BzATP-induced uptake of increasing concentrations of PI (1 nM to 1 μM) by live cells, we checked whether PI staining was associated with an increase in Fluo-3 AM staining (Supporting Information Figure S2). The high-molecular-weight dye 7-AAD was used as a negative control, since it does not enter cells through P2RX7. BzATP-induced TO-PRO-3 staining was observed in the presence of 1 nM TO-PRO-3, whereas YO-PRO-1 uptake was visible in the presence of concentrations above 10 nM (Figure 2(A) + Supporting Information Figure S1 for histograms). Propidium uptake was weak at 100 nM. Nevertheless, BzATP-induced PI staining in live cells was detected at concentrations above 1 μM, whereas 10 nM was sufficient to stain dead cells (Supporting Information Figure S2). We therefore chose to use a low concentration of PI, in order to selectively identify dead cells with little (if any) P2RX7-dependent uptake under our experimental conditions. TO-PRO-3 was therefore the most sensitive fluorescent dye for assessing large pore opening.

We also estimated each compound brightness by calculating the corresponding staining index [30]. Using this method, TO-PRO-3 appeared to be brighter than YO-PRO-1 in the low concentration range—explaining TO-PRO-3 higher sensitivity (Figure 2(B)). Above 100 nM, high PI brightness was effective for staining dead cells and the P2RX7-mediated uptake was weak. Given that the YO-PRO-1,

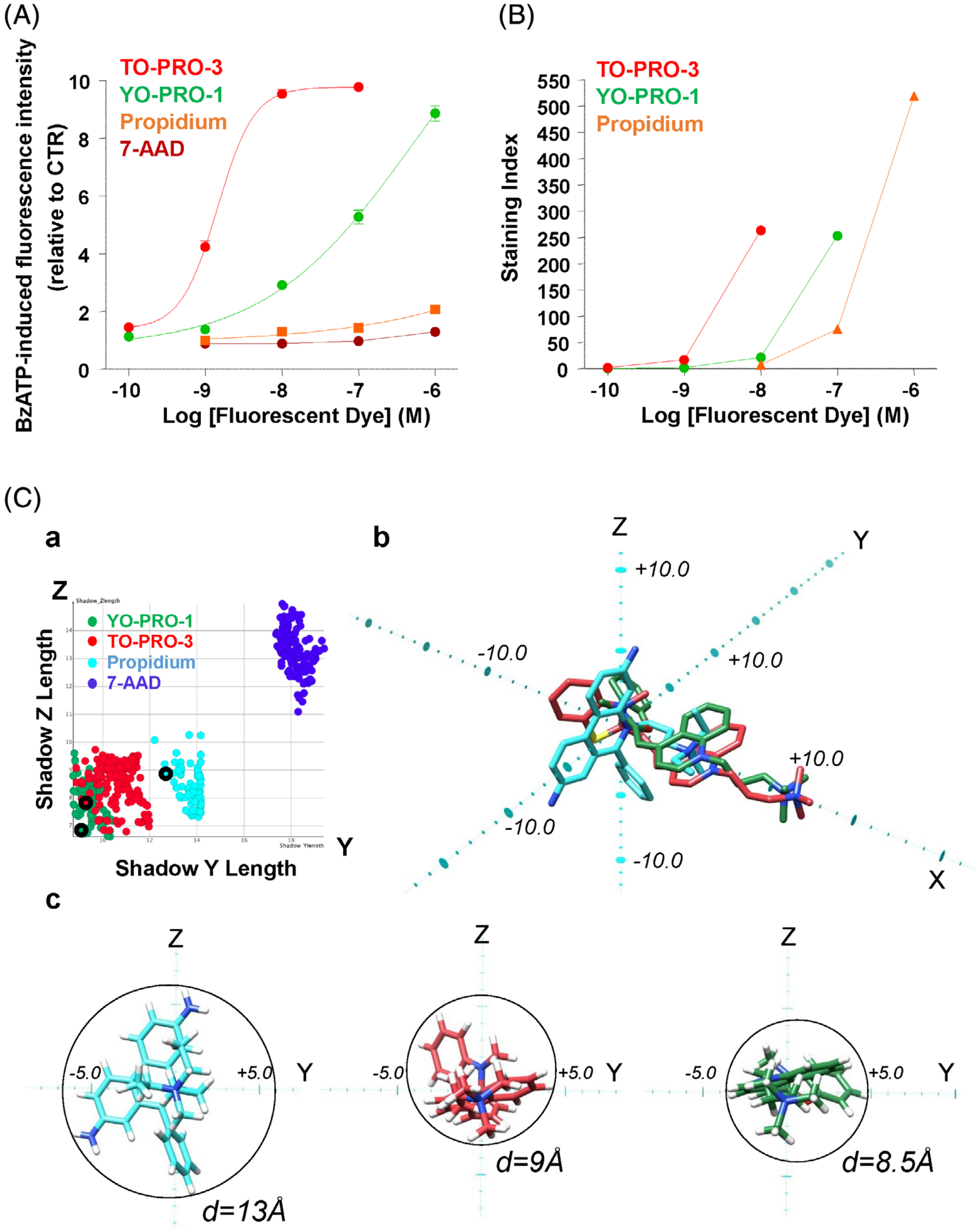

FIGURE 2 A flow cytometry assessment of P2RX7-mediated fluorescent dye uptake. (A) HEK-293 cells overexpressing human P2RX7 were incubated in the presence of increasing concentrations of the nonpermeant DNA-intercalating dyes YO-PRO-1, TO-PRO-3, propidium iodide and 7-AAD in the presence of the P2RX7 agonist BzATP (100 μM) for 1 h. The cells were then analysed using flow cytometry (with the CyAn cytometer). Dye fluorescence was plotted as a fold induction relative to control cells. (B) Line graph representing the staining index of the indicated dyes at different concentrations. Dead cells were taken as high-positive cells. The results are representative of three independent experiments. (C) Structural insights for pore permeation through human P2RX7. (a) According to the best-discriminating Y/Z area for each P2RX7 probe (see other X/Y and X/Z planes in supplemental information), relevant conformers can be viewed in three (b) and in two (the Y/Z plane) (c) dimensions in order to extrapolate the minimal diameter *d* for permeation through P2RX7

TO-PRO-3 and propidium dications have similar molecular weights, one would expect them all to permeate through P2RX7 large pore in a similar way. We hypothesized that the enhanced uptakes of YO-PRO-1 and TO-PRO-3 were linked to their linear three-dimensional structure; in contrast, propidium broader three-dimensional structure might disfavor permeation through the pore (Supporting Information Figure S3). We therefore compared the shadow projections of all the possible structural conformations of 7-AAD, YO-PRO-1, TO-PRO-3 and propidium with our experimental results. This analysis confirmed that 7-AAD conformers have much greater dimensions than the other molecules, which prevents this dye from passing through the pore. YO-PRO-1 and TO-PRO-3 conformers can be easily distinguished from propidium conformers in two intersecting planes (X/Y and Y/Z). Despite its equivalent molecular weight, propidium has at least one dimension greater than 13 Å in each intersecting plane. In contrast, YO-PRO-1 and TO-PRO-3 conformers have at least one dimension of between 7 and 9 Å in two intersecting planes; this might favor their permeation through P2RX7. According to the best-discriminating Y/Z area for each P2RX7 probe (Figure 2(C,a)), relevant conformers can be viewed in three dimensions (Figure 2(C,b)) and in two dimensions (the Y/Z plane, Figure 2(Cc)); this extrapolates the minimum diameter *d* for permeation through P2RX7. YO-PRO-1 (*d* = 8.5 Å) and TO-PRO-3 (*d* = 9 Å) are more elongated than propidium (*d* = 13 Å); this might facilitate the permeation of YO-PRO-1 and TO-PRO-3 through the receptor and thus explain the staining observed in the presence of BzATP. With regard to P2RX7-mediated uptake, the fluorescent dyes' molecular structures and dimensions therefore appear to be more important than their molecular weights.

3.3 | The kinetics of P2RX7 cation channel and large pore activities

In view of TO-PRO-3 high sensitivity and the overlapping emission wavelengths for the calcium indicator Fluo-3 AM and the commonly used YO-PRO-1 dye (526 and 509 nm, respectively), we chose to combine the red DNA-binding dye TO-PRO-3 (emission wavelength: 661 nm) with the green Fluo-3 AM dye in order to simultaneously assess P2RX7 calcium channel and large pore activities (Figure 3(A)). Simultaneous PI staining was also used to gate out dead cells. This kinetic study revealed that the BzATP-induced, rapid Ca^{2+} influx (observed after 1 min) in all cells was followed by the progressive appearance of two distinct cell populations over the next hour. In one cell population, the Ca^{2+} level returned to baseline. The second cell population slowly incorporated TO-PRO-3 dye—attesting to the opening of the large pore. After a 1-h incubation with BzATP, cells displaying Fluo-3 AM/TO-PRO-3 double-positive staining were clearly seen; this allowed a stringent evaluation of P2RX7 activation (49% of the cells). Staining with an anti-P2RX7 antibody demonstrated that BzATP-exposed, TO-PRO-3-positive cells expressed higher membrane levels of P2RX7 (Figure 3(B))—clearly linking receptor expression to large pore opening. Cell shrinkage and an increase in granularity appeared between 5 and 10 min after BzATP addition (Supporting Information Figure S4(A)). The cell shrinkage observed in the presence of BzATP in sucrose buffer might be linked to P2RX7-mediated K^+ depletion [38], since it was prevented by reduction of the potassium electrochemical gradient (i.e., the use of sucrose buffer supplemented with 140 mM KCl) and induced by addition of the potassium ionophore nigericin (Supporting Information Figure S5). As mentioned above, cell viability did not change significantly during this 1 h period (Supporting Information Figure S4(B)). P2RX7's functional activities and the associated changes in cell morphology were confirmed by imaging flow cytometry (Supporting Information Figure S6). Treatment with BzATP was associated with the appearance of the Fluo-3 AM/TO-PRO-3 double-positive cell population and elevated granularity (dark field, side scatter [SS]). Bright-field images evidenced a lower cell size, blebbing, and greater granularity in the presence of BzATP, relative to control cells.

We used Fluo-3 AM/TO-PRO-3/PI triple staining to measure BzATP potency (i.e., the EC_{50}) on both human and mouse P2RX7 (Figure 3(C)). The mean ± SEM EC_{50} of BzATP in sucrose buffer was 31 ± 3 μM for human P2RX7 and 16 ± 2 μM for mouse P2RX7; these values are in line with the literature data [39]. Quantification of double-positive cells (with high Ca^{2+} influx and large pore opening) proved to be an excellent method for assaying a drug candidate's biological effects on P2XR7 variants that form large pores [15]. The method takes account of cell viability and is therefore suitable for measuring early and late P2RX7-mediated events in the same tube.

3.4 | Screening of potential P2RX7 antagonists

We used Fluo-3 AM/TO-PRO-3/PI triple staining to screen our newly synthesized compounds, two of which are referred to hereafter as compound A and compound B (Figure 4). BzATP-induced Fluo-3 AM/TO-PRO-3 double staining was inhibited by the reference antagonist AZ11645373 [40] and several new compounds, including compound A (Figure 4(A)). These compounds inhibited BzATP-induced morphological changes and did not induce cell death (Supporting Information Figure S7). Our results indicate that this method is very sensitive and allows the accurate measurement of the half maximal inhibitory concentration (IC_{50}) of P2RX7 antagonists (Figure 4(B), IC_{50} = 459 nM for compound A). The addition of compound B alone induced an increase in Fluo-3 AM fluorescence—suggesting that it is a calcium channel agonist (Figure 4(A)). After the further addition of BzATP, the cells did not incorporate TO-PRO-3 dye but were still positive for Fluo-3 AM. At first sight, therefore, compound B inhibited the large pore activity and stimulated calcium influx. However, comparison of compound-B-treated cells with non-treated cells in the absence of Fluo-3 AM and TO-PRO-3 indicated that compound B had intense intrinsic fluorescence (Figure 4(C)). This was detected in the FL1 channel (530 ± 30 nm) used to quantify Fluo-3 AM. Thus, compound B's green fluorescence interfered with calcium content measurement and prevented us from drawing any conclusions about its effect on P2RX7 calcium channel activity.

3.5 | A multiparameter spectral flow cytometry analysis of P2RX7 activity

In order to take account of compound B intrinsic fluorescence (Figure 4(A,C)), we performed experiments with a spectral flow cytometer (SP6800, Sony Biotechnology). In contrast to conventional flow cytometers (which detect the fluorochrome emission peak with dichroic mirrors and band-pass filters), spectral flow cytometry enables the whole emission fluorescence spectrum to be analysed

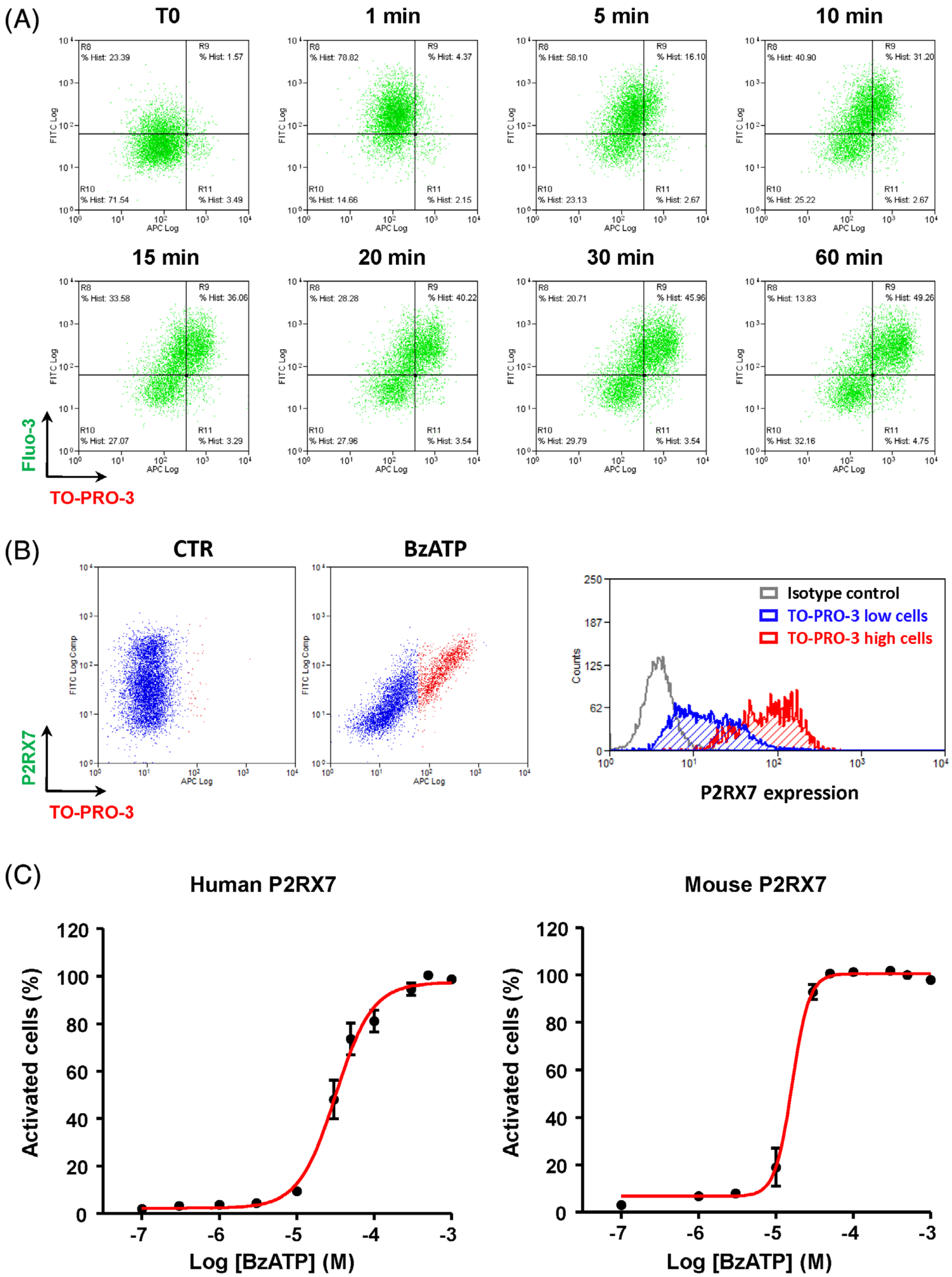

FIGURE 3 The kinetics of P2RX7 cation channel and large pore activities. (A) HEK-293 cells overexpressing human P2RX7 were stained with the calcium indicator Fluo-3 AM and then incubated with the nonpermeant DNA-intercalating dyes TO-PRO-3 (large pore opening) and propidium iodide (cell viability) before addition of the P2RX7 agonist BzATP (100 μM). The cells were then analysed at different time points using flow cytometry (with the CyAn cytometer). Two-parameter plots of Fluo-3 AM versus TO-PRO-3 fluorescence were created with Summit software. (B) HEK-293 cells overexpressing human P2RX7 were stained with anti-P2RX7 antibodies and incubated with TO-PRO-3 in the absence (CTR) or presence of BzATP (100 μM) for 1 h. The cells were then analysed using flow cytometry (with the CyAn cytometer). Two-parameter plots of P2RX7 expression versus TO-PRO-3 fluorescence (left panel) were created with Summit software. Overlays of P2RX7 staining in TO-PRO-3 low (blue) and TO-PRO-3 high (red) cells in the presence of BzATP are represented in the right panel. The results are representative of three independent experiments. (C) HEK-293 cells overexpressing human P2RX7 (left panel) and mouse P2RX7 (right panel) were stained with Fluo-3 AM and then incubated with TO-PRO-3 before addition of increasing concentrations of BzATP. The percentages of Fluo-3 AM/TO-PRO-3 double-positive cells are plotted for half maximal effective concentration (EC_{50}) calculation. The results are representative of three independent experiments

without the need for conventional compensation matrices [31]. Whereas a conventional cytometer's band-pass filters cannot distinguish between two spectrally adjacent fluorochromes, a spectral cytometer can perform a multicolor analysis with an unmixing algorithm [31,32]. Each spectrum derived from single-stained cells and the spectrum from unstained cells (autofluorescence) are considered as reference spectra for a spectral unmixing algorithm based on WLSM. Dye fluorescences from multistained samples are unmixed by the algorithm (using the spectra of unstained cells and single-stained cells as references), in order to mathematically separate and measure each fluorochrome's emission fluorescence intensity. We first determined the shape of the respective emission spectra of unstained HEK cells (autofluorescence), each individual dye, and compound B (Figure 5(A)) as references for the unmixing algorithm. The results of our spectral cytometry experiments confirmed that compound B fluorescence overlapped with Fluo-3 AM fluorescence at around 530 nm, after excitation with the 488 nm laser. However, compound B also displayed an intense fluorescence peak between 450 and 470 nm after excitation at 405 nm.

The spectra of multistained cells (Fluo-3 AM, PI and TO-PRO-3) were determined in the presence and absence of BzATP (Figure 5 (B)). BzATP induced the appearance of a Fluo-3-high cell population (indicated by the green arrow in the figure) and a TO-PRO-3 high cell population (indicated by the red arrow). After fluorescence unmixing, BzATP was found to induce the appearance of a population of small cells (arbitrarily marked in green in the figure; Supporting Information Figure S8 for FS/SS plots) that was positive for Fluo-3 AM and TO-PRO-3 (i.e., with large pore opening) (Figure 5(C)). We then assessed compound B effect on P2RX7 activity. First, we applied the unmixing algorithm for the Fluo-3 AM, TO-PRO-3 and PI fluorescence signals without considering compound B spectrum, as a comparison with conventional cytometry (Figure 5

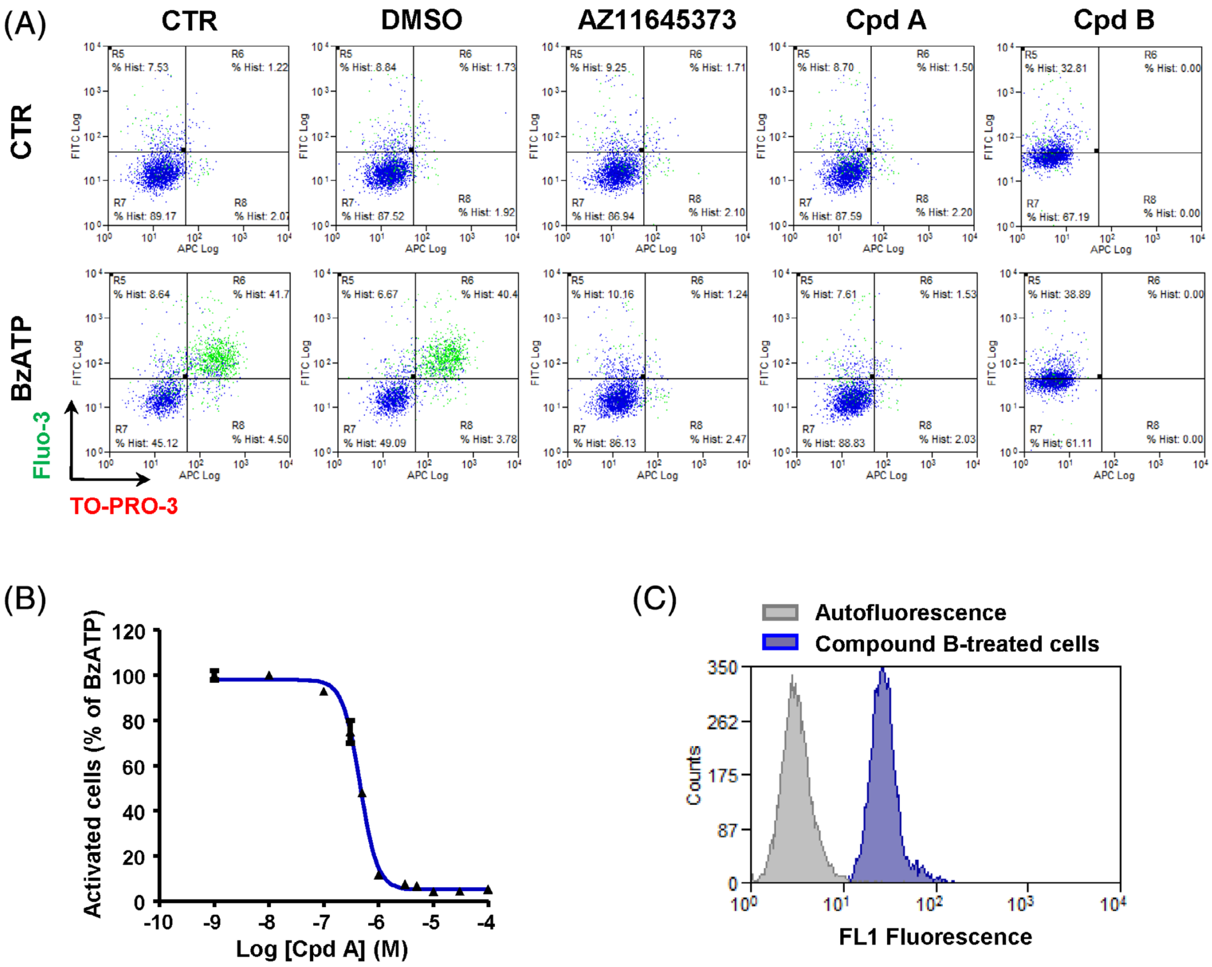

FIGURE 4 Screening of potential P2RX7 antagonists. (A) HEK-293 cells overexpressing human P2RX7 were stained with the calcium indicator Fluo-3 AM and then incubated with the non-permeant DNA-intercalating dyes TO-PRO-3 and propidium iodide in the presence of indicated molecules at 10^{-5} M for 15 min before addition of the P2RX7 agonist BzATP (100 μM) for 1 h. The cells were then analysed using flow cytometry (with the CyAn cytometer). Two-parameter plots of Fluo-3 AM versus TO-PRO-3 fluorescence were created with Summit software. (B) Percentages of Fluo-3 AM/TO-PRO-3 double-positive cells are plotted for calculation of half maximal inhibitory concentration (IC_{50}) of compound A in HEK-293 cells overexpressing human P2RX7. The results are representative of three independent experiments. (C) HEK-293 cells overexpressing human P2RX7 were incubated in the presence of compound B at 10^{-5} M for 1 h. The overlay of fluorescence intensity in FL1 band-pass filter (530 nm ± 30) of unstained cells versus compound-B-treated cells was created with Summit software

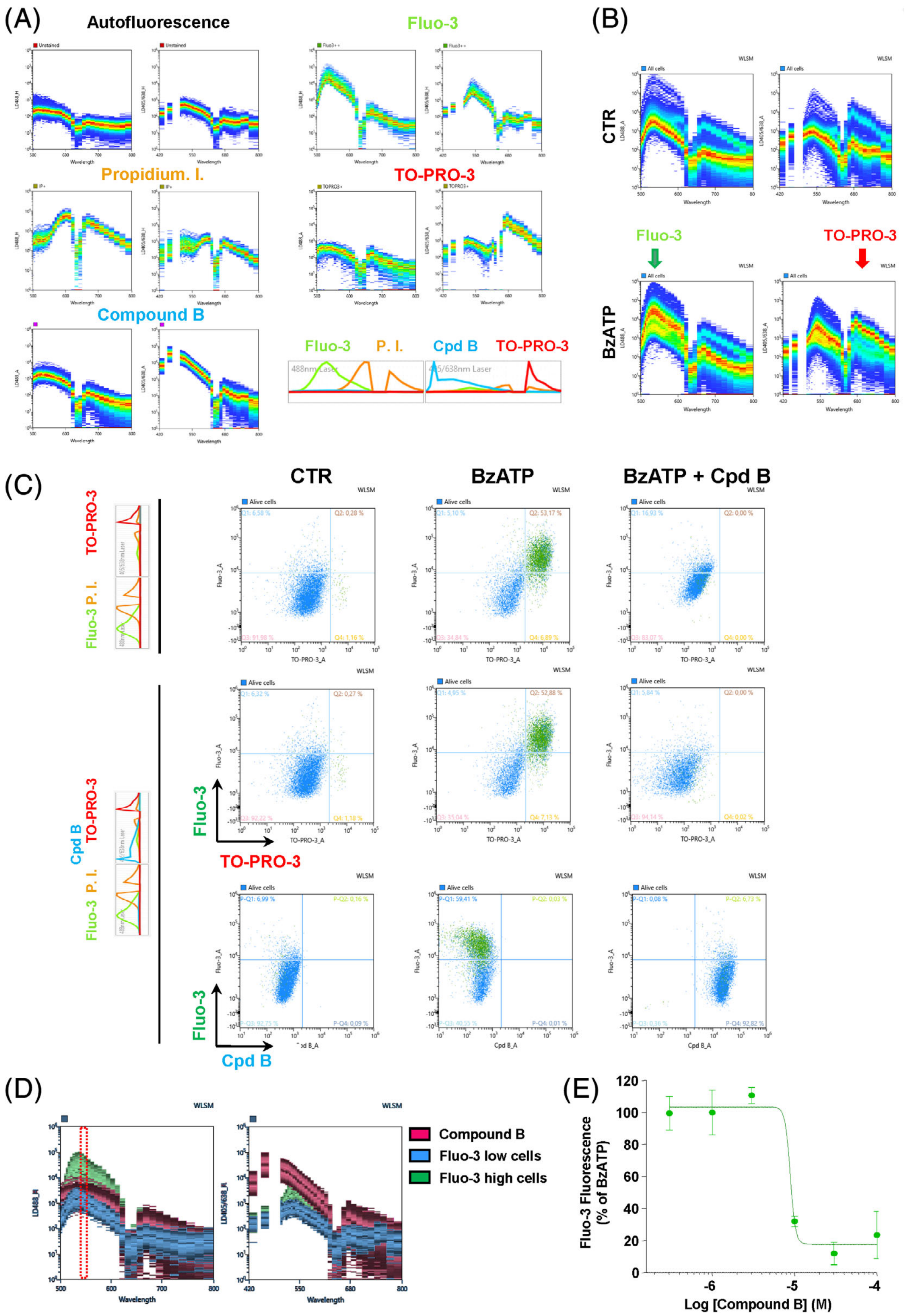

FIGURE 5 Legend on next page.

(C), upper panel). Compared with control cells, Fluo-3 AM fluorescence was elevated in the presence of compound B; this was due to spectral overlap between Fluo-3 AM and compound B (Figure 5(D)), as seen in the conventional cytometry experiments (Figure 4(A,C)). However, the addition of compound B's spectrum to the unmixing algorithm enabled us to dissociate Fluo-3 and compound B fluorescence emissions and therefore specifically detect both Fluo-3 AM and compound B (Figure 5(C), lower panels). Unmixing of compound

B's fluorescence highlighted a dose-dependent decrease in Fluo-3 AM intensity – indicating inhibition of the calcium influx by compound B (Figure 5(C,E)). Hence, in contrast to conventional flow cytometry, spectral flow cytometry takes account of a drug compound intrinsic fluorescence and enables the accurate measurement of fluorescent dyes with overlapping emission peaks. We therefore provided evidence to suggest that compound B antagonizes P2RX7 calcium channel activity (measured with Fluo-3 AM) and large pore activity (measured with TO-PRO-3).

4 | DISCUSSION

Fluorescence-based bioassays are now widely employed in the drug discovery process. The microplate assay has long been the preferred method, since it is suitable for high-throughput screening. However, microplate assay have several limitations, such as erroneous, sustained increases in fluorescence, low sensitivity (relative to fluorescence microscopy), and the lack of single-cell resolution [41]. The intrinsic fluorescence of compounds can also interfere with fluorescence-based bioassays.

Although a microplate assay can easily detect calcium influx and YO-PRO-1 uptake in HEK cells overexpressing P2RX7, flow cytometry assays are more sensitive and have greater statistical significance for the determination of large pore activity. In the present study, single-cell resolution was the prime benefit of our flow cytometry assay. Indeed, the combination of a low concentration of PI with DNA-intercalating dyes (YO-PRO-1 and TO-PRO-3) enabled us to gate out cells with a disrupted plasma membrane and thus reduce background fluorescence from accumulated DNA-intercalating dyes. This accuracy was associated with dramatically higher reproducibility, sensitivity and statistical significance. This was made possible by the absence of BzATP-induced cell death under our experimental conditions.

Although it is generally agreed that P2RX7 has a molecular weight cut-off of 900 Da, propidium (414 Da as a cation) can be used as a cell viability marker because it does not significantly permeate through the open P2RX7 pore [4,9,10]. In fact, P2RX7-mediated propidium uptake was very low at concentrations below 1 μM, in accordance with previous observations revealing human and murine lymphocytes allows ethidium but not propidium uptake [42,43]. Although PI has been already used as a fluorescent dye to study P2RX7 large pore activity, the reported experiments featured micromolar concentrations of propidium and high concentrations of BzATP [44]. Nevertheless, propidium brightness at lower concentrations made this dye a highly efficient stain for dead cells in our assay.

Our results demonstrated that the best permeant fluorescent dyes were TO-PRO-3 and YO-PRO-1. TO-PRO-3 was associated with more sensitivity—primarily because it is brighter (i.e., has a higher staining index) than YO-PRO-1. The permeation of large organic cations (such as *N*-methyl-D-glucamine) through the pore of ATP-gated P2X receptors was recently studied in molecular dynamics simulations. Entry was associated with the molecule's ability to adopt different molecular conformations and orientations, relative to the pore axis [6]. Similarly, TO-PRO-3 and YO-PRO-1 elongated molecular structures appear to facilitate pore entry. With regard to their three dimensional structures, YO-PRO-1 and TO-PRO-3 can adopt conformations with estimated maximum dimensions of 8.5 and 9 Å, respectively; by comparison, P2RX7 pore diameter may be as high as 8.5 Å [45]. Propidium's greater maximum dimension (13 Å) may explain its weak permeation through P2RX7. Hence, the fluorescent dyes' molecular size and shape appear to be more important than their molecular weight with regard to P2RX7-mediated uptake.

We combined the highly sensitive red fluorescent dye TO-PRO-3 with the calcium indicator Fluo-3 AM and the cell viability marker PI, in order to simultaneously assess P2RX7 calcium channel and large pore activities at different time points. The addition of BzATP led to rapid calcium influx (observed after 1 min), followed by a progressive

FIGURE 5 A multiparameter spectral flow cytometry analysis of P2RX7 activity. HEK-293 cells overexpressing human P2RX7 were stained with the calcium indicator Fluo-3 AM, the nonpermeant DNA-intercalating dyes TO-PRO-3 and PI before addition of compound B and/or the P2RX7 agonist BzATP (100 μM) for 1 h. The cells were then analysed by spectral flow cytometry using SP6800 (Sony Biotechnology).
(A) Spectrum charts of unstained HEK-293 cells (autofluorescence) or single stained cells. The left panel is the spectrum chart of cells excited with a 488 nm laser and the right panel is the spectrum chart of cells excited with 405 and 638 nm lasers. Wavelengths from 420 nm to 800 nm are indicated in the x-axis and fluorescence intensities in the y-axis. Normalized intensity spectra of each fluorochrome used in the unmixing algorithm are indicated in the bottom right panel. (B) Spectra of the multistained HEK-293 cells (Fluo-3 AM, PI and TO-PRO-3) were determined in the absence or presence of BzATP. BzATP induced the appearance of a Fluo-3-high cell population (indicated by the green arrow) and a TO-PRO-3 high cell population (indicated by the red arrow). The unmixing algorithm determined in panel A was then applied to determine individual fluorochrome intensities (C). (C) Two-parameter plots of Fluo-3 AM versus TO-PRO-3 fluorescences of nontreated cells (CTR) or cells treated with BzATP (100 μM) with or without compound B at 10^{-5} M were created with the algorithm unmixing Fluo-3 AM, TO-PRO-3 and PI (upper panel). Two-parameter plots of Fluo-3 AM versus TO-PRO-3 and Fluo-3 AM versus compound B fluorescences of nontreated cells (CTR) or cells treated with BzATP (100 μM) with or without compound B at 10^{-5} M were created with the algorithm unmixing Fluo-3 AM, TO-PRO-3, PI and compound B (lower panels). (D) Overlay of spectrum charts of Fluo-3 AM single stained HEK-293 cells incubated in the presence of BzATP (Fluo-3 low and Fluo-3 high cells) and spectrum chart of HEK-293 cells incubated in the presence of compound B. Wavelengths from 420 nm to 800 nm are indicated in the x-axis and fluorescence intensities in the y-axis. The red dashed square represents the FL1 band-pass filter (530 nm ± 30) used in conventional cytometry. (E) Fluo-3 AM fluorescence intensities resulting from the algorithm unmixing Fluo-3 AM, TO-PRO-3, PI and compound B fluorescence, in the presence of increasing concentrations of compound B. The results are representative of three independent experiments

return to the basal level or by sustained uptake over the next hour. These transient versus sustained responses have been already observed in ATP-stimulated PC12 cells by using single-cell fluorescence microscopy; in contrast, a microplate assay only evidenced a sustained calcium increase as the average of the two types of response [41]. We found that sustained calcium influx was associated with progressive TO-PRO-3 uptake. The delay in fluorescent dye uptake (relative to rapid calcium influx) might correspond to the slower permeation of large cations through the pore and the progressive accumulation of these cations within the nucleus. Cells stained by TO-PRO-3 expressed higher membrane levels of P2RX7 than TO-PRO-3 negative cells did. A direct link between dye uptake activity and P2RX7 density has already been demonstrated in macrophages [46,47]. Pore formation may require a threshold number of agonist-occupied receptors or may be linked to P2RX7 clustering through the recruitment of additional P2RX7 subunits [4,9].

Double staining with Fluo-3 AM and TO-PRO-3 is a very efficient method for screening of P2RX7 modulators. It can be performed at different time points, in order to study early and late events. It can be useful for screening compounds before patch-clamp electrophysiology, more appropriate to study rapid events, on the second time scale, at the membrane level. Agonist and antagonist potencies (EC_{50} and IC_{50}) can also be accurately evaluated. Moreover, typical changes in cell morphology—such as cell shrinkage, increased granulosity, and (using imaging flow cytometry) membrane blebbing—are clearly apparent.

The intrinsic fluorescence of new chemical entities complicates the development of fluorescence-based bioassays [48], as evidenced by compound B's biological activity in conventional assays. We took advantage of the recently developed spectral cytometer to efficiently discriminate between fluorochromes with overlapping emission peaks. Spectral cytometry considered the cells' autofluorescence and compound B fluorescence as independent signals, as it does for other fluorescent probes. It was therefore possible to discriminate between Fluo-3 AM staining and compound B fluorescence; in contrast to conventional cytometry, this correction highlighted compound B antagonism of P2RX7 calcium channel activity.

Flow cytometry is an efficient tool for low- to medium-throughput screening of P2RX7 modulators, and spectral cytometry can be used to screen fluorescent compounds. Hence, this method has allowed the screening of several hundred compounds, the discovery of several P2RX7 antagonists (some of which have *in vivo* efficacy in an animal model of inflammatory bowel disease [49,50], and an analysis of the biological activity of cancer-related P2RX7 isoforms [51]. Spectral cytometry is a valuable new analytical tool for the fluorescence-based screening of drug candidates. It can potentially be adapted to all types of bioassay—irrespective of the fluorescence produced by the probes and/or the test compounds—and thus opens up new perspectives in drug discovery.

ACKNOWLEDGMENTS

The authors thank Claire Devos, Manon Devos, Laura Creusot, Audrey Vinchent, Betsy Crapet, Ludivine Lapèze, Jennifer Bultez and Yoan Laforgue for technical assistance during the compound screening process. The authors thank Emilie Floquet from Bio Imaging Center Lille Nord-de-France Flow Cytometry Core Facility for technical assistance. The authors gratefully thank Cédric Ait Mansour and Nicolas Montcuquet from Sony Biotechnology for fruitful discussions. The authors thank chemists from Hautes Etudes d'Ingénieur (HEI) (Germain Homerin, Davy Baudelet, Benoît Rigo, Alina Ghinet and Philippe Gautret) and from Institut de Chimie Pharmaceutique Albert Lespagnol (Lucas Lemaire and Frédérique Klupsch) for the synthesis of new chemical entities, Christophe Furman and Guillaume Ragé (binding core facility of the University of Lille) for complementary binding experiments, and Philippe Chavatte (molecular modelling core facility of the University of Lille). The authors thank David Fraser PhD (Biotech Communication SARL, Ploudalmézeau, France) for copy-editing assistance. The authors thank Institut National du Cancer (INCA), Institut National de la Santé et de la Recherche Médicale (INSERM), Centre National de la Recherche Scientifique (CNRS) and the University of Lille for financial support.

AUTHOR CONTRIBUTIONS

Amélie Barczyk: Data curation; formal analysis; methodology; writing-review and editing. **Hélène Bauderlique-Le Roy:** Data curation; formal analysis; methodology. **Nathalie Jouy:** Data curation; formal analysis; methodology. **Nicolas Renault:** Data curation; formal analysis; software. **Audrey Hottin:** Resources. **Régis Millet:** Funding acquisition; project administration; resources; writing-review and editing. **Valérie Vouret-Craviari:** Conceptualization; funding acquisition; project administration; writing-review and editing. **Sahil Adriouch:** Conceptualization; funding acquisition; project administration; resources; writing-review and editing. **Thierry Idziorek:** Resources; validation; writing-review and editing. **Xavier Dezitter:** Conceptualization; data curation; formal analysis; methodology; supervision; writing-original draft; writing-review and editing.

CONFLICT OF INTEREST

The authors declare no conflict of interest.

ORCID

Xavier Dezitter https://orcid.org/0000-0001-6932-6947

REFERENCES

1. Burnstock G, Knight GE. The potential of P2X7 receptors as a therapeutic target, including inflammation and tumour progression. *Purinergic Signal.* 2018;*14*:1–18.
2. Pelegrin P. Many ways to dilate the P2X7 receptor pore. *Br J Pharmacol.* 2011;*163*:908–11.
3. Alves LA, Melo Reis RA, de Souza CA, de Freitas MS, Teixeira PC, Neto Moreira FD, et al. The P2X7 receptor: shifting from a low- to a high-conductance channel - an enigmatic phenomenon? *Biochimica et Biophysica Acta*. 2014;*1838*:2578–87.
4. Di Virgilio F, Schmalzing G, Markwardt F. The elusive P2X7 macropore. *Trends in Cell Biology*. 2018;*28*:392–404.
5. Pelegrin P, Surprenant A. Pannexin-1 mediates large pore formation and interleukin-1beta release by the ATP-gated P2X7 receptor. *EMBO J*. 2006;*25*:5071–82.

6. Harkat M, Peverini L, Cerdan AH, Dunning K, Beudez J, Martz A, et al. On the permeation of large organic cations through the pore of ATP-gated P2X receptors. *Proc Natl Acad Sci USA*. 2017;*114*:E3786–95.
7. Pippel A, Stolz M, Woltersdorf R, Kless A, Schmalzing G, Markwardt F. Localization of the gate and selectivity filter of the full-length P2X7 receptor. *Proc Natl Acad Sci USA*. 2017;*114*:E2156–65.
8. Li M, Toombes GE, Silberberg SD, Swartz KJ. Physical basis of apparent pore dilation of ATP-activated P2X receptor channels. *Nat Neurosci.* 2015;*18*:1577–83.
9. Di Virgilio F, Giuliani AL, Vultaggio-Poma V, Falzoni S, Sarti AC. Non-nucleotide agonists triggering P2X7 receptor activation and pore formation. *Front Pharmacol*. 2018;*9*:39.
10. Peverini L, Beudez J, Dunning K, Chataigneau T, Grutter T. New insights into permeation of large cations through ATP-gated P2X receptors. *Front Mol Neurosci.* 2018;*11*:265.
11. Pelegrin P, Surprenant A. The P2X(7) receptor-pannexin connection to dye uptake and IL-1beta release. *Purinergic Signal.* 2009;*5*:129–37.
12. Adinolfi E, Giuliani AL, De Marchi E, Pegoraro A, Orioli E, Di Virgilio F. The P2X7 receptor: a main player in inflammation. *Biochemical Pharmacol*. 2018;*151*:234–44.
13. Di Virgilio F, Chiozzi P, Falzoni S, Ferrari D, Sanz JM, Venketaraman V, et al. Cytolytic P2X purinoceptors. *Cell Death Differ*. 1998;*5*:191–9.
14. Di Virgilio F. Purines, purinergic receptors, and cancer. *Cancer Res*. 2012;*72*:5441–7.
15. Benzaquen J, Heeke S, Janho Dit HS, Douguet L, Marquette CH, Hofman P, et al. Alternative splicing of P2RX7 pre-messenger RNA in health and diseases: Myth or reality? *Biomed J*. 2019;*42*: 141–54.
16. Ulrich H, Ratajczak MZ, Schneider G, Adinolfi E, Orioli E, Ferrazoli EG, et al. Purine signaling contributes to neuroblastoma metastasis. *Front Pharmacol*. 2018;*9*:500.
17. Arnaud-Sampaio VF, Rabelo ILA, Ulrich H, Lameu C. The P2X7 receptor in the maintenance of cancer stem cells, chemoresistance and metastasis. *Stem Cell Rev Rep.* 2020;*16*:288–300.
18. Adinolfi E, Raffaghello L, Giuliani AL, Cavazzini L, Capece M, Chiozzi P, et al. Expression of P2X7 receptor increases in vivo tumor growth. *Cancer Res*. 2012;*72*:2957–69.
19. Adinolfi E, Capece M, Franceschini A, Falzoni S, Giuliani AL, Rotondo A, et al. Accelerated tumor progression in mice lacking the ATP receptor P2X7. *Cancer Research*. 2015;*75*:635–44.
20. Ghiringhelli F, Apetoh L, Tesniere A, Aymeric L, Ma Y, Ortiz C, et al. Activation of the NLRP3 inflammasome in dendritic cells induces IL-1beta-dependent adaptive immunity against tumors. *Nat Med.* 2009; *15*:1170–8.
21. Hofman P, Cherfils-Vicini J, Bazin M, Ilie M, Juhel T, Hebuterne X, et al. Genetic and pharmacological inactivation of the purinergic P2RX7 receptor dampens inflammation but increases tumor incidence in a mouse model of colitis-associated cancer. *Cancer Res*. 2015;*75*:835–45.
22. Di Virgilio F. P2RX7: a receptor with a split personality in inflammation and cancer. *Mol Cell Oncol.* 2016;*3*:e1010937.
23. Baudelet D, Lipka E, Millet R, Ghinet A. Involvement of the P2X7 purinergic receptor in inflammation: an update of antagonists series since 2009 and their promising therapeutic potential. *Curr Med Chem*. 2015;*22*:713–29.
24. Koch-Nolte F, Eichhoff A, Pinto-Espinoza C, Schwarz N, Schafer T, Menzel S, et al. Novel biologics targeting the P2X7 ion channel. *Curr Opin Pharmacol.* 2019;*47*:110–8.
25. Jursik C, Sluyter R, Georgiou JG, Fuller SJ, Wiley JS, Gu BJ. A quantitative method for routine measurement of cell surface P2X7 receptor function in leucocyte subsets by two-colour time-resolved flow cytometry. *J Immunol Methods*. 2007;*325*:67–77.
26. Korpi-Steiner NL, Sheerar D, Puffer EB, Urben C, Boyd J, Guadarrama A, et al. Standardized method to minimize variability in a functional P2X(7) flow cytometric assay for a multi-center clinical trial. *Cytom B Clin Cytom.* 2008;*74*:319–29.
27. Adriouch S, Dox C, Welge V, Seman M, Koch-Nolte F, Haag F. Cutting edge: a natural P451L mutation in the cytoplasmic domain impairs the function of the mouse P2X7 receptor. *J Immunol*. 2002; *169*:4108–12.
28. Adriouch S, Scheuplein F, Bähring R, Seman M, Boyer O, Koch-Nolte F, et al. Characterisation of the R276A gain-of-function mutation in the ectodomain of murine P2X7. *Purinergic Signal*. 2009;*5*: 151–61.
29. Adriouch S, Dubberke G, Diessenbacher P, Rassendren F, Seman M, Haag F, et al. Probing the expression and function of the P2X7 purinoceptor with antibodies raised by genetic immunization. *Cell Immunol*. 2005;*236*:72–7.
30. Maecker HT, Frey T, Nomura LE, Trotter J. Selecting fluorochrome conjugates for maximum sensitivity. *Cytom Part A*. 2004;*62*:169–73.
31. Futamura K, Sekino M, Hata A, Ikebuchi R, Nakanishi Y, Egawa G, et al. Novel full-spectral flow cytometry with multiple spectrally-adjacent fluorescent proteins and fluorochromes and visualization of in vivo cellular movement. *Cytom Part A*. 2015;*87*:830–42.
32. Schmutz S, Valente M, Cumano A, Novault S. Spectral cytometry has unique properties allowing multicolor analysis of cell suspensions isolated from solid tissues. *PLoS One*. 2016;*11*:e0159961.
33. Buell G, Chessell IP, Michel AD, Collo G, Salazzo M, Herren S, et al. Blockade of human P2X7 receptor function with a monoclonal antibody. *Blood*. 1998;*92*:3521–8.
34. Sander T, Freyss J, von Korff M, Rufener C. DataWarrior: an open-source program for chemistry aware data visualization and analysis. *J Chem Inf Model*. 2015;*55*:460–73.
35. Pettersen EF, Goddard TD, Huang CC, Couch GS, Greenblatt DM, Meng EC, et al. UCSF chimera--a visualization system for exploratory research and analysis. *J Comput Chem*. 2004;*25*:1605–12.
36. Michel AD, Kaur R, Chessell IP, Humphrey PP. Antagonist effects on human P2X(7) receptor-mediated cellular accumulation of YO-PRO-1. *Br J Pharmacol*. 2000;*130*:513–20.
37. Hibell AD, Thompson KM, Xing M, Humphrey PP, Michel AD. Complexities of measuring antagonist potency at P2X(7) receptor orthologs. *J Pharmacol Exp Ther*. 2001;*296*:947–57.
38. Bortner CD, Hughes FM, Cidlowski JA. A primary role for K+ and Na+ efflux in the activation of apoptosis. *J Biol Chem*. 1997;*272*: 32436–42.
39. Donnelly-Roberts DL, Namovic MT, Han P, Jarvis MF. Mammalian P2X7 receptor pharmacology: comparison of recombinant mouse, rat and human P2X7 receptors. *Br J Pharmacol.* 2009;*157*:1203–14.
40. Stokes L, Jiang LH, Alcaraz L, Bent J, Bowers K, Fagura M, et al. Characterization of a selective and potent antagonist of human P2X (7) receptors, AZ11645373. *Br J Pharmacol*. 2006;*149*:880–7.
41. Heusinkveld HJ, Westerink RH. Caveats and limitations of plate reader-based high-throughput kinetic measurements of intracellular calcium levels. *Toxicol Appl Pharmacol.* 2011;*255*:1–8.
42. Wiley JS, Chen R, Jamieson GP. The ATP4- receptor-Operated Channel (P2Z class) of human lymphocytes allows Ba2+ and ethidium+ uptake: inhibition of fluxes by Suramin. *Archiv Biochem Biophys*. 1993; *305*:54–60.
43. Chused TM, Apasov S, Sitkovsky M, Murine T. Lymphocytes modulate activity of an ATP-activated P2Z-type purinoceptor during differentiation. *J Immunol*. 1996;*157*:1371–80.
44. Sun C, Heid ME, Keyel PA, Salter RD. The second transmembrane domain of P2X7 contributes to dilated pore formation. *PLoS One*. 2013;*8*:e61886.
45. Riedel T, Schmalzing G, Markwardt F. Influence of extracellular monovalent cations on pore and gating properties of P2X7 receptor-operated single-channel currents. *Biophys J*. 2007;*93*:846–58.
46. Gudipaty L, Humphreys BD, Buell G, Dubyak GR. Regulation of P2X (7) nucleotide receptor function in human monocytes by extracellular

ions and receptor density. *Am J Physiol Cell Physiol*. 2001;*280*: C943–53.

47. Humphreys BD, Dubyak GR. Modulation of P2X7 nucleotide receptor expression by pro- and anti-inflammatory stimuli in THP-1 monocytes. *J Leukoc Biol*. 1998;*64*:265–73.
48. Simeonov A, Davis MI. Interference with fluorescence and absorbance. *Assay guidance manual [Internet]*. Bethesda, MD: Eli Lilly & Company and the National Center for Advancing Translational Sciences; 2004.
49. Homerin G, Lipka E, Rigo B, Millet R, Dezitter X, Furman C, et al. Discovery of highly functionalized scaffolds: pyrroloimidazolediones as P2X7 receptor antagonists. *Tetrahedron*. 2017;*73*:5327–36.
50. Homerin G, Jawhara S, Dezitter X, Baudelet D, Dufrénoy P, Rigo B, et al. Pyroglutamide-based P2X7 receptor antagonists targeting inflammatory bowel disease. *J Med Chem*. 2020;*63*: 2074–94.
51. Benzaquen J, Dit Hreich SJ, Heeke S, Juhel T, Lalvee S, Bauwens S, et al. P2RX7B is a new theranostic marker for lung adenocarcinoma patients. *Theranostics*. 2020;*10*:10849–60.

SUPPORTING INFORMATION

Additional supporting information may be found online in the Supporting Information section at the end of this article.

ISAC CYTOMETRY Journal of Quantitative Cell Science PART A

Evaluating the Cytometric Detection and Enumeration of the Wine Bacterium, *Oenococcus oeni*

Louise Bartle,[1,2] James G. Mitchell,[3] James S. Paterson[3]*

[1]Department of Wine and Food Science, The University of Adelaide, Urrbrae, Australia

[2]Department of Microbiology and Infectious Diseases, Université de Sherbrooke, Sherbrooke, Québec, Canada

[3]Flinders University, College of Science and Engineering, Adelaide, Australia

Received 21 January 2020; Revised 28 October 2020; Accepted 29 October 2020

Grant sponsor: University of Adelaide; Grant sponsor: Wine Australia, Grant numberAGW Ph 1510

Additional Supporting Information may be found in the online version of this article.

*Correspondence to: James S. Paterson, Flinders University, College of Science and Engineering, Adelaide, South Australia
Email: james.paterson@flinders.edu.au

DOI: 10.1002/cyto.a.24258

Abstract

Flow cytometry is a high-throughput tool for determining microbial abundance in a range of medical, environmental, and food-related samples. For wine, determining the abundance of *Saccharomyces cerevisiae* is well-defined and reliable. However, for the most common wine bacterium, *Oenococcus oeni*, using flow cytometry to determine cell concentration poses some challenges. *O. oeni* most often occurs in doublets or chains of varying lengths that can be greater than seven cells. This wine bacterium is also small, at 0.2–0.6 μm and may exhibit a range of morphologies including binary fission and aggregated complexes. This work demonstrates a straightforward approach to determining the suitability of flow cytometry for the chain-forming bacteria, *O. oeni*, and considerations when using flow cytometry for the enumeration of small microorganisms (<0.5 μm).

Key terms

wine; bacteria; yeast; enumeration

THE enumeration of bacteria from any environment increases our knowledge of microbial dynamics and develops a deepened understanding of conditions and factors that favor the growth of individual species. Shifts in abundance of bacterial species in dynamic systems have been demonstrated in several biological and ecological environments, including human gut microflora (1,2), groundwater (3–5), oceanic (6,7), and food-related environments (8–11). From these studies, the importance of bacterial diversity is linked to the overall health of those environments. It has become increasingly important to determine the abundance of bacteria, since increased abundance of any one species may negatively impact overall diversity and the surrounding environment (1). Alternatively, in environments that require specific species to thrive, such as in wine fermentation, determining microbial abundance can provide information to winemakers, enabling successful fermentation progression (12).

Flow cytometry is currently used to determine microbial abundances in a range of environmental, medical, and industrial environments (5,13–16). In wine, enumerating yeast and lactic acid bacteria during fermentation is crucial for understanding the dynamics of successful and efficient wine production. The most common wine yeast, *Saccharomyces cerevisiae*, conducts alcoholic fermentation, while the common wine lactic acid bacterium, *Oenococcus oeni*, completes malolactic fermentation. For *O. oeni*, reaching a population density of 1×10^6 cfu ml^{-1} often correlates with successful malolactic fermentation onset (12). However, for *S. cerevisiae*, alcoholic fermentation onset occurs when oxygen has been depleted, but growth must be sustained to complete the process (17). Enumerating *S. cerevisiae* during fermentation is currently most accurately and rapidly done by flow cytometry (18), as they are easy to distinguish from background noise due to their size, intracellular

ISAC INTERNATIONAL SOCIETY FOR ADVANCEMENT OF CYTOMETRY

complexity, and ease of staining. However, *O. oeni* has been difficult to distinguish from particulate noise in red wines (18,19) as they are smaller and less complex.

Flow cytometry is preferred over microscopy and cell culture methods due to its speed, reliability, ease of use, and versatility (15,20). Microscopy can be time consuming and is heavily limited by the subjective counting process (21). Furthermore, cell culture methods for enumeration rely on a single cell to form a colony on an agar plate, therefore relying on the cells being viable, culturable and to be in singular form (22). As flow cytometry becomes increasingly available for researchers studying bacteria, it is imperative that methods are developed to suit the cell types that are under investigation. Specifically, understanding cellular morphology is crucial for creating methods that enable reproducibility and accurate results.

In developing flow cytometric methods for bacterial enumeration, researchers must ensure that samples contain single cells. In many sample types, the bacteria of interest in their planktonic form are commonly found as single cells. However, there are several bacteria that also most commonly exist as doublets or chains that can impact the method used for enumeration (23–26). Additionally, it is critical to understand cellular morphology that may impact the enumeration method, such as binary fission or species-specific physiological changes (27,28).

Here, we used the wine bacterium, *O. oeni*, which most commonly survives in doublets and can form chains greater than seven cells in length (24). *O. oeni* was chosen as the model species for this work to detail a thorough approach for enumerating small, chain-forming bacteria in wine using flow cytometry. Additionally, the flow cytometric analysis of *S. cerevisiae* alongside *O. oeni* was utilized to demonstrate further applicability of flow cytometry for wine microbial analysis. The cellular morphology of *O. oeni* alters throughout different phases of growth, achieving cell budding, binary fission, and a pomegranate complex, which encapsulates numerous cells (29). These properties can lead to inaccurate enumeration when using colony counts on agar plates and flow cytometry. Therefore, when utilizing flow cytometry as an enumeration method for any bacterium that clumps or chains, certain checks must be performed.

MATERIALS AND METHODS

Media and Juice Production

Shiraz juice was extracted from destemmed, crushed Shiraz grapes harvested from the Waite Campus Coombe vineyard, Urrbrae, South Australia in 2017 (30). Following crushing, the grapes and juice were macerated at 0°C for 7 days to aid polyphenolic extraction. No antimicrobial agents or SO_2 were added to the juice during crushing. The grape must was pressed, then the juice was stored at −20°C until use. Chardonnay juice was extracted from destemmed, crushed Chardonnay grapes harvested from the Scarpantoni Estate vineyard, McLaren Flat, South Australia in 2020. No antimicrobial agents or SO_2 were added to the juice during crushing. The juice was stored at 4°C prior to use. Prior to use, Shiraz and Chardonnay juices were filtered at 0.45 μm using an in-line groundwater filter (Air-Met Scientific, Victoria, Australia) to remove grape solids, followed by two treatments of filter sterilization (0.2 μm). Liquid De Man, Rogosa and Sharpe (MRS; Amyl Media, Victoria, Australia) was sterilized by autoclaving (121°C, 0.1 MPa, 20 min), cooled and supplemented with 20% filter sterilized (0.2 μm) apple juice (MRSAJ).

O. oeni and *S. cerevisiae* Cell Culture

Two commercial freeze-dried *O. oeni* strains, Enoferm Alpha (Lallemand Inc., Australia) and O-Mega (Lallemand Inc.), were rehydrated in MRSAJ. After rehydration, 1 ml was transferred into three separate sterile tubes containing 9 ml of MRSAJ. Cultures were incubated anaerobically at 30°C for 4 days. A commercially available *Saccharomyces cerevisiae* strain, NT50 (Vintessential Laboratories, Victoria, Australia), was rehydrated in 30°C MRSAJ prior to dilution and flow cytometric analysis.

Dilution Assay

O. oeni and *S. cerevisiae* cultures were inverted to homogenize cells. Prior to dilution, *S. cerevisiae* and *O. oeni* cultures were either initially diluted (pure cultures) or combined to create a *S. cerevisiae* and *O. oeni* culture. For *O. oeni* samples, 750 μl of culture and 250 μl of sterile MRSAJ were transferred to a 1.5 ml microcentrifuge tube, while 250 μl of culture and 750 μl of MRSAJ were transferred to a microcentrifuge tube for *S. cerevisiae* samples. Samples for *O. oeni* mixed with *S. cerevisiae* were prepared by combining 750 μl of *O. oeni* culture and 250 μl of *S. cerevisiae* culture in a microcentrifuge tube. The tubes were inverted to mix and centrifuged at 20,238*g* for 2 min. The supernatant was removed then 1 ml of phosphate buffered saline (PBS; pH 7.0) was added. The cells were mixed by pipette and centrifugation repeated. The supernatant was again removed then cells were resuspended in 1 ml of PBS. All washed cultures were serially diluted 1:5 with PBS prior to flow cytometric analysis and microscopy.

Microscopy

For each sample that contained *S. cerevisiae*, 10 μl of 1:25 diluted sampled was transferred to a hemocytometer chamber and observed at 400× magnification. Concentrations (cells ml^{-1}) were calculated for each *S. cerevisiae*-containing sample after counting cells in five squares from each grid. For *O. oeni*, a Helber bacteria, Thoma ruling bacterial counting chamber (ProSciTech, Queensland, Australia) was used to calculate sample concentrations. Three individual mounting liquids were used which included PBS, 60% glycerol and 70% glycerol. Further to the three mounting media liquids, drying the sample to a clean glass slide was also used as a sample preparation method.

Flow Cytometry

Flow cytometry was performed for pure *O. oeni*, pure *S. cerevisiae* and mixed *O. oeni* and *S. cerevisiae* at 1:125, 1:625, 1:3125, 1:15625, and 1:78125 dilutions. Prior to flow cytometric analysis, samples were stained with a final concentration of 2 µM SYTO 9 nucleic acid dye (Invitrogen, Waltham, MA), incubated at room temperature for 10 min, and analyzed to determine *S. cerevisiae* and *O. oeni* concentration. Filtered (0.2 µm) Shiraz, Chardonnay, MRSAJ and PBS were stained with SYTO 9 nucleic acid dye (2 µM final concentration), incubated at room temperature for 10 min, and analyzed for particulate and non-specific noise. A flow cytometry sub-micron particle size reference kit (Invitrogen) was used for particle size reference. Green fluorescent beads of 0.2, 0.5, 1.0, and 2.0 µm sizes were used by adding one drop of bead solution into 1 ml of 0.2 µM filtered MilliQ water. Each diluted bead solution at a volume of 50 µl was added to a microcentrifuge tube and mixed prior to flow cytometric analysis. Samples were analyzed on a Guava® easyCyte™ 12HT flow cytometer with the threshold set to 11 on the forward scatter channel (FSC) or 100 on the green-blue (Grn-B) channel. Events were collected for 2 min at a flow rate of 0.118 µl s^{-1}. All instrument settings can be found on the MIFlowCyt checklist, uploaded with individual FCS 2.0 and FCS 3.0 files at http://flowrepository.org/id/FR-FCM-Z2M7. Data analysis and gating was performed using guavaSoft 3.3 flow cytometry software and histogram plots generated using FCS express 7 (De Novo Software).

The concentration for each dilution of each sample was determined using the following equation:

$$\text{Concentration}\left(\text{particles ml}^{-1}\right) = \text{Dilution factor} \times \text{V} \times \text{adjusted particle count}$$

where $V = \frac{1000}{\text{Volume measured }(\mu\text{l})}$

The adjusted particle count is calculated by the subtraction of particles situated in the gated region of the PBS control sample from the particle count in the gated region of the test sample.

For *O. oeni* samples, the concentration for the 1:3125, 1:15625, and 1: 78125 dilutions were averaged for each biological replicate, and subsequently the mean across all replicates was determined. This same process was used for *S. cerevisiae* concentration calculations, with the exception of using the 1:125, 1:625, 1:3125, and 1:15625 dilutions.

RESULTS

Flow Cytometry

Flow cytometric analysis of the mixed *S. cerevisiae* and *O. oeni* serial dilution samples revealed that the method was able to measure *S. cerevisiae* alone and *S. cerevisiae* mixed with *O. oeni* (Fig. 1). The *O. oeni* population displayed considerable spread over both FSC and side scatter measures (SSC; Figs. 1 and 2). Analysis of sub-micron beads demonstrated that as particles became smaller (<0.5 µm) the FSC population spread increased (Fig. 2). Bead populations were able to be separated by SSC rather than FSC, as the 0.2 and 0.5 µm bead populations could not be differentiated by FSC (Fig. 2B). In comparison to beads, *O. oeni* cell populations ranged between <0.2 µm and 1.0 µm (Fig. 2B), while *S. cerevisiae* were > 2.0 µm (Fig. 2C). Flow cytometry of the 1:125, 1:625, 1:3125, and 1:15625 diluted *S. cerevisiae* alone and *O. oeni* mixed with *S. cerevisiae* samples resulted in an average of $3.31 \pm 1.74 \times 10^7$ *S. cerevisiae* cells ml^{-1} (Supporting Information Table S1). The raw *S. cerevisiae* cell counts achieved using flow cytometry were on average 1,234 ± 215 cells for the 1:125 diluted sample analyzed for 2 min. The cytograms also revealed two *S. cerevisiae* populations on the Grn-B parameter, indicating *S. cerevisiae* cell budding (Fig. 1). For *O. oeni* Enoferm Alpha and O-Mega, an average of $2.19 \pm 0.98 \times 10^9$ and $1.77 \pm 0.48 \times 10^9$ bacterial particles ml^{-1} were measured for *O. oeni* alone and *O. oeni* mixed with *S. cerevisiae* samples, respectively (Supporting Information Table S1). Flow cytometric estimations for *O. oeni* were determined from 1:3,125, 1:15,625, and 1:78,125 dilutions. The raw bacteria cell counts achieved using flow cytometry were on average 3,792 ± 873 and 3,312 ± 349 cells for Enoferm Alpha and O-Mega 1:3125 diluted samples analyzed for 2 min, respectively. Raw cell counts for all dilutions are presented in the Supporting Information Table S2.

Initial cytometric analysis revealed that the chosen growth media can result in particulate interference (Fig. 3). All three growth media demonstrated some particulate noise that could interfere with the *O. oeni* population for the forward scatter or side scatter parameters (Fig. 3). PBS also had particulate noise when the threshold was set to 11 on the FSC channel (Fig. 3C). However, this was eliminated by setting the threshold value to 100 on the Grn-B channel (Fig. 3A).

Microscopy

S. cerevisiae cells were counted using a hemocytometer and were used for comparison with flow cytometric results. The 1:25 dilution of samples was used for microscopy resulting in an average *S. cerevisiae* concentration of $8.82 \pm 1.96 \times 10^7$ cells ml^{-1} across all samples. The average raw cell count was 71 ± 16 cells in 10 µl of diluted sample. Determining *O. oeni* concentration by microscopy was inhibited by multiple factors. Due to their size, accurate counting of *O. oeni* required magnification of 1,000×. The depth of the counting chamber did not allow use of an oil-immersion 100× lens. Brownian motion led to *O. oeni* cells moving at such a rate that resulted in an inability to know which cells had been already counted. Thickened mounting media was used to reduce Brownian motion; however, it resulted in an inability to visualize the counting grid.

DISCUSSION

Assessing *O. oeni* and *S. cerevisiae* samples by flow cytometry through serial dilutions demonstrated the successful cytometric enumeration of these cells (Fig. 1). The dilution assay was performed with two commercial *O. oeni* strains, Enoferm Alpha and O-Mega, to demonstrate reproducibility. *S. cerevisiae* enumeration was compared for flow cytometry and microscopy, revealing comparable results for both methods (Supporting

(A) *O. oeni* alone

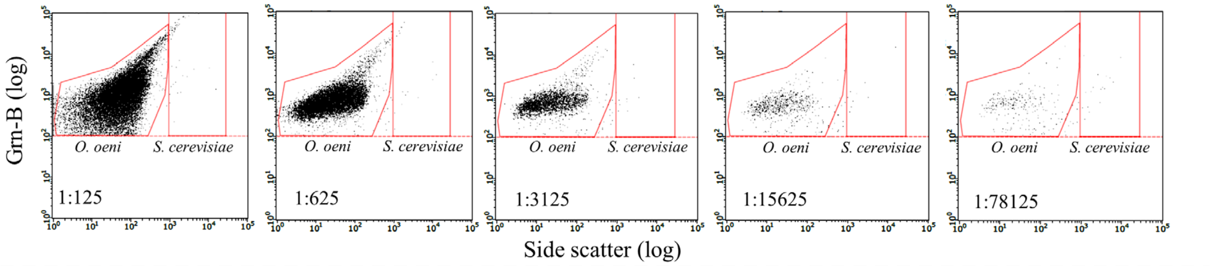

(B) *S. cerevisiae* alone

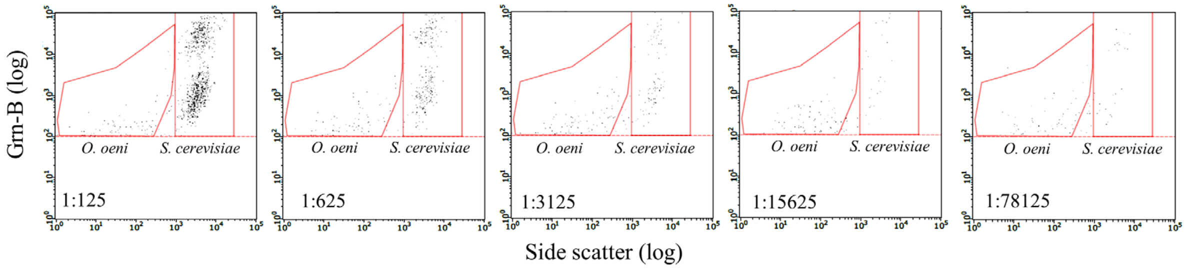

(C) *O. oeni* and *S. cerevisiae* combined

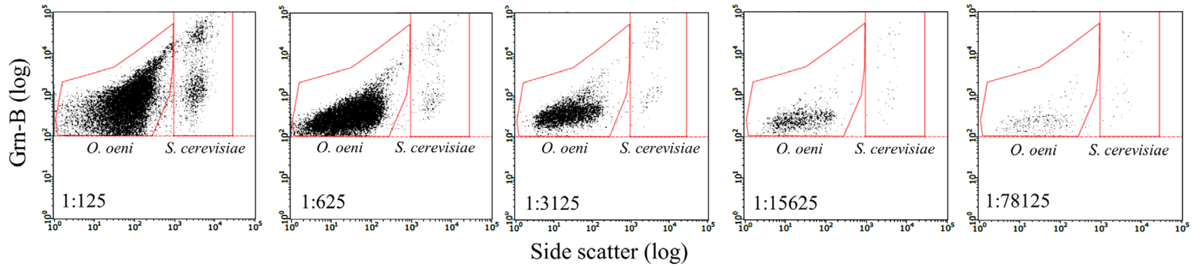

Figure 1. Dilution assay for one replicate of *O. oeni*strain Enoferm Alpha alone (**A**), *S. cerevisiae* alone (**B**) and *O. oeni* Enoferm Alpha mixed with *S. cerevisiae* (**C**). Samples were washed once with 1x PBS, serially diluted 1:5 and stained with 2 μM SYTO 9 nucleic acid dye before analyzing samples at various dilutions, shown in the bottom right of each cytogram. The gates for *S. cerevisiae* and *O. oeni* populations are displayed on each cytogram in red. Threshold was set to 100 on the Grn-B channel and events were collected for 2 min. [Color figure can be viewed at wileyonlinelibrary.com]

Information Table S1). Although the average *S. cerevisiae* concentration was lower for flow cytometry compared to microscopy, the variance was smaller for flow cytometry results. Cytograms revealed two populations of *S. cerevisiae* cells on the Grn-B channel (Fig. 1B, C); however, this has been reported to relate to *S. cerevisiae* cell budding and a feature of asynchronous *S. cerevisiae* populations (31,32). Flow cytometry offered the benefit of assessing more volume and counting more cells compared to microscopy, which may underlie the difference in *S. cerevisiae* concentrations calculated for the two methods. Nevertheless, this demonstrated that the approach used was able to discern *S. cerevisiae* cells in a mixed *S. cerevisiae* and *O. oeni* sample (Fig. 1).

It was necessary to wash cells in 1x PBS prior to analysis since the use of *O. oeni* growth medium, MRSAJ, resulted in particulate noise (Fig. 3). In addition, 0.2 μm filtered Chardonnay and Shiraz juice also contained the presence of particulate noise (Fig. 3). Although *O. oeni* was not measured in Shiraz and Chardonnay juice for this work, it is commonly assessed in these juice types (33,34) and therefore it was necessary to demonstrate potential for particulate noise in these backgrounds. Given that MRSAJ, Shiraz and Chardonnay juice all had some particulate noise (Fig. 3), staining cells with a nucleic acid dye, SYTO 9, prior to analysis was required to enable a more appropriate threshold and separation of *O. oeni* cells from particulate matter, thereby eliminating nonspecific particulate interference. Furthermore, using a forward scatter threshold and no stain could cause highly inaccurate cell counts due to nonspecific noise situated in the same space as *O. oeni* cells (Fig. 3B, C).

Flow cytometry of *O. oeni* by itself, and in a mixture with *S. cerevisiae* cells, resulted in an abundance of $2.19 \pm 0.98 \times 10^9$ and $1.77 \pm 0.48 \times 10^9$ bacterial particles ml^{-1} for Enoferm Alpha and O-Mega, respectively. Although promising, these estimates may not be truly representative of the total numbers of *O. oeni* in the samples, and values obtained for *O. oeni* should be questioned and thoroughly evaluated prior to publication. As is observed with colony

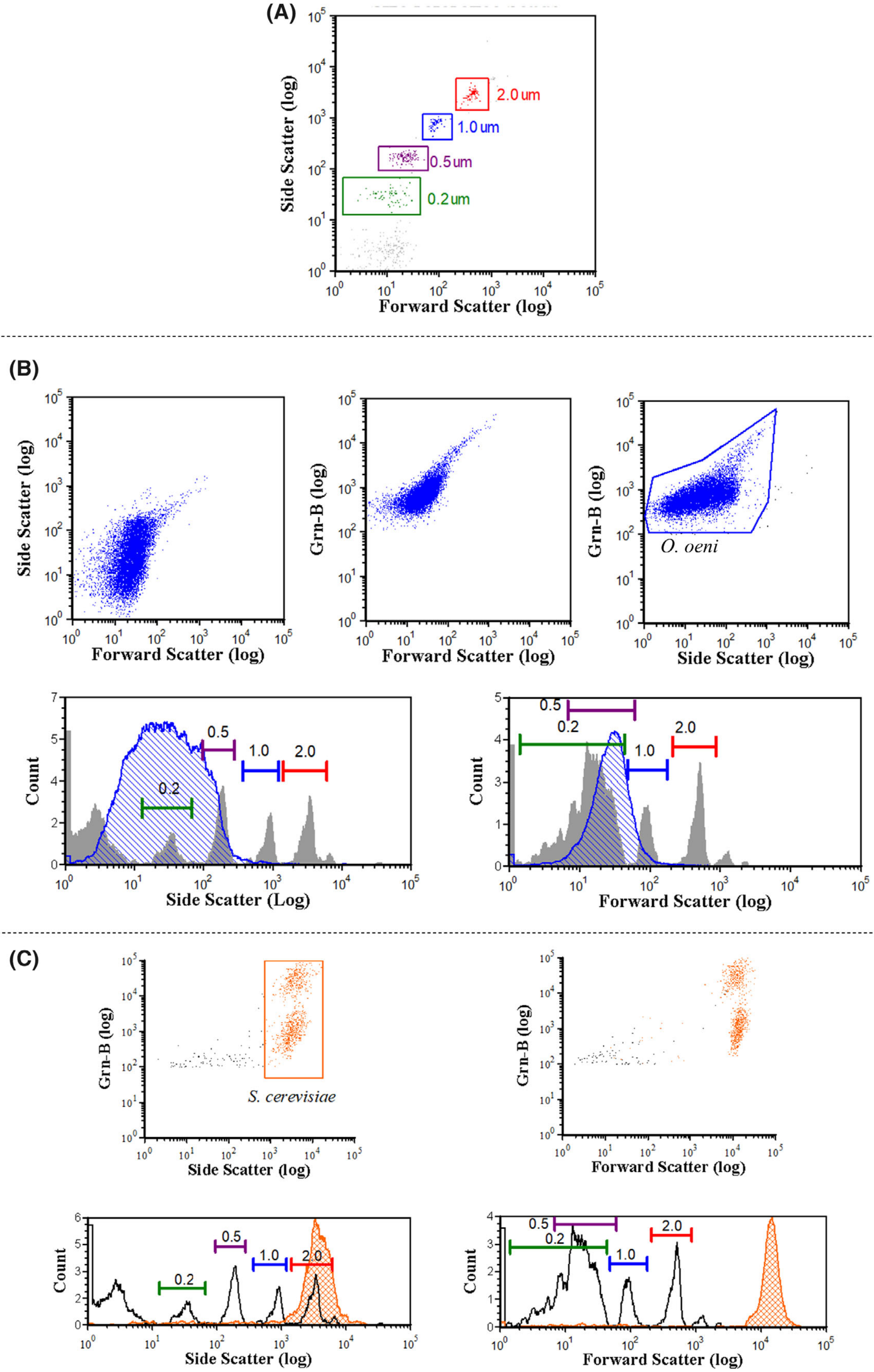

Figure 2. Legend on next page.

(A) Threshold Grn-B 100; SSC vs Grn-B

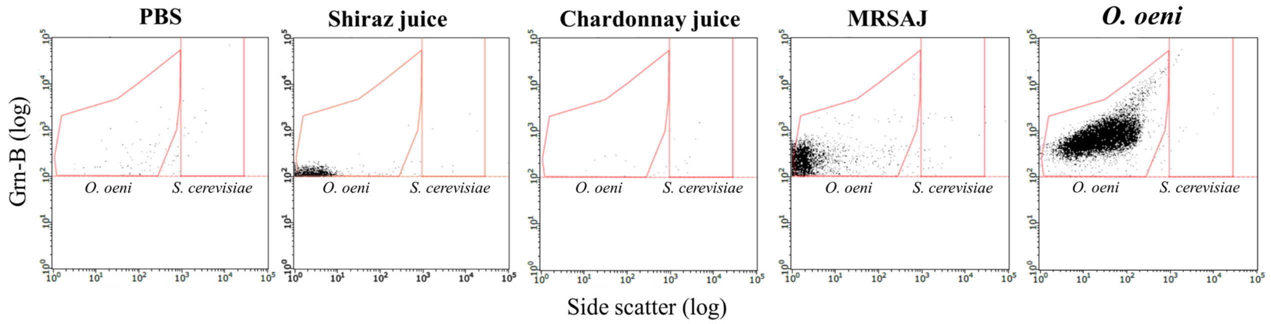

(B) Threshold Grn-B 100; SSC vs FSC

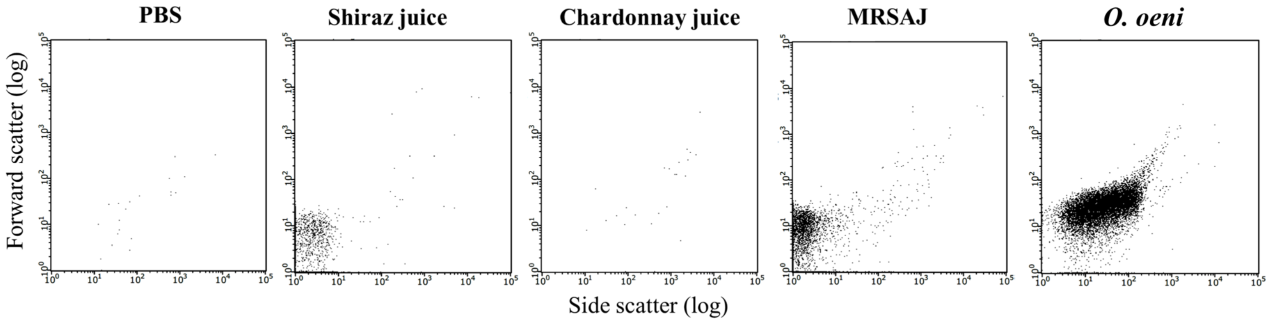

(C) Threshold FSC 11

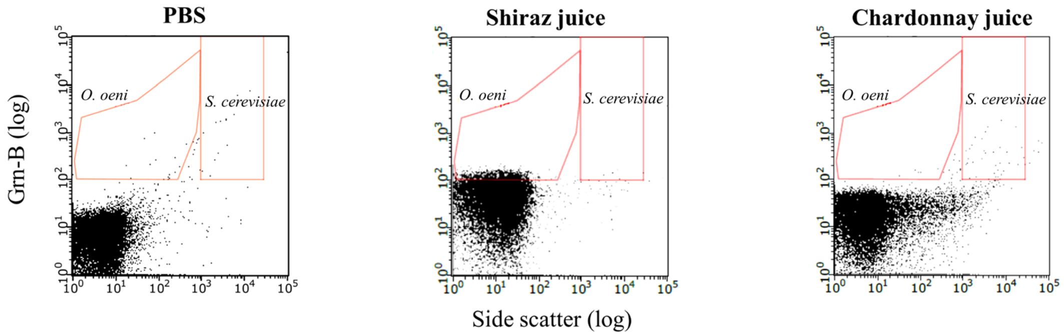

Figure 3. Particulate noise in PBS, Shiraz and Chardonnay juices and MRSAJ compared with an *O. oeni* population. All samples were stained with 2 μM SYTO 9 nucleic acid dye and Shiraz and Chardonnay juices were filtered at 0.2 μm prior to staining. (**A**) Side scatter vs Grn-B cytograms for each of the samples, when threshold is set to 100 on the Grn-B channel. (**B**) Forward scatter vs side scatter cytograms with a threshold of 100 on the Grn-B channel. (**C**) Side scatter vs Grn-B for PBS and shiraz and chardonnay juices when threshold was set to 11 on the forward scatter channel. MRSAJ and *O. oeni* samples were not assessed with these parameters. All samples were analyzed for 2 min or up to 5,000 events. [Color figure can be viewed at wileyonlinelibrary.com]

Figure 2. (**A**) Flow cytometric analysis of sub-micron particle size reference beads using sizes of 0.2 (green), 0.5 (purple), 1.0 (blue), and 2.0 (red) μm in 0.2 μm filtered MilliQ water. (**B**) Gated population of Enoferm Alpha, at a 1:625 dilution. The gated *O. oeni* population (blue) is superimposed on the two other scatter plots, side scatter vs forward scatter and Grn-B vs forward scatter, which highlights a population shift between chosen parameters. Comparison of bead populations (gray) from (A), with *O. oeni* population (blue) displayed in the scatter plots. The histogram plots display the populations for side scatter (left) and forward scatter (right). Markers are displayed for the bead sizes in μm, which match the corresponding gates in (A). (**C**) Scatter plots of a 1:125 diluted *S. cerevisiae* sample, with Grn-B vs side scatter (left) and Grn-B vs forward scatter (right). The *S. cerevisiae* population is gated and colored orange. Histograms demonstrating the comparison of *S. cerevisiae* cell size (orange crosshatch) compared to particle size reference beads (black outline) for side scatter (left) and forward scatter (right) are presented below. Markers are displayed for each bead size in μm. The same cytometer settings were used for all samples, with threshold set to 100 on the Grn-B channel. [Color figure can be viewed at wileyonlinelibrary.com]

growth plates, chaining or aggregated cells may be recorded as a single particle by a flow cytometer (35,36). If the bacteria are in chains, this theoretically will be detected as a single particle that would have much larger side scatter and forward scatter values in comparison to a single bacterium. Cell aggregation or doublets are not unique to bacterial cells and have been observed for yeast and human cell types (37,38). In flow cytometry, discrimination of doublets for larger cell types can be determined by assessing FSC-Area vs FSC-Height. However, the discrimination may not be clear enough to accurately separate singlet and doublet populations (37). The presence of doublets and chains could explain the side-scatter spread of the bacterial population seen in flow cytometry cytograms of *O. oeni* (Figs. 1 and 2B). Due to the size of *O. oeni* cells, the population displayed in cytograms is further spread out compared to the larger *S. cerevisiae* cells (Fig. 2B, C). As particle sizes become smaller, the FSC spread increases, as was demonstrated using sub-micron beads (Fig. 2A). The range of spread is dependent on the specificity and power of the instrument (39), and in this instance, the smaller particle sizes are nearing the limits of detection for the flow cytometer. It was clear that SSC was more appropriate for differentiation of small particles (<0.5 μm; Fig. 2A, B) while FSC was more appropriate for larger particle size estimation (>1.0 μm; Fig. 2C). The log scale results in a tighter population for *S. cerevisiae* cells because their size range is larger, leading to distribution across a higher log value but smaller log range (SSC value 2,000–9,000 = 10^3 to 10^4) compared to *O. oeni* cells that are distributed across a smaller log value but larger log range (SSC value 2–1,000 = 10^0 to 10^3). Using the sub-micron beads for size comparison, the spread of *O. oeni* cells corresponds to a size range between <0.2 μm and 1.0 μm (Fig. 2B). This range is different from the reported cell size range of 0.2 and 0.6 μm (29). From this, it is reasonable to assume that the particle sizes measured for *O. oeni* range greatly in size and complexity, which could relate to chain formation or cell aggregation. *O. oeni* may form chains of multiple different lengths; therefore, there would not be a clear cytogram population. Instead, a scattered distribution over the SSC parameter would be visible, which was demonstrated in this work (Figs. 1 and 2).

Comparison of cells with reference beads should also be treated with caution since the refraction index of beads could differ from cells (40). For smaller cells, estimating size could be problematic if the cells are close to the limit of detection for the machine. Particles in the *O. oeni* sample that lay in the region <0.2 μm, as compared to the sub-micron reference beads, cannot be discounted as bacterial cells, since the range of the refractive index of *O. oeni* cells and the additive effects of the flow cytometer detection limit are unknown. A major consideration when utilizing flow cytometry for bacterial cell enumeration is the occurrence of binary fission. For larger cell sizes (> 1 μm), cells that are replicating and forming daughter cells may be distinguishable using SSC (41). However, for small cells, this differentiation becomes difficult due to flow cytometer detection limits. It is also difficult to determine what proportion of cells might be undergoing binary fission at any one time, unless cellular reproduction is specifically inhibited.

Flow cytometry can offer a fast, reliable solution to enumerate bacteria from various environments. However, much more work is needed to optimize this method to ensure small, chain-forming bacteria are enumerated accurately and produce reliable results. For now, it is not possible to determine how many *O. oeni* cells are present in a chain or an aggregate based on the side or forward scatter values obtained. The development of a method to break chained cells prior to flow cytometric analysis would be one way to combat this issue. However, this presents new challenges to estimating abundance since some bacterial de-chaining methods involve sonication (42), which is harsh and may damage cells in the process.

New technologies are constantly being produced to allow researchers to look deeper into their microbial samples. For example, the Amnis ImageStream (Luminex, Japan) is a flow cytometer that can take an image of every particle that passes through the machine's laser, which could aid in tackling problems such as bacterial chaining. Alternatively, there are cytometers that can provide data on the shape of the pulse generated from scanning a particle, such as the CytoSense (CytoBuoy, the Netherlands; 43,44). A pulse scan may provide more detail on particle morphology compared to recording a single value for each particle. Currently, these technologies require optimization for small cells such as *O. oeni*. Developing methods for such technology to enumerate bacteria, whether they are in chains, undergoing binary fission or singular, could allow for much more accurate counts of bacterial abundance. This would create a significant positive impact not only on the wine industry, but any bacterial research, at the global scale.

Currently, there is a plethora of data identifying bacterial taxa in a range of environments, but the determination of bacterial cell abundance is less prominent. Reporting enumeration with species identification data would enable a greater overall picture of microbial ecology. The development of more precise, high-powered flow cytometers will also lead to easier abundance estimation of small microorganisms, but until then researchers must be aware of the current limitations of small cell flow cytometry methods.

ACKNOWLEDGMENTS

This work was supported by Australia's grape growers and winemakers through their investment body, Wine Australia, with matching funds from the Australian Government. L.B. was supported by joint scholarships from The University of Adelaide and Wine Australia (AGW Ph 1510).

CONFLICT OF INTEREST

The authors declare no conflict of interest.

ETHICS STATEMENT

This work for this article did not require ethics approval.

AUTHOR CONTRIBUTIONS

Louise Bartle: Conceptualization; data curation; formal analysis; methodology; writing-original draft; writing-review and editing. **James Mitchell:** Conceptualization; formal analysis; methodology; supervision; writing-original draft; writing-review and editing. **James Paterson:** Conceptualization; formal analysis; methodology; supervision; writing-original draft; writing-review and editing.

LITERATURE CITED

1. Le Chatelier E, Nielsen T, Qin J, Prifti E, Hildebrand F, Falony G, Almeida M, Arumugam M, Batto JM, Kennedy S, et al. Richness of human gut microbiome correlates with metabolic markers. Nature 2013;500:541–546.
2. Davenport ER, Mizrahi-Man O, Michelini K, Barreiro LB, Ober C, Gilad Y. Seasonal variation in human gut microbiome composition. PLoS One 2014;9:e90731.
3. Cho JC, Kim SJ. Increase in bacterial community diversity in subsurface aquifers receiving livestock wastewater input. Appl Environ Microbiol 2000;66:956–965.
4. Roudnew B, Seymour JR, Jeffries TC, Lavery TJ, Smith RJ, Mitchell JG. Bacterial and virus-like particle abundances in purged and unpurged groundwater depth profiles. Groundw Monit Remediat 2012;32:72–77.
5. Smith RJ, Paterson JS, Wallis I, Launer E, Banks EW, Bresciani E, Cranswick RH, Tobe SS, Marri S, Goonan P, et al. Southern south Australian groundwater microbe diversity. FEMS Microbiol Ecol 2018;94:158.
6. Gilbert JA, Steele JA, Caporaso JG, Steinbrück L, Reeder J, Temperton B, Huse S, McHardy AC, Knight R, Joint I, et al. Defining seasonal marine microbial community dynamics. ISME J 2012;6:298–308.
7. Santelli CM, Orcutt BN, Banning E, Bach W, Moyer CL, Sogin ML, Staudigel H, Edwards KJ. Abundance and diversity of microbial life in ocean crust. Nature 2008; 453:653–656.
8. Morgan HH, du Toit M, Setati ME. The grapevine and wine microbiome: insights from high-throughput amplicon sequencing. Front Microbiol 2017;8:820.
9. Portillo M del C, Franquès J, Araque I, Reguant C, Bordons A. Bacterial diversity of Grenache and Carignan grape surface from different vineyards at Priorat wine region (Catalonia, Spain). Int J Food Microbiol 2016;219:56–63.
10. Botta C, Cocolin L. Microbial dynamics and biodiversity in table olive fermentation: culture-dependent and -independent approaches. Front Microbiol 2012;3:245.
11. Chakravorty S, Bhattacharya S, Chatzinotas A, Chakraborty W, Bhattacharya D, Gachhui R. Kombucha tea fermentation: microbial and biochemical dynamics. Int J Food Microbiol 2016;220:63–72.
12. Lonvaud-Funel A. Lactic acid bacteria in the quality improvement and depreciation of wine. Anton Van Leeuwen 1999;76:317–331.
13. Carlson-Jones JA, Kontos A, Kennedy D, Martin J, Lushington K, McKerral J, Paterson JS, Smith RJ, Dann LM, Speck P, et al. The microbial abundance dynamics of the paediatric oral cavity before and after sleep. J Oral Microbiol 2020;12: 1741254.
14. Engh G, Ulloa O, Karl DM. Monitoring microbial communities in the marine environment. Cytom Part A 2019;95A:717–721.
15. McHugh IOL, Tucker AL. Flow cytometry for the rapid detection of bacteria in cell culture production medium. Cytom Part A 2007;71A:1019–1026.
16. Yamaguchi N, Sasada M, Yamanaka M, Nasu M. Rapid detection of respiring *Escherichia coli* O157:H7 in apple juice, milk, and ground beef by flow cytometry. Cytom Part A 2003;54A:27–35.
17. Bisson LF, Butzke CE. Diagnosis and rectification of stuck and sluggish fermentations. Am J Enol Viticult 2000;51:168–177.
18. Malacrinò P, Zapparoli G, Torriani S, Dellaglio F. Rapid detection of viable yeasts and bacteria in wine by flow cytometry. J Microbiol Methods 2001;45:127–134.
19. Salma M, Rousseaux S, Sequeira-Le Grand A, Alexandre H. Cytofluorometric detection of wine lactic acid bacteria: Application of malolactic fermentation to the monitoring. J Ind Microbiol Biotechnol 2013;40:63–73.
20. Czechowska K, Johnson DR, Roelof Van Der Meer J. Use of flow cytometric methods for single-cell analysis in environmental microbiology. Curr Opin Microbiol 2008;11:205–212.
21. Frossard A, Hammes F, Gessner MO. Flow cytometric assessment of bacterial abundance in soils, sediments and sludge. Front Microbiol 2016;7:903.
22. Van Nevel S, Koetzsch S, Proctor CR, Besmer MD, Prest EI, Vrouwenvelder JS, Knezev A, Boon N, Hammes F. Flow cytometric bacterial cell counts challenge conventional heterotrophic plate counts for routine microbiological drinking water monitoring. Water Res 2017;113:191–206.
23. Thibodeau EA, Ford CM. Chain formation and de-chaining in *Streptococcus sobrinus* SL-1. Oral Microbiol Immun 1991;6:313–315.
24. Grandvalet C. *Oenococcus oeni*: Queen of the cellar, nightmare of geneticists. Microbiology 2017;163:297–299.
25. Beech JP, Ho BD, Garriss G, Oliveira V, Henriques-Normark B, Tegenfeldt JO. Separation of pathogenic bacteria by chain length. Anal Chim Acta 2018;1000:223–231.
26. Saxena S, Mtech SS, Tembhurkar AR. Biotechnological approach for enhancing the properties of mortar using treated wastewater. Eng Sustain 2019;173:97–106.
27. Calvert MEK, Lannigan JA, Pemberton LF. Optimization of yeast cell cycle analysis and morphological characterization by multispectral imaging flow cytometry. Cytom Part A 2008;73A:825–833.
28. Yamamoto M, Handa S, Kawano S. DNA content of *Stichococcus bacillaris* (Trebouxiophyceae, Chlorophyta) nuclei determined with laser scanning cytometry. Cytologia 2011;76:157–161.
29. Wang Y, Liu S, Su J, Zhang Y, Li J, Sui YQ, Li YY, Wang H, Li H. Three novel structural phenomena in the cellular ontogeny of *Oenococcus oeni* from northern China. Sci Rep 2017;7:1–10.
30. Bartle L. Identification and Understanding of *Saccharomyces* and *Oenococcus* Interactions in Wine Fermentation. Dissertation, The University of Adelaide 2020.
31. Haase SB, Lew DJ. Flow cytometric analysis of DNA content in budding yeast. Method Enzymol 1997;283:322–332.
32. Rosebrock AP. Analysis of the budding yeast cell cycle by flow cytometry. Cold Spring Harb Protoc 2017;2017(1). http://dx.doi.org/10.1101/pdb.prot088740.
33. Larsen JT, Nielsen JC, Kramp B, Richelieu M, Bjerring P, Riisager MJ, Arneborg N, Edwards CG. Impact of different strains of *Saccharomyces cerevisiae* on malolactic fermentation by *Oenococcus oeni*. Am J Enol Viticult 2003;54:246–251.
34. Abrahamse CE, Bartowsky EJ. Timing of malolactic fermentation inoculation in shiraz grape must and wine: Influence on chemical composition. World J Microb Biot 2012;28:255–265.
35. Jennison MW. The relations between plate counts and direct microscopic counts of *Escherichia coli* during the logarithmic growth period. J Bacteriol 1937;33:461–477.
36. Resina-Pelfort O, Garc M, Ortega-Calvo J, Comas-Riu J, Vives-Rego J. Flow cytometry discrimination between bacteria and clay-humic acid particles during growth-linked biodegradation of phenanthrene by *Pseudomonas aeruginosa* 19SJ. FEMS Microbiol Ecol 2003;43:55–61.
37. Cosma A. The nightmare of a single cell: Being a doublet. Cytom Part A 2020;97A: 768–771.
38. Knutsen JHJ, Rein ID, Rothe C, Stokke T, Grallert B, Boye E. Cell-cycle analysis of fission yeast cells by flow cytometry. PLoS One 2011;6:e17175.
39. Davey HM, Kell DB. Flow cytometry and cell sorting of heterogeneous microbial populations: The importance of single-cell analyses. Microbiol Rev 1996;60:641–696.
40. Life Technologies. Flow cytometry sub-micron particle size reference kit. https://www.thermofisher.com/document-connect/document-connect.html?url=https%3A%2F%2Fassets.thermofisher.com%2FTFS-Assets%2FLSG%2Fmanuals%2Fmp13839.pdf&title=RmxvdyBDeXRvbWV0cnkgU3ViLW1pY3JvbiBQYXJ0aWNsZSBTaXplIFJlZmVyZW5jZSBLaXQ= 2020.
41. Roostalu J, Jõers A, Luidalepp H, Kaldalu N, Tenson T. Cell division in *Escherichia coli* cultures monitored at single cell resolution. BMC Microbiol 2008;8:68.
42. Bitoun JP, Liao S, Yao X, Xie GG, Wen ZT. The redox-sensing regulator rex modulates central carbon metabolism, stress tolerance response and biofilm formation by *Streptococcus mutans*. PLoS One 2012;7:e44766.
43. Fragoso GM, Poulton AJ, Pratt NJ, Johnsen G, Purdie DA. Trait-based analysis of subpolar North Atlantic phytoplankton and plastidic ciliate communities using automated flow cytometer. Limnol Oceanogr 2019;64:1763–1778.
44. Fontana S, Jokela J, Pomati F. Opportunities and challenges in deriving phytoplankton diversity measures from individual trait-based data obtained by scanning flow-cytometry. Front Microbiol 2014;5:324.

CYTOMETRY
Journal of Quantitative Cell Science PART A

A Systematic Approach to Improve Scatter Sensitivity of a Flow Cytometer for Detection of Extracellular Vesicles

Leonie de Rond,[1,2,3]* Edwin van der Pol,[1,2,3] Paul R. Bloemen,[1] Tina Van Den Broeck,[4] Ludo Monheim,[4] Rienk Nieuwland,[2,3] Ton G. van Leeuwen,[1,3] Frank A.W. Coumans[1,2,3]

[1] Biomedical Engineering and Physics, Amsterdam UMC, University of Amsterdam, Amsterdam, The Netherlands

[2] Laboratory Experimental Clinical Chemistry, Amsterdam UMC, University of Amsterdam, Amsterdam, The Netherlands

[3] Vesicle Observation Center, Amsterdam UMC, University of Amsterdam, Amsterdam, The Netherlands

[4] BD Biosciences, Erembodegem, Belgium

Received 9 July 2019; Revised 6 November 2019; Accepted 6 January 2020

Grant sponsor: Netherlands Organisation for Scientific Research, Grant number: VENI 13681, Grant number: VENI 15924, Grant number: STW Perspectief Program CANCER-ID 14195

Additional Supporting Information may be found in the online version of this article.

*Correspondence to: Leonie de Rond, Department of Biomedical Engineering and Physics, Cancer Center Amsterdam, Amsterdam Cardiovascular Sciences, Amsterdam UMC, University of Amsterdam, Meibergdreef 9, 1105AZ Amsterdam, The Netherlands
Email: l.derond@amsterdamumc.nl

DOI: 10.1002/cyto.a.23974

Abstract

Extracellular vesicles (EVs) are commonly studied by flow cytometry. Due to their small size and low refractive index, the scatter intensity of most EVs is below the detection limit of common flow cytometers. Here, we aim to improve forward scatter (FSC) and side scatter (SSC) sensitivity of a common flow cytometer to detect single 100 nm EVs. The effects of the optical and fluidics configuration on scatter sensitivity of a FACSCanto (Becton Dickinson) were evaluated by the separation index (SI) and robust coefficient of variation (rCV) of polystyrene beads (BioCytex). Improvement is defined as increased SI and/or reduced rCV. Changing the obscuration bar improved the rCV 1.9-fold for FSC. A 10-fold increase in laser power improved the SI 19-fold for FSC and 4.4-fold for SSC, whereas the rCV worsened 0.8-fold and improved 1.5-fold, respectively. Confocalization worsened the SI 1.2-fold for FSC, and improved the SI 5.1-fold for SSC, while the rCV improved 1.1-fold and worsened 1.5-fold, respectively. Replacing the FSC photodiode with a photomultiplier tube improved the SI 66-fold and rCV 4.2-fold. A 2-fold reduction in sample stream width improved both SI and rCV for FSC by 1.8-fold, and for SSC by 1.3- and 2.2-fold, respectively. Decreasing the sample flow velocity worsened rCVs. Decreasing the flow channel dimensions and the pore size of the sheath filter did not substantially change the SI or rCV. Using the optimal optical configuration and fluidics settings, the SI improved $3.8 \cdot 10^4$-fold on FSC and 30-fold on SSC, resulting in estimated detection limits for EVs (assuming a refractive index of 1.40) of 246 and 91 nm on FSC and SSC, respectively. Although a 50-fold improvement on FSC is still necessary, these adaptions have produced an operator-friendly, high-throughput flow cytometer with a high sensitivity on both SSC and FSC.

Key terms

exosomes; extracellular vesicles; flow cytometry; light scattering; microparticle

Cells release membrane-enclosed particles into their environment to communicate or to transport waste. These membrane-enclosed particles are called extracellular vesicles (EVs) and are present in all body fluids. EVs are potential biomarkers, because their concentration and composition in body fluids change with disease (1–4).

Flow cytometry is often applied to characterize EVs in body fluids, because of its high throughput and ability to distinguish between different EV populations at single-EV level based on immunophenotype (5). Figure 1A shows that the majority of EVs in human urine have a diameter <200 nm (6). In plasma, at least 47% of EVs have a diameter <200 nm (8). A recent study involving multiple centers that use flow cytometry to study EVs (7) showed that most flow cytometers do not detect EVs <200 nm based on scatter (Fig. 1A). In fact, only 6 out of the 46 flow cytometers could detect a scatter of 300 nm EVs or smaller. Moreover, due to the power–law relation between

EV concentration and diameter, the detected size range of a flow cytometer strongly affects the measured EV concentration, as shown in Figure 1B. For example, a 3-fold increase of the detected size range from >300 to >100 nm results in a 15-fold increase in the measured EV concentration.

Multiple efforts have been described toward increasing the sensitivity of a flow cytometer for the detection of submicrometer particles (9–18). Most efforts focused on improving the side scatter (SSC) sensitivity (9–13). SSC is the logical choice when a single sensitive scatter detector is required, because SSC has a dark field configuration. From the signals of a single scatter detector, it is generally possible to derive particle size if the particle refractive index is known (19–21). However, if the refractive index is unknown, only the ratio of SSC versus forward scatter (FSC) allows simultaneous determination of particle size and refractive index (22). The refractive index proved useful to distinguish EVs from non-EV particles, such as lipoproteins, which are abundantly present in plasma (23). Regardless of whether fluorescence- or scatter-based detection is used, sensitive SSC and FSC detections are required to allow determination of particle size and refractive index. In addition, none of the previous reports (9–18) showed a systematic and quantitative overview of the influence of an adaptation on the sensitivity of the flow cytometer. Such a systematic overview would provide insight in the relative contributions of the different adaptations to improve sensitivity and can indicate future directions for improvements.

Here, we systematically evaluated adaptations to the optical configuration and fluidics of a common flow cytometer (FACSCanto, Becton Dickinson [BD], Franklin Lakes, NJ), and show the resulting effects on the FSC, SSC, and fluorescence sensitivity. The evaluated adaptations include varying the obscuration bar shape, laser power, pinhole diameter, detector type, sample stream width, sample flow velocity, flow channel dimensions, and the pore size of the sheath filter. The aim is to enable detection of scatter signals from 100 nm EVs on both the FSC and SSC detectors.

MATERIALS AND METHODS

Materials

A mixture of green fluorescent polystyrene (PS) beads of 100, 300, 500, and 900 nm (Megamix-plus FSC, Stago BNL, Leiden, the Netherlands) was used to evaluate flow cytometer sensitivity with every adaptation. The sensitivity of the optimized system was demonstrated using nonfluorescent 100 ± 7.8, 125 ± 4.5, 147 ± 4.3, 203 ± 5.3, 400 ± 7.3 nm NIST traceable PS beads (mean ± standard deviation [SD], all 3000 Series Nanosphere Size Standards, Thermo Fischer Scientific, Rockford, IL), 75 ± 7.7 nm silica bead (mean ± SD, Supporting Information Fig. S1, SI-0.1, Kisker Biotech GmbH, Steinfurt, Germany), 189 ± 2 and 374 ± 10 nm hollow silica beads (mean ± uncertainty, (24)) and a urine EV sample.

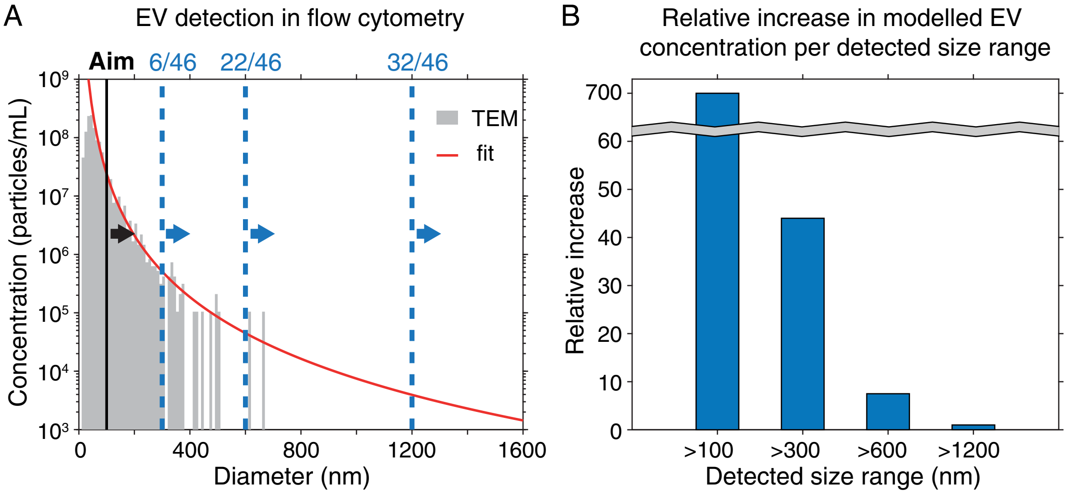

Figure 1. Extracellular vesicle (EV) detection by common flow cytometers. (**A**) Size distribution of urinary EVs (*n* = 5) as measured by transmission electron microscopy (TEM) and fitted with a power law (red line) (6). Of the 46 flow cytometers tested in (7), 32 could detect EVs >1,200 nm, 22 EVs >600 nm, and only 6 could detect EVs >300 nm. Here, we aim to enable detection of EVs >100 nm (black line). (**B**) Increase in detected EV concentration as a function of the detected size range relative to the concentration of EVs >1,200 nm. [Color figure can be viewed at wileyonlinelibrary.com]

Urine EV Sample

Urine from five overnight fasting healthy male donors was collected and processed as described earlier (25). Informed consent and approval from the ethics committee was obtained. Briefly, urine was pooled and centrifuged for 10 min at 180 *g*, 4°C, followed by 20 min at 1,560 *g*, 4°C to remove cells. Aliquots of 1 ml of the resulting cell-free urine were snap-frozen in liquid nitrogen and stored at −80°C. Before use, 12 aliquots of cell-free urine were thawed at 37°C, pooled, and centrifuged for 10 min at 1,560 *g*, 4°C to remove salt precipitation. The resulting cell- and salt-precipitate-free supernatant was diluted in phosphate-buffered saline (PBS, 21-031-CVR, Corning, Corning, NY) before analysis.

Flow Cytometer Adaptations

We systematically evaluated adaptations to the optical configuration and fluidics ($N = 1$ for all configurations) of a FACSCanto flow cytometer (Fig. 2A). Upon hardware adaptations, FACSCanto should only be used for research purposes and cannot be used for diagnostic purposes.

Optical configuration

Obscuration bars with different designs were obtained from BD (cat# 641570 and 647895). Among the tested obscuration bar designs are the standard design (#1 in Fig. 3A), a symmetrical and asymmetrical vertical design (#2 and #3 in Fig. 3A), a cross design (#4 in Fig. 3A), and a round design (#5 in Fig. 3A). The vertical designs were tested because the laser is shaped as a vertical ellipse at the position of the obscuration bar, in which Obscuration bar 3 was intended to represent a slightly broader version of Obscuration bar 2. The cross design was tested as a thicker version of the standard design and the round design was tested because it blocks a uniform angle of light. For each FSC detection module, all obscuration bars were tested and the optimal one for that module was identified and used during all subsequent analysis with the module. The standard 20 mW laser of the FACSCanto was replaced with a 20–200 mW adjustable power laser (both 488 nm Sapphire, Coherent, Santa Clara, CA).

The standard SSC detection module of the FACSCanto (Supporting Information Fig. S2A) contains a pinhole with a diameter of 1,000 µm. Here we tested an SSC module (BD, Supporting Information Fig. S2B) with a 105, 200, or 400 µm fiber (Thorlabs, Newton, NJ), which acts as a spatial pinhole, to see if further confocalization (i.e., decreasing the pinhole size) improves scatter sensitivity. Increased confocalization decreases the contribution of background scattered light (e.g., scattering of the channel walls and particles in the sheath; Fig. 2A) and thereby decreases the noise, thus potentially improving the sensitivity. Under the assumption that particles pass through the focus of the collection lens, and because the image of the particle is at least 14-fold smaller than the pinhole, the pinhole does not affect the collection angles.

The standard FSC detection module (Supporting Information Fig. S2A) contains a photodiode (PD) and an obscuration bar to prevent the illuminating laser light from reaching the detector. Here, we confocalized FSC detection by replacing the standard FSC detection module with the dual FSC module (BD, Supporting Information Fig. S2B). In addition to an obscuration bar, the dual FSC module also contains a numerical aperture (NA) ~0.2 lens and 400 µm pinhole. Next to a PD, the dual FSC module contains a photomultiplier tube (PMT), which typically has lower detector noise than PDs.

Subsequently, a prototype tube FSC detection module (BD, Supporting Information Fig. S2C) was tested, which consists of a PMT, a 6.7× magnifying lens set and a 100 µm pinhole to enable better separation between sample stream and

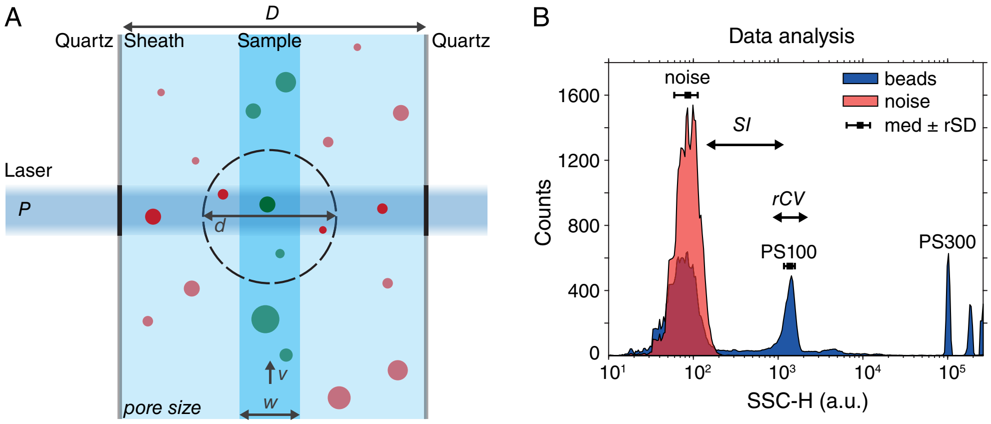

Figure 2. (**A**) Schematic representation of the adaptations made to increase sensitivity. Depicted is the channel inside the cuvette (black lines), containing the sheath stream with particles (red circles) and sample stream with particles (green circles). A projection of the detector pinhole (dashed black line) is also shown. Here we investigated how the scatter sensitivity depends on laser power (*P*), pinhole diameter (*d*), sample stream width (*w*), sample flow velocity (*v*), flow channel dimensions (*D*), and the pore size of the sheath filter. (**B**) Side scatter (SSC-H) histogram of beads (blue) and noise (red). The median intensity (med, black squares) and robust standard deviation (rSD, whiskers) are used to calculate the separation index (SI) and robust coefficient of variation (rCV) according to Eqs. 1 and 2. The SI thereby is a measure for the separation between a bead population and the noise, and the rCV for the reproducibility of the system. PS100, 100 nm polystyrene (PS) bead population; PS300, 300 nm PS bead population. [Color figure can be viewed at wileyonlinelibrary.com]

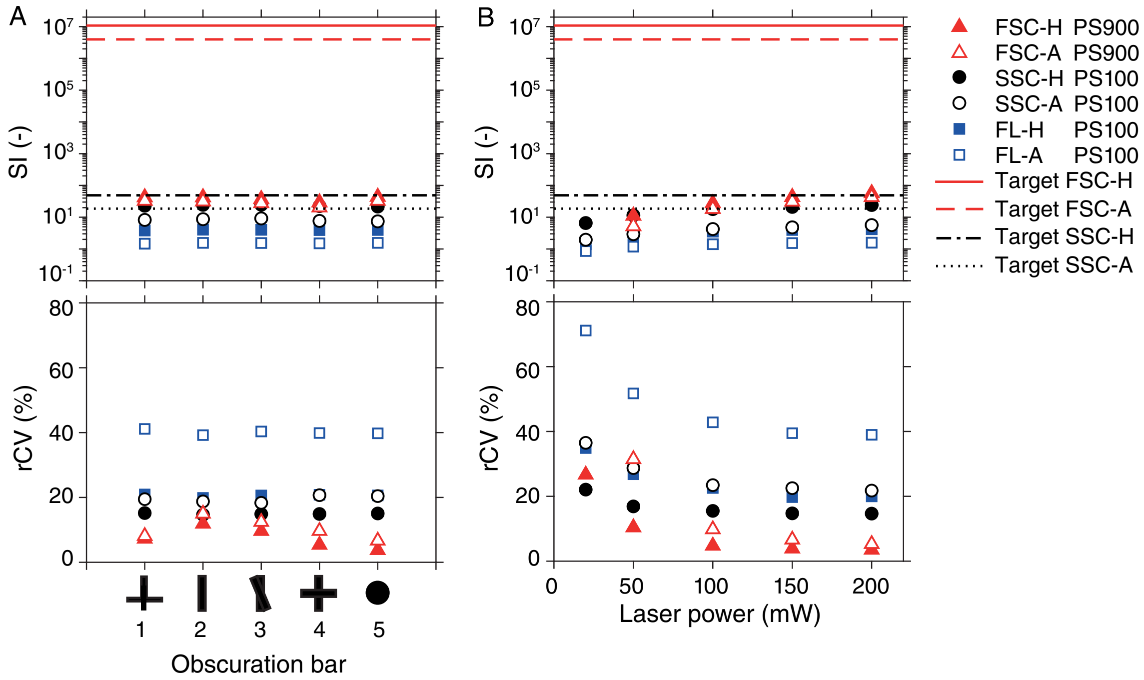

Figure 3. Influence of (**A**) forward scatter (FSC) obscuration bar shape and (**B**) laser power on the separation index (SI, top panels) and robust coefficient of variation (rCV, bottom panels). For FSC (red triangles), data of 900 nm polystyrene (PS) are shown, for side scatter (SSC, black circles) and fluorescence (FL, blue squares) data of 100 nm PS are shown. The required SI for the depicted PS bead to allow detection of 100 nm extracellular vesicles for FSC (red lines) and SSC (black lines) as calculated using Mie theory are also shown. Data collected using standard flow cytometer set up. *A*, area parameter; *H*, height parameter. [Color figure can be viewed at wileyonlinelibrary.com]

background signals. This design was optimized using simulations in Zemax (Zemax LLC, Kirkland, WA), and the resulting optimized tube FSC detection module (Supporting Information Fig. S2D) containing a 6.5× magnifying lens set and a 100, 200, or 300 µm pinhole (all Thorlabs) was tested.

Fluidics

The sample stream width (*w* in Fig. 2A) was varied by adjusting the sample pressure in the Diva software (BD). The resulting sample width was determined by running a fluorescent sample (diluted ink from yellow Stabilo Boss marker, Staples, Framingham, MA) and imaging the flow channel with a home-built 2.8× microscope. The sample width was defined as the full width at half the maximum of the fluorescent intensity in the captured image.

The sample flow rate (*v* in Fig. 2A) was reduced by reducing the sheath flow rate, which due to the design of the flow cell determines the sample flow velocity. The sheath flow rate reduced by placing an adjustable flow tubing clip (Fisher Scientific, Hampton, NH) on the sheath tubing. The sheath flow rate was measured by mass discharge and we confirmed a reciprocal relationship between the width parameter and the measured sheath flow rate (Supporting information, Fig. S5). While reducing the sheath flow rate, the sample stream width was monitored by microscopy (see previous paragraph) and kept constant by reducing the sample flow rate using a syringe pump (11Plus, Harvard apparatus, Holliston, MA). Another way to reduce the sample flow velocity is by decreasing the dimensions of the flow channel (*D* in Fig. 2A) in the cuvette. A narrower flow channel has a higher flow resistance, thereby causing a reduction in sample flow velocity. Here, we tested a cuvette (Hellma, Jena, Germany) with an inner flow channel of half the dimensions of the standard one. The sampling rate of the analog-to-digital converter was 10 MHz for all adaptations. Lastly, the standard 0.2 µm sheath filter was replaced with a 0.1 µm filter (Millipak-100, Merck Chemicals, Darmstadt, Germany).

Flow Cytometry Analysis

To optimize the hardware (Figs. 2–5), green fluorescence of the Megamix-plus FSC beads was detected in the fluorescein isothiocyanate (FITC) channel (530/30 band-pass filter) and in the phycoerythrin (PE) channel (585/42 band-pass filter). The fluorescence detected in the FITC channel was used to trigger data acquisition, to ensure detection of all beads throughout the adaptations. The fluorescence detected in the PE channel was used to monitor the effect of the adaptations on the fluorescence sensitivity, and as a control. The Megamix beads were diluted in 10-fold concentrated PBS (BE17-525F, Lonza, Basel, Switzerland) and purified and deionized water to obtain Megamix beads in 1-fold concentrated PBS. A minimum of 1,000 events per bead population were acquired. Noise levels were estimated by measuring PBS while triggering on the FITC channel with low threshold (200 arbitrary units [a.u.]) and high voltage (600 V). The resulting randomly triggered events enable an approximation of FSC and SSC noise.

To enable determination of the separation index (SI), and thereby monitor the sensitivity, both noise and bead signal need to be within the dynamic range of the detector. Thereto, the PMT voltage was adjusted after every adaptation, according to a standardized protocol. The voltage on the FITC channel was configured to attain a rate of 1000 (noise) events/s in PBS using FITC triggering. Next, the SSC voltage was set such that the 300 nm bead had an intensity of 10^5 a.u., and the PE voltage such that the 500 nm bead had an intensity of 10^4 a.u. Since only the 900 nm bead was detectable on FSC in the standard configuration, the FSC PMT voltage was instead configured to center the noise in the FSC channel around 10^2 a.u. At the used PMT voltages, the optical noise is dominant over the electronic noise for all channels (robust SD [rSD] with laser off $\leq 2.5 \cdot$rSD with laser on), except for SSC after the illumination and detection adaptations. After these adaptations, the noise on SSC was no longer within the dynamic range using the 300 nm bead setting approach, so for the fluidics experiments the noise on SSC was also centered around 10^2 a.u. with the PMT voltage, causing the optical noise to be dominant again. For a complete description of the flow cytometer configuration, operating conditions and data analysis, see the MIFlowCyt list in Supporting Information Data S1.

To demonstrate the sensitivity of the optimized system (Fig. 6), we triggered on SSC to enable detection of non-fluorescent beads. Noise levels were estimated by triggering on the FITC channel, as described before.

Data Analysis

The SI and rCV (Fig. 2B) for each bead population were calculated as follows:

$$\mathrm{SI} = \frac{\mathrm{median}_{\mathrm{bead}} - \mathrm{median}_{\mathrm{noise}}}{2 \cdot \mathrm{rSD}_{\mathrm{noise}}}, \qquad (1)$$

$$\mathrm{rCV} = \frac{\mathrm{rSD}_{\mathrm{bead}}}{\mathrm{median}_{\mathrm{bead}}} \cdot 100\%, \qquad (2)$$

with $\mathrm{median}_{\mathrm{bead}}$ the median intensity of the bead population, $\mathrm{median}_{\mathrm{noise}}$ the median intensity of the noise, and $\mathrm{rSD}_{\mathrm{noise}}$ and $\mathrm{rSD}_{\mathrm{bead}}$ the robust SD of the noise and bead, respectively, defined as

$$\mathrm{rSD} = \S\left(\mathrm{percentile}_{84.13} - \mathrm{percentile}_{15.87}\right), \qquad (3)$$

with $\mathrm{percentile}_{84.13}$ and $\mathrm{percentile}_{15.87}$ the intensity of the noise or bead population at those percentiles. Eq. 1 was selected in analogy to the Stain Index (26), which is commonly used to express brightness in fluorescence. The rCV was preferred over the CV because the rCV is less affected by outliers. Data analysis was done in Matlab R2018b (Mathworks, Natick, MA). The SI and rCV were calculated for both the height and area parameters. Data for both parameters are given in the figures. However, the SI on the area parameter was negative for some configurations, making expressions of fold changes between configurations meaningless. Therefore, under the condition that the area and height parameters show the same trend, the text contains only quantitative statements of the height parameter. For SSC and fluorescence, data of the 100 nm bead are shown in all figures. For FSC, the bead used to follow progress differs per figure, as a result of large improvements in sensitivity. Throughout this manuscript, an improvement in sensitivity is defined as an increase in SI >1-fold and/or a reduction in rCV >1-fold.

Mie Theory

Scatter versus diameter relations were calculated for the standard and optimized FACSCanto FSC and SSC detection modules as described previously (19), using Mie theory and a bead mixture with beads of known size and refractive index (Exometry, Amsterdam, the Netherlands). Since the standard FSC detection module detects only one bead of the bead mixture, modeling of the optical configuration of the FSC detection module was performed by manual calculations based on geometry. Using the scatter versus diameter relations, the scatter intensities in a.u. can be linked to the corresponding scattering cross section (σ_s) in nm^2.

The scatter intensity of a 100 nm EV can be derived from the scatter versus diameter relation for EVs (assuming a refractive index of 1.40 throughout this manuscript unless stated otherwise). Assuming that the noise shape is conserved (i.e., SD/median will stay the same), the required noise median to achieve an SI of 1 for a 100 nm EV can be derived from Eq. 1. With the scatter versus diameter relation for PS, this noise median can be translated into an SI needed for any specific size PS bead, at which 100 nm EVs will then be detectable. The resulting SIs are depicted as the "target" in Figures 3–5. See Supplemental Information Appendix S1 for a detailed description of the calculation of the target values. Furthermore, using the measured noise distributions on the standard and optimized FACSCanto, the median signal at which an SI of 2 is achieved can be calculated from Eq. 1. The detection limits for EVs were subsequently derived from the scatter versus diameter relations for EVs with a refractive index ranging between 1.37 (22,27) and 1.40 (28,29).

RESULTS

Optical Configuration

Figure 3A shows the effect of the obscuration bar shape on the SI and rCV in the standard flow cytometer. Since the obscuration bar is in the detection path of FSC only, no differences were expected nor observed for SSC and fluorescence. Figure 3A shows that the obscuration bar shape mainly affected the rCV for FSC, with minor variations in the SI (<1.5-fold). The latter can be explained by the fact that the noise suppression reaches a maximum once the entire laser beam is blocked, which is the case for all tested obscuration bars. A possible explanation for the changes in rCV is that variations in the FSC intensity due to the position of the particle in the sample stream are more efficiently canceled out by one obscuration bar than the other. The round obscuration bar (#5 in Fig. 3A) resulted in the lowest rCV (1.9-fold improvement) in the standard flow cytometer, and also for

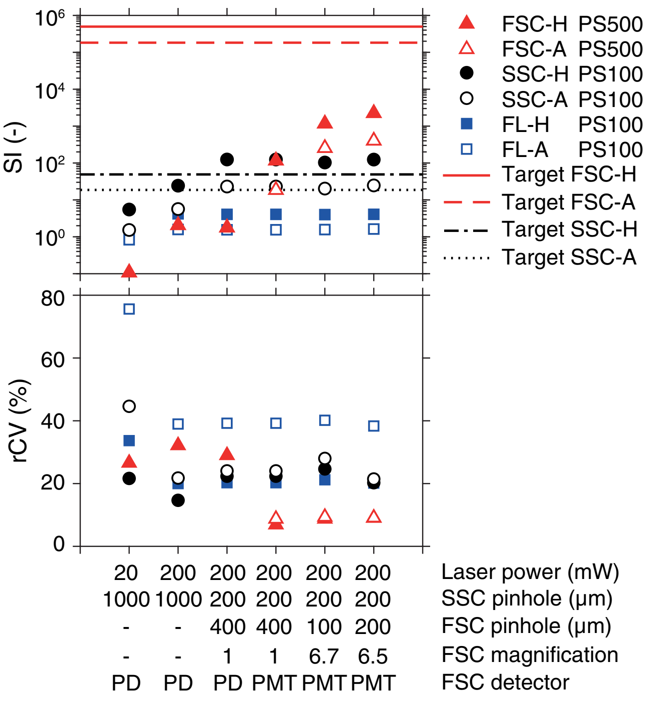

Figure 4. Influence of laser power in combination with adaptations in the detection modules on the separation index (SI, top panels) and robust coefficient of variation (rCV, bottom panels). For forward scatter (FSC, red triangles), data of 500 nm PS are shown, for side scatter (SSC, black circles) and fluorescence (FL, blue squares) data of 100 nm PS are shown. Lines represent the required SI for the depicted PS bead to allow detection of 100 nm extracellular vesicles for FSC (red lines) and SSC (black lines), as calculated using Mie theory. *A*, area parameter; *H*, height parameter; PD, photodiode, PMT, photomultiplier tube. [Color figure can be viewed at wileyonlinelibrary.com]

the other FSC modules (data not shown). Therefore, we used the round obscuration bar in all further experiments.

Figure 3B shows the effect of the laser power on the SI and rCV in the standard flow cytometer. An increased laser power resulted in an improved SI and rCV for all detectors. Because the scattered power is linearly proportional to the illuminating power, an increase in laser power increases the number of scattered photons, thereby increasing the SI and decreasing rCV according to photon statistics.

Figure 4 shows the influence of laser power in combination with adaptations in the FSC and SSC detection modules on the SI and rCV. The first column of the graphs shows the SI and rCV for the standard FACSCanto. Increasing the laser power from 20 to 200 mW (second column), improved the SI 19-fold for FSC, 4.4-fold for SSC, and 3.0-fold for fluorescence. The 10-fold increase in laser power could achieve a 19-fold improvement in SI for FSC because SI <1 at 20 mW. The rCV thereby worsened 1.2-fold for FSC and improved 1.5-fold for SSC and 1.7-fold for fluorescence. Confocalization (third column) worsened the SI 1.2-fold for FSC and improved the SI 5.1-fold for SSC. The rCV improved 1.1-fold for FSC and worsened 1.5-fold for SSC. Replacing the 200 μm fiber on SSC for a 105 μm fiber did not improve SSC sensitivity (e.g., worsened the SI 2.5-fold and the rCV 2.7-fold, data not shown). The 400 μm fiber improved the rCV 1.6-fold, but worsened the SI 1.2-fold (data not shown). As shown by the SI of the 100 nm PS bead relative to the target, the combination of increased laser power and the 200 μm fiber enabled detection of 100 nm EVs on SSC (third column). Since we thereby reached our aim for SSC detection, further modifications to the optical configuration were focused on the FSC module. Replacement of the FSC PD with a PMT in the confocalized setup (fourth column), improved the SI on FSC 66-fold and the rCV 4.2-fold. Addition of two magnifying lens sets and reduction of the pinhole diameter (fifth column) improved the SI 10-fold, with only a slight worsening of the rCV (1.3-fold). Optimization of this setup by replacing the two magnifying lens sets with a single one led to another 1.9-fold improvement in the SI while keeping the rCV similar (improvement of 1.0-fold, sixth column). Changing the 200 μm pinhole for a 100 or 300 μm pinhole did not improve FSC sensitivity (SI worsened >1.4-fold, data not shown).

All together, the SI improved $2.1 \cdot 10^4$-fold for FSC, 23-fold for SSC, and 2.9-fold for fluorescence due to adaptations in the optical configuration, and the rCV improved 2.9-fold for FSC, 1.1-fold for SSC, and 1.7-fold for fluorescence. We continued with the optimized optical configuration (last column) to study the influence of adaptations in the fluidics on the SI and rCV.

Fluidics

Figure 5A shows the influence of the sample stream width on the SI and rCV. The sample flow rate was kept constant during these experiments. Reducing the sample stream width from 25 to 12 μm improved the SI 1.8-fold for FSC, 1.3-fold for SSC, and 1.0-fold for fluorescence. The rCV thereby improved 1.8-fold for FSC, 2.2-fold for SSC, and 1.1-fold for fluorescence.

The influence of the sheath flow rate, and thereby sample flow velocity, on the SI and rCV is shown in Figure 5B. The sample stream width was kept constant during these experiments. Here, the height parameter and the area parameter show a different trend. While the SI of the height parameter does not change (1.1-fold improvement for FSC, 1.5-fold worsening for SSC, 1.1-fold improvement for fluorescence), the SI of the area parameter does. This can be explained by the fact that a longer transit time will result in light being scattered by the particle over a longer period of time, so the integrated scattered light over time will be higher (i.e. area parameter), but the maximal amplitude of the scattered light per time point will not change significantly (i.e. height parameter). For the area parameter, a 17.5-fold reduction in sample flow velocity improved the SI 15-fold for FSC, 7.7-fold for SSC, and 9.6-fold for fluorescence. The area rCV, however, worsened 2.8-fold for FSC, 2.5-fold for SSC, and improved 2.5-fold for fluorescence. Also, the height rCV increased with decreasing flow rate. Such increases in the rCV are undesirable, since high rCVs indicate poor reproducibility and decrease resolution.

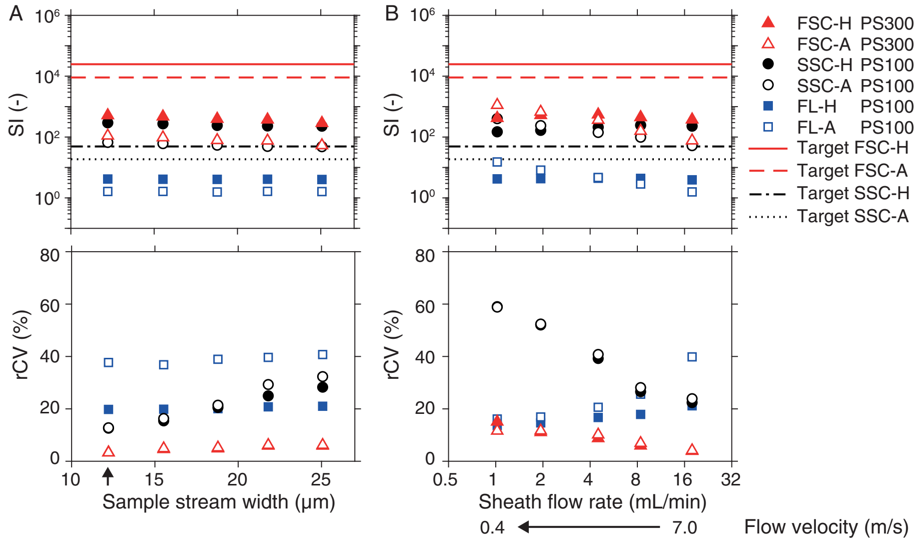

Figure 5. Influence of (**A**) sample stream width and (**B**) sample flow velocity on the separation index (SI, top panels) and robust coefficient of variation (rCV, bottom panels). For forward scatter (FSC, triangles), data of 300 nm PS are shown, for side scatter (SSC, black circles) and fluorescence (FL, blue squares) data of 100 nm PS are shown. Lines represent the required SI for the depicted PS bead to allow detection of 100 nm extracellular vesicles for FSC (red lines) and SSC (black lines), as calculated using Mie theory. Data collected using optimal detection setup (Fig. 4, right column). Sensitivity of the final optimized FACSCanto as indicated by the arrow in panel A. *A*, area parameter; *H*, height parameter. [Color figure can be viewed at wileyonlinelibrary.com]

Combining a low sample flow velocity (0.4 m/s, 1 mL/min) with a low sample stream width (12 µm) slightly improved the rCVs, but still resulted in an rCV of 45% for SSC (Supporting Information Fig. S3). The overall gain in FSC SI is thereby small (1.9-fold compared to decreasing the sample stream width alone). Taken together, the tested reductions in sample flow velocity do not improve the scatter sensitivity of this system. Similarly, a 2-fold reduction in the dimensions of the flow channel in the cuvette did not result in substantial changes in the SI or rCV (Supporting Information Fig. S3). The latter could be explained by the fact that the contribution of background light is higher in a narrower flow channel, because the walls of the flow channel are closer to the sample stream and thus to the detector pinhole. In addition, reducing the pore size of the sheath filter from 0.2 to 0.1 µm did not change the SI or rCV (Supporting Information Fig. S3). Changing the filters thus did not reduce the noise level.

With regard to the fluidics, only decreasing the sample stream width improved the scatter sensitivity of the flow cytometer in this study. The optimized FACSCanto thus has the sensitivity as depicted in Figure 5A at a sample stream width of 12 µm (arrow in Fig. 5A).

EV Measurement

To demonstrate the sensitivity of the optimized FACSCanto, beads and EVs isolated from human urine were measured using SSC thresholding on both the optimized FACSCanto (Fig. 6A,C) and a standard FACSCanto II (Fig. 6B,D), which has a comparable sensitivity to the standard FACSCanto. PMT voltages on both instruments were set according to the protocol described in “Materials and Methods” section, and a low sample flow rate was used on the FACSCanto II.

Figure 6A shows that on the optimized FACSCanto, the 189 and 374 nm hollow silica beads can easily be detected on SSC. On FSC, the 374 nm hollow silica bead is almost separated from the noise. On the standard FACSCanto (Fig. 6B), both hollow silica beads cannot be detected. On the optimized FACSCanto, 100 nm PS is 2 decades from the noise on SSC, whereas on the standard FACSCanto it is still indiscernible from the noise. The smallest detectable bead ($SI > 1$) on the optimized FACSCanto is 75 nm silica on SSC and 150 nm PS on FSC. On the standard FACSCanto, the smallest detectable bead is 125 nm PS on SSC and >400 nm PS on FSC.

Since the 75 nm silica beads were close to the detection limit, there is a risk of swarm detection, meaning that hundreds of particles are simultaneously illuminated and wrongly detected as single particles (21). To exclude swarm detection of 75 nm silica beads, we determined the size distribution of the beads by transmission electron microscopy (Supporting Information Fig. S1) to (1) confirm absence of contaminations <75 nm, which may contribute to swarm detection, and (2) determine the mean size and total concentration of the beads. Next, we diluted the silica beads to a concentration of 10^7/ml, at which only 1–2.5% of the events is caused by the simultaneous presence of two silica beads (Supporting Information Fig. S4). The fact that the measured bead concentration was only a factor 2 lower than expected, thereby excludes swarm and coincidence detection. Figure S6 of the Supporting Information shows a calibration of the SSC-H detector using Mie theory to further confirm that single 75 nm silica beads indeed exceed the trigger threshold.

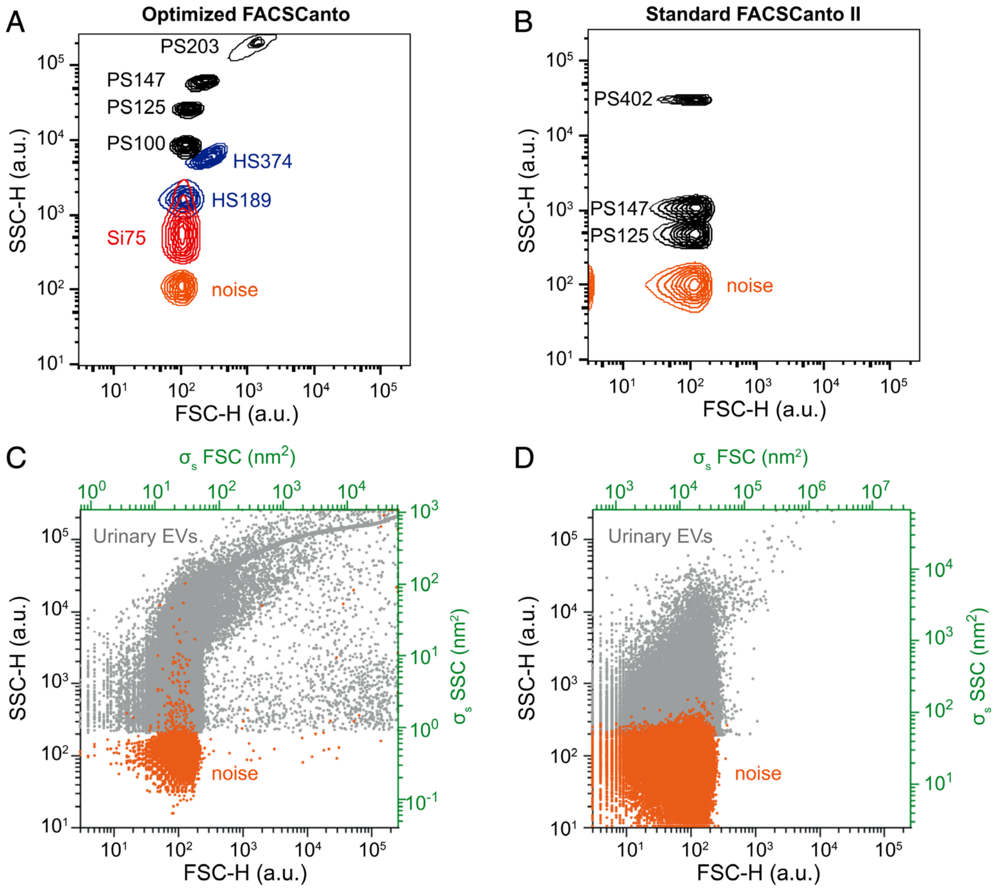

Figure 6. (**A**,**B**) Contour plots of side (SSC-H) versus forward scatter (FSC-H) for beads and noise on the optimized FACSCanto (A) and standard FACSCanto II (B). Noise data acquired using a trigger on the fluorescein isothiocyanate (FITC) channel as described in "Materials and Methods" section. (**C**,**D**) scatter plots of SSC-H versus FSC-H for urinary extracellular vesicles (gray dots) and noise (orange) as measured on the optimized FACSCanto (C) and standard FACSCanto II (D). Bottom and left axes (black) show the scattering intensities in arbitrary units (a.u.), top and right axes (green) show the corresponding scattering cross section (σ_s) in nm^2 as described in "Materials and Methods" section. Data of the height (*H*) parameter are shown, since theses data showed a better separation from the noise. Si, silica; HS, hollow silica; PS, polystyrene; Si75, 75 nm silica beads. [Color figure can be viewed at wileyonlinelibrary.com]

Figure 6C,D shows clear differences between the FSC versus SSC plots of the urine EVs on both flow cytometers. In addition to the standard axis in a.u., the calibrated axis in terms of the measured σ_s in nm^2 is shown. The σ_s of a 100 nm EV (refractive index 1.40) and 75 nm silica beads (refractive index 1.463) for SSC on the optimized FACSCanto are 1.52 and 1.31 nm^2, respectively. Since these values for σ_s exceed the σ_s of the noise in Figure 6C, modeling thus shows that 100 nm EVs and 75 nm silica beads are separated from the noise on SSC of the optimized FACSCanto. Furthermore, the calibrated axis show that the optimized FACSCanto allows detection of signals that are two orders of magnitude lower on SSC, and three orders of magnitude lower on FSC compared to the standard FACSCanto.

DISCUSSION

In this study, we systematically evaluated adaptations to the optical configuration and fluidics of a common flow cytometer, the FACSCanto, and showed the resulting effects on the FSC, SSC, and fluorescence sensitivity.

rCVs were found to worsen slightly upon increased confocalization for SSC, which is because the 200-μm pinhole diameter is near the projected width of the imaged sample stream at the pinhole (~150 μm). This configuration leads to sample position-dependent transmission of light through the pinhole, with the highest transmission for particles that travel through the center of the pinhole. A magnifying lens set added to FSC allowed optimization of the projected width of the sample stream at the pinhole and the pinhole diameter, using commercially available pinholes. A decreased sample stream width enabled further optimization resulting in improved rCVs and slight improvements in the SI. Previous work suggested that the pinhole diameter should be twice the projected sample stream diameter to achieve low rCVs (17). Here, the final system has a 12 μm wide sample stream, which results in a 96 μm projected sample stream diameter for SSC, and 78 μm for FSC, which compared to the 200 μm pinholes used indeed results in a factor of ~2.

Several studies increased the sensitivity of their flow cytometer by increasing the transit time of the particle in the laser beam, that is, decreasing the sample flow velocity (10,12). Unexpectedly, for this system, the rCV on FSC and SSC worsened when decreasing the sample flow velocity, even though we adjusted the sample flow rate to the sheath flow rate to maintain the same sample stream width. Analysis of the sample stream width revealed a 1.86-fold increase in the sample stream width with decreasing flow velocity, which was found to be partly due to diffusion of the fluorescent dye molecules into the sheath. For EV particle sizes, however, diffusion is at least 50-fold smaller, and therefore unlikely to play a role. Another explanation for the observed worsening in rCV could be that the fluidics becomes less stable due to the restriction on the sheath flow rate, or the design of the cuvette and cuvette holder. Fluidic instability can cause fluctuations in the position of the sample stream, which will worsen rCVs as not all scattered light will be collected with equal efficiency by the pinholes.

With the exception of the worsened rCVs at low sample flow velocities, the effects of the adaptations described in this study are expected to be similar for at least all BD flow cytometers incorporating a cuvette, and possibly all flow cytometers. The described adaptations can therefore be used to increase the sensitivity of any (BD) flow cytometer. Except for the adaptation of the sample flow velocity, the effects of the adaptations were thereby similar for the height and area parameter. For FSC, the highest impact was changing the PD for a PMT (66-fold SI improvement). For SSC, both increased laser power and reduced pinhole diameter caused a similar improvement in the SI (4.4- and 5.1-fold, respectively).

The adaptations in the optical configuration and fluidics resulted in a total improvement of the SI on FSC of $3.8{\cdot}10^4$-fold, on SSC of 30-fold, and on fluorescence of 2.9-fold. As a result, the estimated detection limits (SI = 2) for EVs (refractive index between 1.37–1.40 (22,27–29)) changed from 1,228–1,571 nm on FSC and 182–272 nm on SSC for the standard FACSCanto, to 246–310 nm on FSC and 91–117 nm on SSC for the optimized FACS Canto. On FSC, another ~50-fold improvement is needed to allow detection of 100 nm EVs. A possible way to further increase the FSC sensitivity is by using a 405 nm laser instead of 488 nm, which has been shown to increase the scattered light intensity for SSC ~2-fold (30) and should be effective for FSC as well. Another way would be to increase the laser power >200 mW, and/or to increase the NA. The latter will require modification of the SSC objective holder, since this is now physically obstructing the realization of a large NA on FSC. Another route toward improved sensitivity might be to improve the signal processing. In addition to hardware adaptations, this will require adaptation of the software, which is why we did not explore this route in the current study.

As shown in Figure 6A, the smallest detectable bead (SI > 1) on the optimized FACSCanto is 75 nm silica on SSC and 150 nm PS on FSC. The SSC sensitivity is thereby better than or comparable to reported in previously mentioned work (better than References 9,13–18,31, comparable to Reference 11). Only the NanoFCM (10,12) has a higher SSC sensitivity of 24 nm silica beads. For FSC, only the Beckman Coulter MoFlo Asterios (31) has a comparable and the BD Influx (16) a better sensitivity than our optimized FACSCanto. Both the NanoFCM and BD Influx, however, are not suited to be used in routine (clinical) labs, the NanoFCM because of its low count rate (~200 events/s (10)), and the BD Influx because it requires the permanent presence of a highly skilled operator. Here, we thus present the first operator-friendly, high-throughput flow cytometer with a high sensitivity on SSC and FSC, enabling the determination of EV size and refractive index in human body fluids.

Acknowledgments

This work was supported by the Netherlands Organisation for Scientific Research—Domain Applied and Engineering Sciences (NWO-TTW), research programmes VENI 13681 (F.A.W.C.), VENI 15924 (E.v.d.P.), and STW Perspectief program CANCER-ID 14195 (L.d.R.). Tina Van Den Broeck and Ludovic Monheim are both employees of BD Biosciences, a business unit of Becton, Dickinson and Company. Frank A.W. Coumans and Edwin van der Pol are co-founder and stakeholder of Exometry B.V., Amsterdam, the Netherlands.

References

1. O'Driscoll L. Expanding on exosomes and ectosomes in cancer. N Engl J Med 2015; 372:2359–2362.
2. Loyer X, Vion A-C, Tedgui A, Boulanger CM. Microvesicles as cell–cell messengers in cardiovascular diseases. Circ Res 2014;114:345–353.
3. Yuana Y, Sturk A, Nieuwland R. Extracellular vesicles in physiological and pathological conditions. Blood Rev 2013;27:31–39.
4. Robbins PD, Morelli AE. Regulation of immune responses by extracellular vesicles. Nat Rev Immunol 2014;14:195–208.
5. Coumans FAW, Brisson AR, Buzas EI, Dignat-George F, Drees EEE, El-Andaloussi S, Emanueli C, Gasecka A, Hendrix A, Hill AF, et al. Methodological guidelines to study extracellular vesicles. Circ Res 2017;120:1632–1648.
6. van der Pol E, Coumans FAW, Grootemaat AE, Gardiner C, Sargent IL, Harrison P, Sturk A, van Leeuwen TG, Nieuwland R. Particle size distribution of exosomes and microvesicles determined by transmission electron microscopy, flow cytometry, nanoparticle tracking analysis, and resistive pulse sensing. J Thromb Haemost 2014; 12:1182–1192.
7. van der Pol E, Sturk A, van Leeuwen T, Nieuwland R, Coumans F. Standardization of extracellular vesicle measurements by flow cytometry through vesicle diameter approximation. J Thromb Haemost 2018;16:1236–1245.
8. Arraud N, Linares R, Tan S, Gounou C, Pasquet JM, Mornet S, Brisson AR. Extracellular vesicles from blood plasma: Determination of their morphology, size, phenotype and concentration. J Thromb Haemost 2014;12:614–627.
9. Stoner SA, Duggan E, Condello D, Guerrero A, Turk JR, Narayanan PK, Nolan JP. High sensitivity flow cytometry of membrane vesicles. Cytometry A 2016;89: 196–206.
10. Zhu S, Ma L, Wang S, Chen C, Zhang W, Yang L, Hang W, Nolan JP, Wu L, Yan X. Light-scattering detection below the level of single fluorescent molecules for high-resolution characterization of functional nanoparticles. ACS Nano 2014;8: 10998–11006.
11. Steen HB. Flow cytometer for measurement of the light scattering of viral and other submicroscopic particles. Cytometry A 2004;57A:94–99.
12. Yang L, Zhu S, Hang W, Wu L, Yan X. Development of an ultrasensitive dual-channel flow cytometer for the individual analysis of nanosized particles and biomolecules. Anal Chem 2009;81:2555–2563.
13. Hercher M, Mueller W, Shapiro HM. Detection and discrimination of individual viruses by flow cytometry. J Histochem Cytochem 1979;27:350–352.
14. Danielson KM, Estanislau J, Tigges J, Toxavidis V, Camacho V, Felton EJ, Khoory J, Kreimer S, Ivanov AR, Mantel P-Y, et al. Diurnal variations of circulating extracellular vesicles measured by nano flow cytometry. PLoS One 2016;11:e0144678.
15. Steen HB. Simultaneous separate detection of low angle and large angle light scattering in an arc lamp-based flow cytometer. Cytometry 1986;7:445–449.
16. Nolte-'t Hoen ENM, van der Vlist EJ, Aalberts M, Mertens HCH, Bosch BJ, Bartelink W, Mastrobattista E, van Gaal EVB, Stoorvogel W, Arkesteijn GJA, et al. Quantitative and qualitative flow cytometric analysis of nanosized cell-derived membrane vesicles. Nanomedicine 2012;8:712–720.
17. Zarrin F, Risfelt JA, Dovichi NJ. Light scatter detection within the sheath flow cuvette for size determination of multicomponent submicrometer particle suspensions. Anal Chem 1987;59:850–854.

18. Chandler WL, Yeung W, Tait JF. A new microparticle size calibration standard for use in measuring smaller microparticles using a new flow cytometer. J Thromb Haemost 2011;9:1216–1224.
19. de Rond L, Coumans FAW, Nieuwland R, van Leeuwen TG, van der Pol E. Deriving extracellular vesicle size from scatter intensities measured by flow cytometry. Curr Protoc Cytom 2018;86:e43.
20. Welsh JA, Horak P, Wilkinson JS, Ford VJ, Jones JC, Smith D, Holloway JA, Englyst NA. FCMPASS software aids extracellular vesicle light scatter standardization. Cytometry A 2019.
21. van der Pol E, van Gemert MJC, Sturk A, Nieuwland R, Van Leeuwen TG. Single vs. swarm detection of microparticles and exosomes by flow cytometry. J Thromb Haemost 2012;10:919–930.
22. van der Pol E, de Rond L, Coumans FAW, Gool EL, Böing AN, Sturk A, Nieuwland R, van Leeuwen TG. Absolute sizing and label-free identification of extracellular vesicles by flow cytometry. Nanomedicine 2018;14:801–810.
23. de Rond L, Libregts SFWM, Rikkert LG, Hau CM, van der Pol E, Nieuwland R, van Leeuwen TG, Coumans FAW. Refractive index to evaluate staining specificity of extracellular vesicles by flow cytometry. J Extracell Vesicles 2019;8:1643671.
24. Varga Z, van der Pol E, Pálmai M, Garcia-Diez R, Gollwitzer C, Krumrey M, Fraikin J-L, Gasecka A, Hajji N, van Leeuwen TG, et al. Hollow organosilica beads as reference particles for optical detection of extracellular vesicles. J Thromb Haemost 2018;16:1646–1655.
25. Rikkert LG, Nieuwland R, Terstappen LWMM, Coumans FAW. Quality of extracellular vesicle images by transmission electron microscopy is operator and protocol dependent. J Extracell Vesicles 2019;8:1555419.
26. Maecker HT, Frey T, Nomura LE, Trotter J. Selecting fluorochrome conjugates for maximum sensitivity. Cytometry A 2004;62A:169–173.
27. van der Pol E, Coumans FAW, Sturk A, Nieuwland R, van Leeuwen TG. Refractive index determination of nanoparticles in suspension using nanoparticle tracking analysis. Nano Lett 2014;14:6195–6201.
28. Gardiner C, Shaw M, Hole P, Smith J, Tannetta D, Redman CW, Sargent IL. Measurement of refractive index by nanoparticle tracking analysis reveals heterogeneity in extracellular vesicles. J Extracell Vesicles 2014;3:25361.
29. Konokhova AI, Yurkin MA, Moskalensky AE, Chernyshev AV, Tsvetovskaya GA, Chikova ED, Maltsev VP. Light-scattering flow cytometry for identification and characterization of blood microparticles. J Biomed Opt 2012;17: 0570061–0570068.
30. McVey MJ, Spring CM, Kuebler WM. Improved resolution in extracellular vesicle populations using 405 instead of 488 nm side scatter. J Extracell Vesicles 2018;7: 1454776.
31. Morales-Kastresana A, Musich TA, Welsh JA, Telford W, Demberg T, JCS W, Bigos M, Ross CD, Kachynski A, Dean A, et al. High-fidelity detection and sorting of nanoscale vesicles in viral disease and cancer. J Extracell Vesicles 2019;8: 1597603.